



Università degli Studi di Napoli *Federico II*

DOTTORATO DI RICERCA IN FISICA

Ciclo XXIX

Coordinatore: prof. Salvatore Capozziello

# Single particle and collective electronic excitations in topological insulator nano-wires

Settore Scientifico Disciplinare: FIS/03

**Dottorando**  
Paolino Iorio

**Tutore**  
Prof. Vittorio Cataudella  
Dott. Carmine Antonio Perroni

Anni 2014/2017



# Contents

<b>Introduction</b>	<b>5</b>
<b>1 Three-Dimensional Topological Insulators</b>	<b>9</b>
1.1 $\mathbb{Z}_2$ Topological Insulators . . . . .	10
1.2 Type of 3D topological insulators and experiments . . . . .	16
1.2.1 Transport experiments . . . . .	22
1.2.2 Collective electronic excitations: Dirac surface plasmons	28
<b>2 Hamiltonian models for topological insulator <math>Bi_2Se_3</math></b>	<b>32</b>
2.1 Electronic Model for $Bi_2Se_3$ . . . . .	33
2.2 Effective model for surface states at $k_x = k_y = 0$ . . . . .	35
2.3 Effective model for surface states at $k_x \neq k_y \neq 0$ . . . . .	39
2.4 Confinement effects: Slab . . . . .	43
<b>3 Electronic states of topological insulator nano-wires</b>	<b>49</b>
3.1 Introduction . . . . .	51
3.2 Cylindrical nano-wire: analytical and numerical solution . . . . .	53
3.3 Rectangular nano-wire . . . . .	64
<b>4 Plasmon in topological insulator: cylindrical nano-wire</b>	<b>70</b>
4.1 Susceptibility and dynamic structure factor . . . . .	72
4.2 Zero surface density . . . . .	76

4.3 Finite surface density . . . . .	82
<b>Conclusion</b>	<b>90</b>
<b>Appendices</b>	<b>95</b>
<b>A Berry phase</b>	<b>96</b>
<b>B Numerical approaches</b>	<b>101</b>
<b>C Large radius limit of the polarization function and plasmon dispersion in cylindrical wire</b>	<b>106</b>
<b>D Calculation of the inverse dielectric function and dynamic structure factor in cylindrical wire</b>	<b>112</b>
<b>Bibliography</b>	<b>115</b>

# Introduction

In the last years, the interest for topological insulators (TIs) is rapidly growing. Due to their topological properties, they can have various applications for future technology. For example, an application could be in field of spintronics, that is electronics based on spin instead of charge. Actually, TIs would allow for zero field spin Hall effects and spin dependent conduction with a robustness against disorder larger than that of graphene. Another application has been envisaged in the superconducting phase of these materials. Indeed, they could give rise to Majorana states that can be used for robust quantum computation.

The work of this thesis is based on the analysis of TIs which show new interesting features when confined in one direction and interfaced with the vacuum. The bulk properties of these materials affect those of the surface, giving rise to the phenomena that distinguish a TI by a trivial insulator. This condition is called bulk-boundary correspondence. Indeed, they exhibit conductive surface states protected from backscattering due to the properties of time reversal symmetry combined with strong spin-orbit coupling. The energy dispersion of the surface states is present in the gap of the bulk and connects the valence band with the conduction band. Moreover, in particular points of the Brillouin zone, the bands of surface states present a linear dispersion forming the so called Dirac cone. The strong spin-orbit coupling leads to spin-momentum locking. In fact, the spin states are always perpendicular to the electron wave vector.

In this thesis we focus on the three-dimensional TIs and, in particular, the

novel compound  $Bi_2Se_3$  will be considered. This prototype system has a simple electronic structure: a bulk gap of the order of 0.3 eV and a single Dirac cone present at the  $\Gamma$  point of the Brillouin zone. The aim of this thesis is to analyze the effects of confinement on the electronic properties of  $Bi_2Se_3$  nano-structures such as thin films and wires. In particular, we have studied the influence of the confinement on some electronic features of the surface states, such as the linear energy dispersion at the Dirac cone and the spin momentum-locking. Stimulated by some experiments performed in nano-wires, we have studied the electronic properties of these systems from a theoretical point of view. We point out that the Berry phase plays a significant role in affecting the spectral properties. In this thesis, we have studied not only single particle but also collective electronic excitations such as Dirac plasmons. We have analyzed the features of magneto-plasmons in  $Bi_2Se_3$  nano-wires finding interesting properties with varying the cross-section area, the electron surface density and the strength of an axial magnetic field. We have emphasized that the Berry phase affects both the plasmon dispersion and line width. We have made some predictions on single particle and collective electronic properties which could be experimentally confirmed.

In the first chapter, we explain the main differences that exist between a traditional and a topological insulator. We will investigate the particular bulk symmetries that will lead to define a topological invariant  $\mathbb{Z}_2$  that sets the character of the matter from trivial to topological. Moreover, some clue experiments on topological insulators are discussed. In particular, experimental techniques such as Angle Resolved Photoemission Spectroscopy (ARPES) provide evidence of the influence of topological nature of these materials. In fact, the ARPES technique will show a metal surface with typical formation of the Dirac cone, while the spin-locked ARPES will highlight the relationship between momentum and spin and therefore the Berry phase equal to  $\pi$ . We will discuss some transport experiments made on nano-structures such as films and wires that have revealed the metallic and spinor nature of the surface states. The main difficulties in this type of experiments are to iso-

late the bulk contribution from that of the surface. Due to impurities and imperfections of the material, the chemical potential tends to enter into the conduction band of the bulk, thus observing bulk phenomena and not surfaces one. A strategy to avoid the impurity problem is to make the ratio between volume and surface the lowest possible, just as in the case of nanostructures. Finally, the study of plasmon excitations at the surface of these materials is also very relevant. In the first chapter, we will also discuss some experiments which have confirmed the presence of plasmons representing the collective excitations of massless Dirac electrons at the surface of TIs. For this reason, these excitations are called Dirac plasmons. We will focus on a theoretical study of Dirac plasmons in nano-wires at the end of thesis.

The second chapter addresses the study of electronic properties of TIs from a theoretical point of view focusing on the compound  $Bi_2Se_3$ . We introduce a Hamiltonian based on the orbitals which contribute to surface states, considering in particular the limit of large wave lengths. The study starts from a description at the  $\Gamma$  point ( $k_x = k_y = 0$  momentum) analyzing the surface states. Within the perturbation theory, we construct the states and the spectrum providing an effective simplified Hamiltonian with which it is also possible to study spin properties of the electronic states. In particular, in the last section of the second chapter, we focus on a slab confined along the  $z$  direction, analyzing in particular the case when the thickness is so small such that the two surfaces are coupled (thin films). As predicted by experiments, some features of topological insulator are lost, in particular there is the opening of a gap at the Dirac point. We will provide the gap energy trend as a function of the thickness of the slab.

The last two chapters are the most original part of this thesis. Stimulated by the recent realization of three dimensional topological insulator nano-wire interferometers, a theoretical analysis of quantum interference effects on the low energy spectrum of  $Bi_2Se_3$  nano-wires is given in the third chapter. We will study in particular the effects of the cross-section shape and length. The electronic properties are analyzed in nano-wires with circular, square

and rectangular cross-sections starting from a continuum three dimensional model with particular emphasis on magnetic and geometrical effects. The theoretical study is based on numerically exact diagonalizations of the discretized model for all the geometries. In the case of the cylindrical wire, an approximate analytical solution of the continuum model is also discussed. Although a magnetic field corresponding to half quantum flux is expected to close the band gap induced by Berry phase, in all the studied geometries with finite area cross-sections, the gap closes for magnetic fields typically larger than those expected. Furthermore, unexpectedly, due to geometrical quantum interference effects, for a rectangular wire with a sufficiently large aspect ratio and smaller side ranging from  $50\text{\AA}$  and  $100\text{\AA}$ , the gap closes for a specific finite area cross-section without the application of a magnetic field. In the last chapter we present a theoretical analysis of Dirac magneto-plasmons in topological insulator nano-wires. By taking into account surface electron wave functions introduced in the third chapter and within the random phase approximation (RPA), we provide an analytical form of the dynamic structure factor. Plasmon dispersions and spectral weights are studied with varying the radius of the cylinder, the surface density, and the strength of an external magnetic field. We show that, at zero surface doping, inter-band Dirac plasmons form at the surface and survive at low electron surface densities ( $\sim 10^{10} \text{ cm}^{-2}$ ). Then, we point out that the plasmons are sensitive to the Berry phase gap closure when an external magnetic field close to half quantum flux is introduced. Indeed, a well-defined magneto-plasmon peak is observed at lower energies upon the application of the magnetic field. Finally, the increase of the surface density induces a crossover from inter- to intra- band magneto-plasmons which, as expected for large radii and densities ( $\sim 10^{12} \text{ cm}^{-2}$ ), approach the proper limit of a two-dimensional surface.

# Chapter 1

## Three-Dimensional Topological Insulators

The band theory was one of the first achievements of quantum mechanics in 1920s. It gave a simple explanation of how certain crystalline materials are insulators in terms of electrons that occupy eigenstates, forming energy bands. There are bands completely filled with electrons separated by an energy gap from completely empty bands. In contrast, materials with partially filled bands are conductors, where the chemical potential is in band and the electrons have the ability to move across the bulk.

The simple division into band insulators and metals, based on band theory, is not enough to explain some of the properties observed in quantum Hall systems (1980). The first major difference between a quantum Hall systems and an ordinary insulator is contained in the TKNN invariant (by Thouless, Kohmoto, Nightingale, and den Nijs, 1982) [1].

The Integer Quantum Hall Effect (IQHE) occurs when a two-dimensional electron gas is placed in a strong perpendicular magnetic field [2]. Then the quantization of the electron circular orbits leads to quantized Landau levels. If  $n$  Landau levels are filled and the rest are empty, then an energy gap separates the occupied and empty states just as in an insulator. However unlike an insulator, a Hall current is observed since an electric field causes

the cyclotron orbits to drift along the edges. Associated to these currents the Hall conductivity is quantized  $\sigma = ne^2/\hbar$ , where  $n$  is an integer. The model of TKNN shows that the  $n$  of the quantized Hall conductivity is a quantity related to the topology of the bulk that takes the name of Chern number. Only recently the scientific world turned its attention to a new class of 3D materials defined Topological insulators. They exhibit conductive surface states, residing in the bulk insulating gap, reminiscent of the edge states observed in quantum Hall effect. As in the case of IQHE, these surface states show a very interesting property: they are protected from impurity scattering. In 2007 the first TI, bismuth-antimony, has been discovered and after that in pure antimony, bismuth selenide, bismuth telluride and antimony telluride. Passing from a topological insulator to one trivial as for example the vacuum, the surface states are formed with special properties. Since the surface states are conductive their energy dispersion connects the valence band with the conduction band. In special points of degeneration of the electronic states, these bands have a linear dispersion forming a Dirac cone. In many of these TI the spin-orbit coupling is strong leading to special effect called spin-momentum locking, in fact the spin states will be always be perpendicular to the wave vector. Although both 2D and 3D topological insulators exist, in this work we will focus only on 3D TIs considering numerical and analytical study of their properties. In this chapter we will discuss the main features of a 3D topological insulator, introducing briefly the  $\mathbb{Z}_2$  invariant and the main experiments that have demonstrated the topological nature of surface states.

## 1.1 $\mathbb{Z}_2$ Topological Insulators

An order to clarify the topological properties of 3D TIs, is useful to start from two-dimensional electronic systems. The topologically nontrivial states of the integer quantum Hall occurs when time reversal symmetry is broken either by an external magnetic field or by magnetic order. However, it can

be shown that systems with strong spin orbit interaction (quantum spin Hall systems) are characterize by a different topological class of insulating band structures where time reversal symmetry is unbroken [3], leading to an interesting robustness to scattering for conductive edge states. In the following we will discuss the origin of this interesting property.

In the edge of most material, the electrons go both forward and backward without any preference. In order to reduce electron collision it could be very useful separate their motion in physically separate lines. IQHE is one way to make this condition happen at edge of the material. However, the IQHE occurs only when a strong magnetic field is applied to a two-dimensional gas of electrons in a semiconductor. Electrons will only travel along the semiconductor edges at low temperature and strong magnetic field. Another way to obtain the same results is to use quantum spin Hall systems.

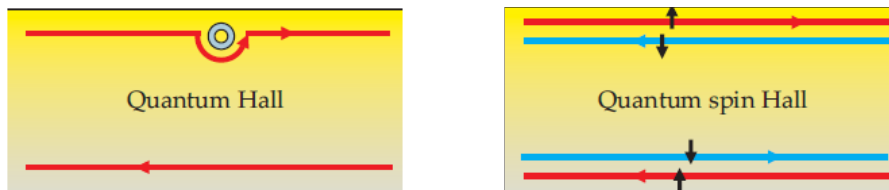


Figure 1.1: The spatially separated movement of one dimensional spinless chain in quantum Hall and one dimensional spinfull chain in quantum spin Hall.

In Figure 1.1, we compare the edge state properties of quantum Hall and quantum spin Hall systems. The most important aspect of quantum Hall effect and quantum spin Hall effect is spatial separation of electron movement. In the left part of Figure 1.1, we can see the one dimensional electron chain moves forward and backward is the separately on the two edges. On the upper edge, the electrons only move forward and the electrons on the lower edge move only backward. This is the key reason why the IQHE is topologically robust, for the electron will go around an impurity without scattering. This is extremely useful but it requires a strong magnetic field, which limits the potential practical applications of the quantum Hall

effect. In quantum spin Hall, instead the forward and backward moving channels will split into four channels with spin-up and spin-down electrons in both direction, which is shown in the right part of Figure 1.1. We can leave the spin-up forward electrons and spin-down backward electrons at the top edge and the other two on the bottom edge. The backscattering due to the presence of non magnetic impurities are forbidden on both the top and bottom edges. This can be understood with the following argument. When an electron is scattered by a nonmagnetic impurity, the directions can be of two types: clockwise when spin is rotate by  $\pi$ , and the other one is counterclockwise with spin rotation by  $-\pi$ . The two path, related by time reversal symmetry, differ by a full  $2\pi$  rotation of electron spin. Thus the two backscattering paths always interfere destructively which leads to perfect transmission. If the impurity carries a magnetic moment, the time reversal symmetry is broken and the two reflected waves do not interfere destructively [4].

The fact that the edge states of the quantum spin Hall insulator are robust without a magnetic field suggests that there must be a topological distinction between the quantum spin Hall insulator and an ordinary insulator. The key to understanding this new topological class is to examine the role of time reversal symmetry  $\mathcal{T}$  for spin 1/2 particles. The  $\mathcal{T}$  is represented by an anti-unitary operator  $\Theta = \exp(i\sigma_i/\hbar)\mathcal{K}$  where  $\sigma_i$  is the spin operator along a general  $i$  direction and  $\mathcal{K}$  is complex conjugation. For spin 1/2 electrons,  $\Theta^2 = -1$ . This leads to an important constrain known as Kramers theorem, which claims that all eigenstates of a  $\mathcal{T}$  invariant Hamiltonian are at least twofold degenerate [5]. In the absence of spin orbit interaction, the Kramers degeneration is simply given by spin up and down degeneration. In the presence of spin orbit the consequences are less obvious. In Figure 1.2 we show the electronic states associated with the edge of a  $\mathcal{T}$  invariant 2D insulator as a function of the crystal momentum along the edge. Only half of the Brillouin zone is shown because  $\mathcal{T}$  symmetry requires that the other half is a mirror image. The shaded regions depict the bulk conduction and

valence bands separated by an energy gap.

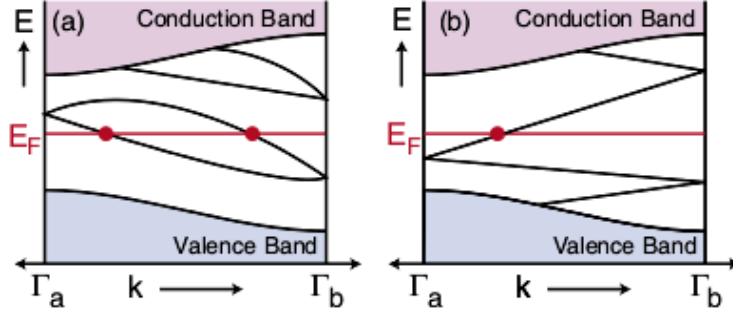


Figure 1.2: Electronic dispersion between two boundary Kramers points. In (a) the number of surface states crossing the Fermi energy  $E_F$  is even, whereas in (b) it is odd. An odd number of crossings leads to topologically protected metallic boundary states.

Depending on the details of the Hamiltonian near the system edge there may or may not be bound states whose associated energy is inside the gap. If they are present, however, then Kramers theorem requires they be twofold degenerate in the  $\mathcal{T}$  invariant momenta  $\Gamma_a$  and  $\Gamma_b$ . Away from these special points a spin orbit interaction will split the degeneracy. There are two ways the splitted states can be connected  $\Gamma_a$  and  $\Gamma_b$ . In Figure 1.2(a) they connect pairwise: in this case the systems can be made insulating by changing properly the Fermi energy. The bands intersect  $E_F$  Fermi level an even number of times. In contrast, in Figure 1.2(b) the edge states exhibits the metallic behavior topological protected and connecting the valence and conduction bands. The bands intersect  $E_F$  an odd number of times. These alternatives depend on the topological class of the bulk band structure. Since each band intersecting  $E_F$  at  $k$  has a Kramers partner at  $-k$ , the bulk-boundary correspondence relates the number  $N_k$  of Kramers pairs of edge modes intersecting  $E_F$  to the change in the  $\mathbb{Z}_2$  invariant across the interface:

$$N_k = \nu \text{ mod } 2, \quad (1.1)$$

where  $\text{mod } 2$  we intend modulo  $\nu$  in base 2. For  $\nu = 0$  we have a normal

insulator otherwise if  $\nu = 1$  the insulator is topological. Hence the name  $\mathbb{Z}_2$ .

The  $\mathbb{Z}_2$  invariant for three-dimensional crystals can be discussed in terms of two dimensional problem [6]. The three-dimensional Brillouin zone can be rolled into a donut along the x- and y-direction as illustrated in Figure 1.3(a). Similarly, the topological invariant characterizing a two-dimensional band structure may be constructed by rolling a two-dimensional system into a cylinder, which returns the edge time reversal invariant momenta as in Figure 1.2. For three-dimensional systems there are eight time reversal invariant momenta:

$$\Gamma_{i=(n_1, n_2, n_3)} = \left( \frac{n_1}{2} \mathbf{G}_1 + \frac{n_2}{2} \mathbf{G}_2 + \frac{n_3}{2} \mathbf{G}_3 \right) \quad (1.2)$$

where  $\mathbf{G}_i$  are the vectors of the reciprocal lattice pattern and  $n_i = 0, 1$ . They can be viewed as vertices of a parallelepiped as in Figure 1.3(b). If we fix an index  $n_i$  and we leave the other two free, we define a two-dimensional Brillouin zone of a two-dimensional system respecting time reversal symmetry, for which a  $\mathbb{Z}_2$  invariant can be calculated from the method for two-dimensional system, referred as  $\nu_{n_i}$ . For example if  $\nu_{n_1} = 1$  then the are other five invariants  $\nu_{n_1=0}, \nu_{n_2=0,1}$  and  $\nu_{n_3=0,1}$ . These six invariants are associated with six planes of the parallelepiped in Figure 1.3(b). Since they belong to the same three-dimensional crystal, only four of them are independent (because are the four vertices). The four independent invariants can be chosen as, say,  $\nu_0 = \nu_{n_1=0} \cdot \nu_{n_1=1}$ ,  $\nu_1 = \nu_{n_1=1}$ ,  $\nu_2 = \nu_{n_2=1}$  and  $\nu_3 = \nu_{n_3=1}$  [7–9]. Thus a 3D topological insulator is characterized by four  $\mathbb{Z}_2$  topological invariants  $(\nu_0; \nu_1 \nu_2 \nu_3)$ . The states of the surface of this insulating can be labeled with a 2D Brillouin zone where there are four invariants momenta points, which must be Kramers degenerate. As in Figure 1.2, even for the equivalent two dimensional in momentum space for the surface, we have special points  $(\Lambda_{1,2,3,4}$  for 2D B.z.) time reversal invariant momenta. These Kramers degenerate points therefore form 2D Dirac points in surface band structure. It is useful to understand how these points are connected to each other, in fact, as before they can cross the Fermi surface an even or odd number of times.

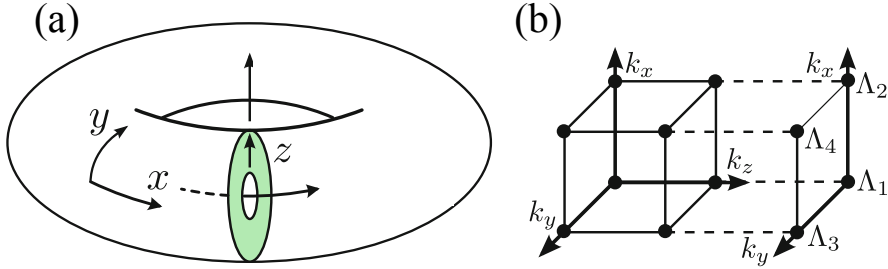


Figure 1.3: (a) Starting from a two-dimensional system (the crown in green), in three dimensions the Brillouin zone can be rolled into a donut. (b) The four time reversal invariant ( $\Lambda_{1,2,3,4}$ ) correspond to the four two-dimensional surface momenta.

This depends on the value of the four invariant  $\mathbb{Z}_2$ . The four  $\mathbb{Z}_2$  invariants are able to identify different classes that can be grouped in two main categories associated to weak (WTI) and strong (STI) topological insulators. These two more general classes are characterized by the value of the first invariant,  $\nu_0 = 0$  [10, 11] and  $\nu_0 = 1$  [9] are associated to WTI and STI, respectively. Only in the second case the surface states are topologically protected from disorder [12, 13]. An example of WTI can be viewed as a stack of weakly coupled 2D quantum spin Hall insulator layers. If  $\nu_0 = 1$  then the topological phase identifies a STI, which cannot be interpreted as a descendant of the 2D quantum spin Hall insulator. The surface states of a STI form a 2D topological metal [14, 15] different from that obtained 2D quantum spin Hall insulator. This particular value of  $\nu_0$  determines a Fermi surface circle that encloses an odd number of Kramers degenerate Dirac points. Unlike an ordinary metal, which has up and down spins at every point on the Fermi surface, the surface states of a STI are not spin degenerate. In fact the  $\mathcal{T}$  symmetry requires that states at momenta  $k$  and  $-k$  have opposite spin, the spin must rotate with  $k$  around the Fermi surface. A further consequence of the spin momentum-locking is related to the presence of a Berry phase for the surface states. There is a non trivial Berry phase acquired by an electron going around the Fermi circle, in particular this phase must be  $\pi$ . More de-

tails on the Berry phase are given in Appendix A. We stress that this phase plays an important role in TI nano-wires, in particular when a magnetic field is present.

## 1.2 Type of 3D topological insulators and experiments

The first 3D topological insulator to be experimentally discovered was the semiconducting alloy  $Bi_xSb_{1-x}$ , whose unusual surface bands were mapped in ARPES experiment. Bismuth antimony alloys have long been studied for their thermoelectric properties. Bismuth is a semimetal with strong spin-orbit interactions. Its band structure has an indirect negative gap between the valence band maximum at the  $T$  point of the bulk Brillouin zone (B.z.) and the conduction band minima at three equivalent  $L$  points [16]. The surface of the bismuth antimony alloys is a new form of 2D metal where electron's spin and linear momentum are locked one to one and the two dimensional Fermi surface carries a nontrivial Berry's phase of  $\pi$  [9].

ARPES uses a photon to eject an electron from a crystal, then determines the surface or bulk electronic structure from an analysis of the momentum of the emitted electron. Unlike a transport experiment, this method carried out in a spin resolution mode can, in addition, measure the distribution of spin orientations on the Fermi surface which can be used to estimate the Berry phase on the surface. Spin sensitivity is critically important for probing the existence of spin-momentum locking on the surface expected as a consequence of bulk topological order. At an  $Sb$  concentration of  $x \sim 4\%$  the gap closes, instead as  $x$  is further increased this gap re-opens with inverted symmetry ordering, which leads to a loss of energy in the gap which generates a Dirac point [5]. Linearly dispersive bulk bands which are uniquely consistent with strong spin-orbit coupling nature of the inverted insulator also occurred. In general, the states at the surface of spin-orbit coupled compounds are allowed to be spin split owing to the loss of space inversion symmetry, i.e.

$E(k, \uparrow) = E(-k, \downarrow)$ . However, this splitting must go to zero at the four time reversal invariant momenta in the 2D surface B.Z. as required by Kramers theorem. When there are an even number of surface state crossings, the surface states are topologically trivial because weak disorder (as may arise through alloying) or correlations can remove pairs of such crossings by pushing the surface bands entirely above or below  $E_F$ . When there are an odd number of crossings, however, at least one surface state must remain gapless, which makes it non-trivial. The measured spin texture of the alloy reveals the existence of a nonzero geometrical quantum phase, a Berry phase of  $\pi$  and the chiral properties.

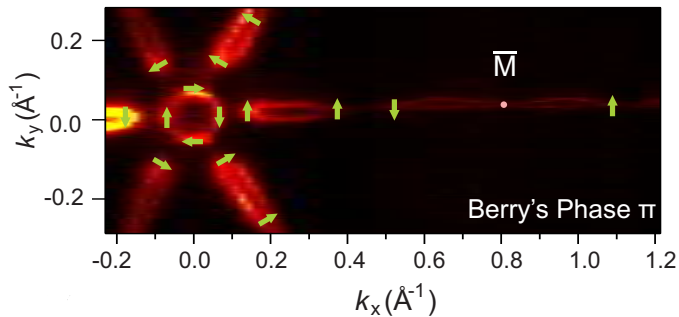


Figure 1.4: Topological surfaces exhibit non-trivial spin-textures. Spin-resolved photoemission directly probes the topological character of the spin-textures of the surface. A schematic of spin-ARPES measurement set up is shown which was used to measure the spin distribution mapped on the surface Fermi surface of  $Bi_{0.91}Sb_{0.09}$ . Spin orientations on the surface create a vortex-like structure around  $\Gamma$ -point. A net Berry phase  $\pi$  is extracted from the full Fermi surface.

Scanning tunneling spectroscopy (STM/STS) and spin-ARPES technique enable to investigate aspects of the metallic regime, which are necessary to determine the microscopic origin of topological order [17]. Repeating once, odd number of Fermi crossings protects the topological surface from becoming insulating, regardless of the position of the chemical potential or the influ-

ence of non-magnetic perturbations. Furthermore, they have established that these surface states have a particular chiral spin structure as shown in Figure 1.4. All these characteristics suggest that backscattering, or scattering between states of equal and opposite momentum, which results in Anderson localization in typical low-dimensional systems [18], will not occur for these two-dimensional carriers. The results show that despite strong atomic scale disorder and random potential, elastic-backscattering between states of opposite momentum and opposite spin is absent. These observations demonstrate that the chiral nature of these states protects the spin of the carriers which is ultimately a consequence of time-reversal symmetry. The same conclusion has emerged from studies of the electronic interference patterns near defects or steps on the surface that electrons never turn completely around when scattered in other topological insulators [19]. Study the  $Bi_{1-x}Sb_x$  alloy material is rather complicated especially from the experimental point of view, having a small gap energy. In topological insulators with larger band gap and simpler surface spectrum for observing topological phenomena at high temperatures. Generally topological phenomena in materials are usually very fragile and impossible to be observed, except through low temperatures and strong magnetic fields. The unusual planar metal that forms at the surface of topological insulators inherits topological properties from the bulk band-structure. The manifestation of this bulk-surface connection occurs at a smooth surface where momentum along the surface remains well-defined. Indeed each momentum along the surface has only a single spin state at the Fermi level, and the spin direction rotates as the momentum moves around the Fermi surface ensuring a non-trivial Berry phase. These two defining properties of topological insulators namely spin-momentum locking of surface states and the Berry phase along with the consequences such as the robustness to non-magnetic disorder are most clearly demonstrated with the discovery of the second generation of topological insulators. New three-dimensional 'topological insulator' materials, especially  $Bi_2Se_3$ , offer the potential for protected surface states and other topological behav-

ior at room temperature. The main characteristic of the surface states energy, for a topological insulator, is the formation of a Dirac-cone. Each momentum along the surface has only a single spin state at the Fermi level, and the spin direction rotates as the momentum moves around the Fermi surface ensuring a non-trivial Berry phase. A Princeton group used ARPES and first-principles calculations to study the surface band structure of  $Bi_2Se_3$  and observed the characteristic signature of a topological insulator in the form of a single-Dirac-cone as in Figure 1.5 [5]. The compound  $Bi_2Se_3$  [20, 79] is just one of several new large band gap topological insulators. Detailed and systematic surface investigations of  $Bi_2Te_3$  [22, 79] and  $Bi_2Te_3$  [22] together with  $Bi_2Se_3$  confirmed the topological band-structure of all 3 of these materials. Even if alloy  $Bi_{1-x}S_e_x$  and  $Bi_2Te_3$  have the same properties and topological class, the best candidate for the experiments remains  $Bi_2Se_3$ .

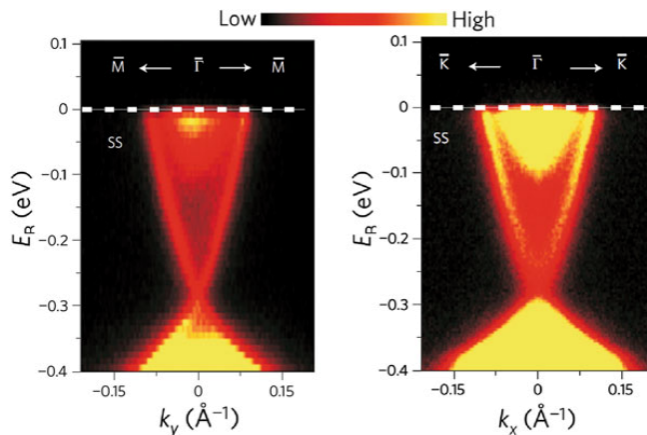


Figure 1.5: High-resolution ARPES data of surface electronic band dispersion on  $Bi_2Se_3$  plane measured with an incident photon energy of 22 eV near the  $\Gamma$  point along the  $\Gamma \rightarrow M$  and  $\Gamma \rightarrow K$  momentum-space cuts.

In fact, its surface state is found from ARPES and theory to be nearly the idealized single Dirac cone as seen from the experimental data in Figure 1.6. Then  $Bi_2Se_3$  is a pure compound rather than an alloy and hence can be prepared in principle at higher purity. For this in its high purity form, the large band gap of this material indicates that topological behavior can be seen at

room temperature and greatly increases the potential for applications. Not only for the temperature but also for its large band gap of approximately 0.3 eV, this semiconductor is the ideal to study. Therefore, all the key properties of topological states have been demonstrated for  $Bi_2Se_3$  which has the most simple Dirac cone surface spectrum and the largest band gap (0.3 eV).

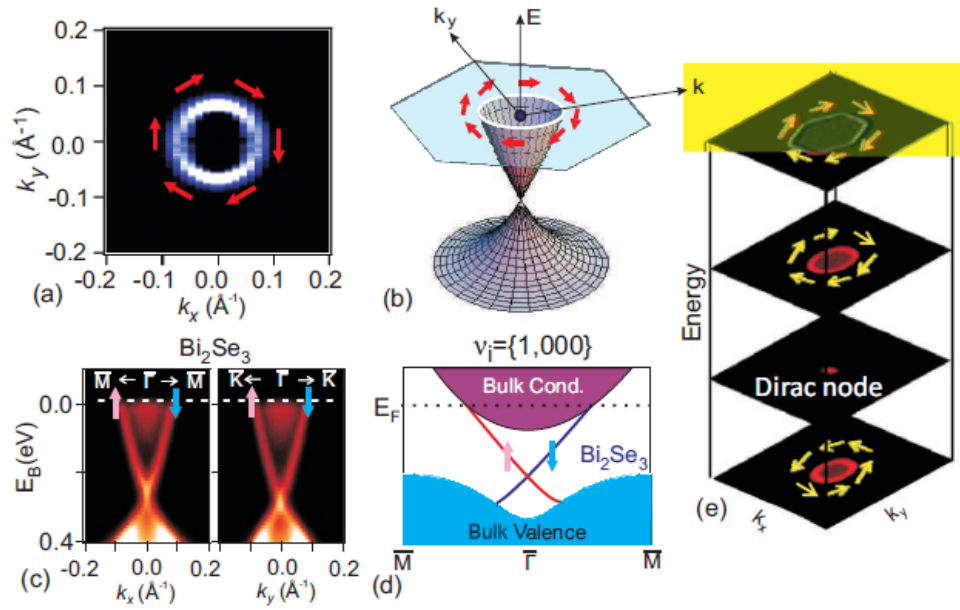


Figure 1.6: (a) Surface dispersion relation of electronic states reveal a spin perpendicular to the direction of the moment. (b) Around Surface Fermi there are surface that exhibits chiral left-handed spin textures. Schematic presentations of (c) surface and bulk band topology and (d) a single spin-polarized Dirac fermion on the surface of a generic  $Bi_2X_3$ . For negative  $k$  spins are inverted but also for the same sign of  $k$  below the node-Dirac (e) reverses the direction of rotation of the spin polarization.

Summarizing, properties of topological insulators namely spin-momentum locking of surface states and  $\pi$  Berry phase could be clearly demonstrated by experiments. Topological surface states are protected by time reversal symmetry which implies that the surface state Dirac node would be robust

in the presence of non-magnetic disorder but opens a gap in the presence of time-reversal breaking perturbation of the system such as the effect of magnetic impurities and the associated disorder. All views properties in the experiments above, are related to materials which have an extensive volume than the surface. If we begin to confine much, at least one dimension, is possible to observe particular characteristics.

Thin film of three-dimensional topological insulator may provide an alternative way to realize the quantum spin Hall effect. It is an example to reduce a three-dimensional topological insulator to two-dimensional topological insulator. The surface states have spatial distribution, which can be characterized by a length scale. When this length scale is comparable with the thickness of the thin film, the wave functions of the two surface states from top and bottom surfaces will overlap in space.

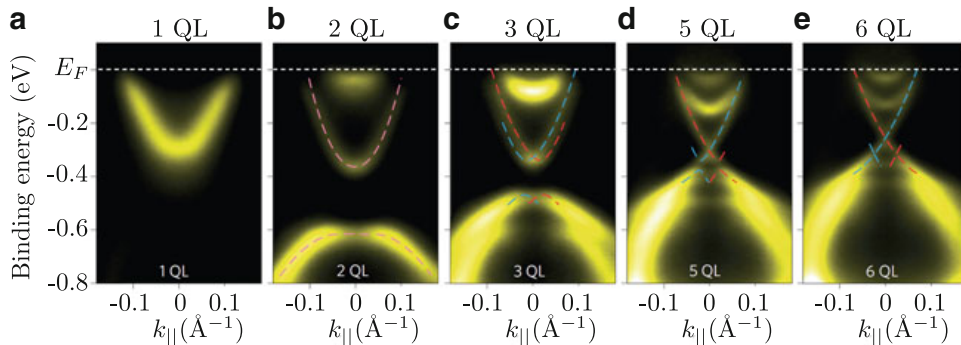


Figure 1.7: ARPES spectra of  $Bi_2Se_3$  thin film at room temperature. (a)-(e) ARPES spectra from one to six quintuple layer (QL) along  $\Gamma - K$  direction of the B.z.

If the two surfaces of the slab are sufficiently far, there is no coupling between the wave functions and the gap is closed again, restoring the Dirac cone. The thickness-dependent band structure of molecular beam epitaxy grown ultra-thin film  $Bi_2Se_3$  was investigated by ARPES by several groups [23, 24] as in Figure 1.7. The energy gap due to the interlayer coupling has been observed experimentally in the surface states of ultrathin film  $Bi_2Se_3$  below

the thickness of  $6\text{ nm}$  (namely 6 Quintuple Layers (QL), each 3 QL is a periodic cell of the lattice of  $\text{Bi}_2\text{Se}_3$ ). The gap of the surface states is caused exclusively by the spatial confinement of thin film, which does not break time reversal symmetry. This is different from the gap opening of the surface states in a Zeeman field or magnetic impurity doping.

Similarly to the case of the film, it is possible to study the electronic properties of a wire, confining in two different directions in the real space. We have in this way a single carrier wave  $k$  with the consequent formation of a number of sub-bands, result of the old Dirac cone in the space of two-dimensional moments. Also in this case it will be observed the opening of a gap, but of a different nature compared to the case of the film. In fact, the effect of this opening is attributable to the phase of Berry (see appendix A) and not to the size effects. Even if we increase the size of the perimeter of the section of the wire, only to infinite lengths will restore the closure of the gap. In fact in this case the closure is achieved only for interference effects. Applying a weak magnetic field and it is observed experimentally by measurements of magnetic-conductance [25]. This concept will be widely discussed by theoretical point of view in the third chapter of this thesis.

### 1.2.1 Transport experiments

An important aspect for these materials is the study of the transport properties. Despite the success of photoemission and scanning tunneling spectroscopy in identifying chiral surface states, signatures of the surface Dirac cone have been slow in being recognized in the field of transport. We repeat that the band structure of topological insulators can be visualized as a band insulator with a Dirac cone within the bulk gap, and to access this cone one needs to ensure the chemical potential lies in the gap. Essentially the strong inconvenience for transport measurements of the surface of these materials are due to the bulk effect. One expects to see in a sample transport measures in which the contribution of the bulk have been eliminated. In the initial

experimental efforts, it appeared impossible to identify any signatures whatsoever of the elusive surface states. Here we propose a series of experimental analysis conducted on different TI nano-structures, for the study of transport to the surface of these materials. One early avenue toward the removal of bulk carriers involved compensation by doping with  $Ca$ , in Ref. [26] the experimental group performed transport experiments on  $Ca$ -doped samples noting an increase in the resistivity, but concluded that surface state conduction alone could not be responsible for the smallness of the resistivities observed at low temperature. Same group noted surface conduction, inferred from the sign change in the Hall coefficient. Such a sign change would indicate a change in the carrier type from electrons to holes, and therefore the fact that the Dirac point has been crossed [27]. An other important experiment focused on  $Bi_2Se_3$  in a magnetic field [28], performing far-infrared and mid-infrared reflectance and transmission measurements, supplemented with UV-visible ellipsometry to obtain the optical conductivity. Temperatures of 6-295 K and magnetic fields of 0-8 T has been studied. The Fermi surface was located away from the Dirac point due to residual doping. The sample was studied in magnetic fields oriented in general directions and the most changes in spectral weight involve a reshuffling of weight between the Drude and optical phonon. As the temperature decreased, the Drude conductivity was found to narrow due to reduced quasiparticle scattering. At the same time, an increase in the absorption edge due to direct electronic transitions was identified. These results are interpreted as evidence for magneto-electric coupling in  $Bi_2Se_3$ . In agreement with ARPES measurements, in [29] have analyzed various samples of which some were metallic and some had a high bulk resistivity. Selective cleaving resulted in non-metallic crystals. Though in  $Bi_2Te_3$  the chemical potential lies in the bulk valence band, they were able to manufacture both n-and p-type samples, which suggests a degree of competition and compensation between the bulk valence and conduction bands. Data from the weak-magnetic field Hall effect yield a surface mobility of 9000-10,000  $cm^2$  per volt-second and substantially higher than in

the bulk. In non-metallic samples, the SdH oscillation (Shubnikov-de Haas effect, oscillation in the conductivity that occurs at low temperatures in the presence of very intense magnetic fields) period depends only on the perpendicular magnetic field, with oscillations not resolved for magnetic field tilt angles  $q$  in the range  $65^\circ < q < 90^\circ$ . The oscillations in the metallic sample survive up to  $90^\circ$ . The Fermi velocity of  $4 \times 10^5$  meters per second obtained from these transport experiments agrees with angle-resolved photoemission experiments. Even though the surface mobility is calculated to be very large and to exceed the bulk, even in the most resistive sample, the bulk conductance exceeds the surface conductance by a factor of about 300. One key aim of current TI efforts is the identification of a definitive signature of surface transport. Several recent experimental works [30, 31] point to a possible way forward, at least in the detection of surface transport, if not a permanent solution to the bulk doping problem. Coexisting bulk and surface transport remains a relevant problem to TI experiments at present, and it will be so until the scientists will be able to produce a material that does not require gating in order to shift the chemical potential into the bulk gap, in order to observe only the surface electron gas. One way to solve the problem is to try to reduce the bulk contribution through for example a thin films.

In some works [32, 33] on thin films, transport measurements have shown better the character of the surface states of  $Bi_2Se_3$ . Weak anti-localization (WAL) is always expected in systems with either strong spin orbit scattering or coupling. WAL is quantum interference effect in quantum transport in a disordered electron system, it enhances the conductivity with decreasing temperature at very low temperatures. This phenomenon is present in systems in which the spin of the carrier rotates as it goes around a self-intersecting path, and the direction of this rotation is opposite for the two directions about the loop. Because of this, the two paths interfere destructively which leads to a lower net resistivity. The WAL is protected against the strength of disorder and nonmagnetic impurity. Two single crystal thin films of  $Bi_2Se_3$ , grown

by Molecular Beam Epitaxy (MBE), both with and without *Pb* doping were considered in [32]. After doping, ARPES by [34] shows that the Fermi level of the  $Bi_{2-x}Pb_xSe_3$  film was inside the bulk energy gap.

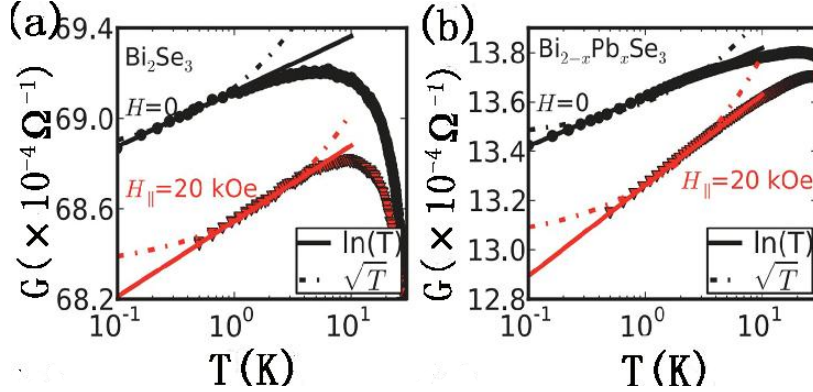


Figure 1.8: Conductance measurements as a function of temperature  $T$ . The lines are fits to the 2D(solid) and 3D(dashed) of the theory in [36] by the EEI theory.

Thus, the bulk conductivity should be suppressed and the surface conductance should come into evidence. So, it is observed the conductance as a function of temperature and magnetic field for the  $Bi_2Se_3$  and  $Bi_{2-x}Pb_xSe_3$  films. In this case is considered for fit of the experimental data an electron-electron interaction (EEI), weak anti-localization (WAL) and anisotropic magnetoresistance (AMR) effect. For example in the Figure 1.8 is shown a case in which there was measured the conductance as temperature dependent, by fitting the data with a EEI theory. The EEI expressions [36] correctly reproduce the signs of the  $T$  dependence. These results clearly demonstrate that it is crucial to include EEI for a comprehensive understanding of diffusive transport in TIs. Both the ordinary bulk and the topological surface states presumably participate in transport as shown in Figure 1.8 by the theoretical lines 2D (solid) and 3D (dashed). This analysis does not allow a clear separation of the two contributions, but they are observed both.

Relevant for this thesis is to observe transport properties in nano-wires of a topological insulator. We stress that on the surface of topological insulators (TI), electron spin is locked perpendicular to momentum, resulting in the suppression of electron backscattering from nonmagnetic impurities. Such spin textured surface states have been studied extensively by surface probing techniques such as ARPES and STM [37]. In a TI nano-wire device, the Aharonov-Bohm (AB) effect, quantum interference of surface state electrons winding around the nano-wire, offers a unique opportunity to detect topological protection in the helical surface electrons. An important difference of TI nano-wires from carbon nanotubes is the existence of a spin Berry phase. Along the TI nano-wire perimeter, the electron spin rotates by a  $2\pi$  angle due to the spin-momentum locking nature of electrons, leading to a Berry phase of  $\pi$ .

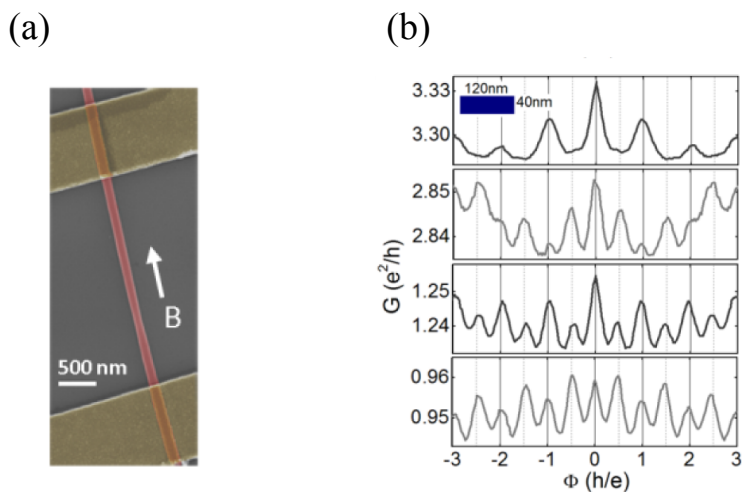


Figure 1.9: Magneto-conductance from TI nano-wire 1D modes of surface electrons: far above the Dirac point. (a) A representative image of devices (false-colored scanning electron microscope image). (b) Magneto-conductance oscillations at four different gate voltages ( $V_G = -40 V, -45 V, -85 V, -95 V$ ). Inset: the cross section of the nano-wire ( $120 nm \times 40 nm$ ).

The experiment in [25] observes a topologically protected 1D mode of surface electrons in topological insulator nano-wires existing at only two values of half magnetic quantum flux ( $\Phi = \pm\hbar/2e$ ) due to a spin Berry phase. With the aid of a magnetic field of generic direction respect the axis of the wire, the experiment shows, through magnetic-conductance measurements, how the helical 1D mode is robust against disorder but very weak against a perpendicular magnetic field, breaking-time-reversal symmetry. The 1D bands and their density of states (DOS) is subject to periodic oscillations by magnetic flux, resulting in magneto-oscillations of  $\Phi = \hbar/e$  period as already known [39, 60]. These oscillations are due essentially to the parabolic 1D bands and they are associated effect AB by ordinary (no topological) electrons. However, a specific value of magnetic flux ( $\Phi = \pm\hbar/2e$ ,  $\Phi = \pm3\hbar/2e, \dots$ ) eliminates the contribution of the phase of Berry. The experiment is conducted through the three phases to demonstrate the topological nature of the surface electrons via transport measures. A first case takes, in Ti nano-wires, the Fermi level approaches to the Dirac point, they observe large conductance peaks at  $\Phi = \pm\hbar/2e$ . Second case, they induce a strong disorder in the material for which the helical 1D electron states are protected by time reversal symmetry, so in this way peaks are detected always at  $\pm\hbar/2e$ . Finally, by applying perpendicular magnetic fields, they find that the helical 1D mode peaks from disordered nano-wires are fragile to time reversal symmetry breaking, meaning topological nature directly related to time reversal symmetry. All cases are taken with temperatures ranging from  $T = 2K - 30K$ . Of course the nature of the conductance peak is very dependent on the Fermi level position. The device Fermi level can be tuned by back gating to reach the Dirac point [40, 41], but the electrostatic gating usually results in a slight difference of top and bottom surfaces Fermi level [42]. The 1D band gap is determined by the nano-wire perimeter that is generally considered in the range of  $L = 100 - 450 \text{ nm}$ , for these lengths they get the largest gap energy ( $15 - 17 \text{ meV}$ ). Thus, varying the gate potential are obtained different features of the conductance as in Figure 1.9. As the

Fermi level crosses multiple 1D sub-bands, the change of DOS induced by the magnetic flux (one sub-band DOS) is much smaller than the total DOS (entire sub-bands DOS), resulting in small oscillation amplitude. Of course also they are observed oscillation peaks for integers of quantum flux  $\hbar/e$ . The oscillation peaks are at either integer quantum flux or half quantum flux is the signature of 1D band effect made of surface electrons, when the Fermi level is far above from the Dirac point. These experimental results are explicitly predicted by the 1D DOS theory of TI nano-wires [43].

### 1.2.2 Collective electronic excitations: Dirac surface plasmons

Another way to study the problem from the electronic point of view on the surface of these materials is to study the response of the system in terms of collective excitations to the surface. Plasmons are collective charge density oscillations, which occur due to long-range Coulomb interactions and have been observed in metals and doped semiconductors. The study of these excitations is of particular interest for several practical applications, such as for example the capacity it offers to locate light on the metal surfaces and interfaces in the sub-wavelength regions. Even for TI the plasmons can be studied, their resonance frequencies are in the mid-infrared and terahertz spectral regions, which can be tuned by varying the Fermi level [18] or the wave vector. The most important aspect is due to the spin-momentum locking, in fact these plasmons are always accompanied by transverse spin oscillations and are thus also called "spin-plasmons" [44]. This would be a major step forward in quantum mechanics and spintronic applications. Only recently plasmons of massless Dirac electrons were observed in graphene for purely two-dimensional systems [45]. To observe the nature of the surface of these materials is necessary that the chemical potential is in gap. The experimental problem for the observation in these materials is given by the impurities and the level of doping that bring the chemical potential in the bulk bands. Another additional difficulty for the observation of these plasmons is due to

the fact that cannot be observed directly through an electromagnetic radiation because the moment conservation is prevented from their dispersion law.

The first experimental evidence of the surface plasmon excitation in TI compound  $Bi_2Se_3$  is shown in the in [46] using infrared spectroscopy and a more recent in the work present in [47] via high-resolution electron energy loss spectroscopy. In the experimental work [46], for coupling the electromagnetic radiation, the thin films of  $Bi_2Se_3$  were patterned in the form of micro-ribbon arrays of different widths  $W$  and periods  $2W$  as in Figure 1.10, so that a series of discrete values of  $k = \pi/W$  were obtained. It was measured in the paper the transmittance of films for different length of  $W$  and therefore the corresponding extinction coefficient for the patterned films. The interesting case to detect the plasmon is one in which there is a field perpendicular applied to the direction of the ribbons.

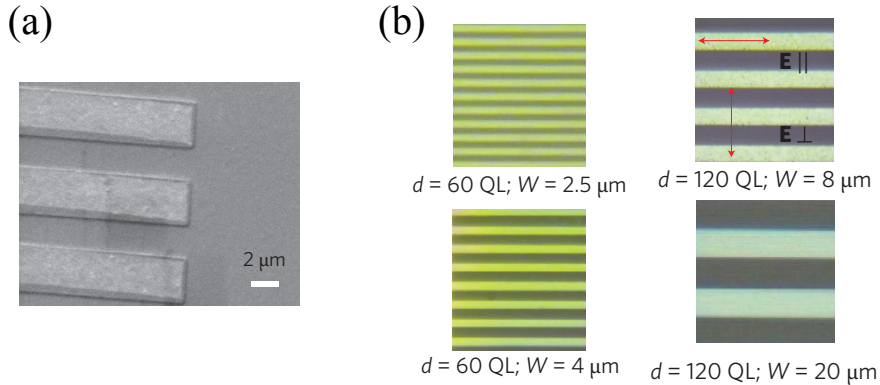


Figure 1.10: (a) Scanning electron microscope (SEM) image of the  $W = 2.5\mu m$  patterned film. (b) Optical microscope images of the five patterned films with different widths  $W$  and periods  $2W$ . Red arrows indicate the direction of the radiation electric field that either perpendicular or parallel to the ribbons. Film thickness is indicated under the images, where 1 QL is 1 nm (QL, quintuple layers).

The direction is the same as that of the reciprocal-lattice vectors needed

for energy-momentum conservation in the transmittance measurement. The excitation peaks are given by a double absorption as in Figure 1.11(a), which depend on the value of the length of  $W$ . It attributes these features to the  $\alpha$  phonon and to the plasmon of  $Bi_2Se_3$ , mutually interacting via a Fano interference.

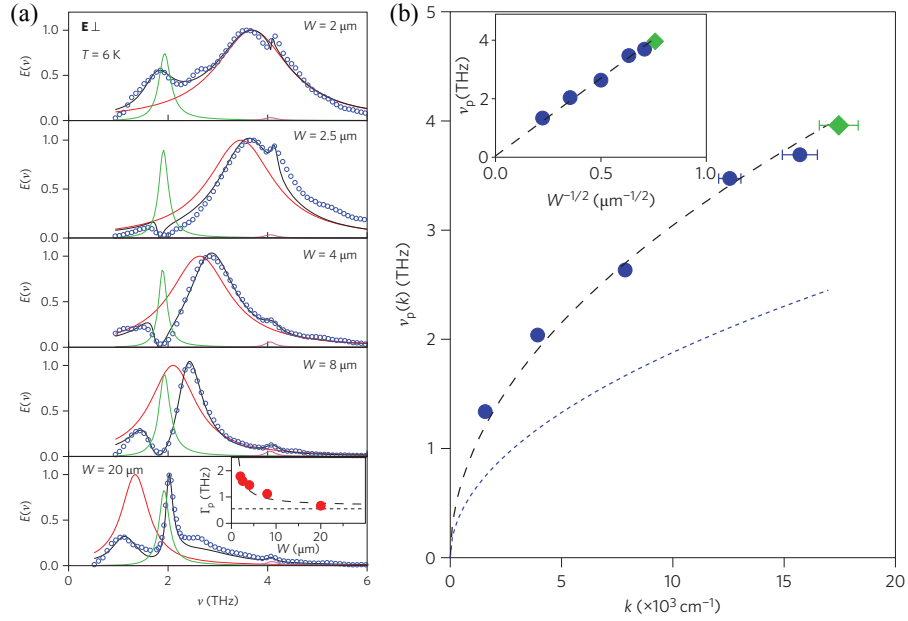


Figure 1.11: (a) Extinction coefficient  $E(\nu)$  versus frequency  $\nu$  for the five patterned films, for the radiation electric field  $E$  perpendicular to the ribbons, at  $6\text{ K}$  (circles), notice the good data agreement with the fit function found in the work (black lines) in [46]. Plasmon and phonon contributions, extracted through the fits, are shown by the red and green lines, respectively. In inset is shown the width at half height of the plasmon peak as a function of the width  $W$ . (b) Experimental values of  $\nu_p$  versus  $k$  at  $6\text{ K}$  (blue circles) compared with the plasmon dispersion for Dirac (dashed black line) and massive (dotted blue line) electrons. Inset: linear dependence of  $\nu_p$  on  $W^{-1/2}$ , where  $W = \pi/k$  is the ribbon width.

This implies a response given by two peaks, one at a lower frequency and a higher frequency. It is extracted the plasmon frequency through a fit of the

experimental data, as shown by the black lines in Figure 1.11(a). The figure shows that the phonon frequency (green line) does not change with  $W$ , while the plasmon contribution is distinct from the rest (red line). At this point, it is possible to find the plasmon frequency for each value of the vector  $k$ . As shown in Figure 1.11(b) the frequencies are plotted versus the wave-vector  $k$  and versus  $W^{-1/2}$  in inset. It is proved that the plasmon dispersion associated with the frequencies found are in good agreement with  $\nu_p \propto \sqrt{k}$ . In this way it is shown that the two-dimensional plasmon can be ascribed to the Dirac (massless) fermions, rather than to massive electrons also present at the surface.

Of course, always remains the problem, as already anticipated, to distinguish the contribution of the bulk plasmons with those of the surface. The surface conductivity of three-dimensional topological insulators is often overwhelmed by the bulk conductivity due to doping introduced by natural defects. Nanoscale topological insulators have a large surface-to-volume ratio, thus enhancing the contribution of the surface state. Plasmons in nanostructured topological insulators, such as thin films, multilayers, and nanoribbons, are essential for future applications. For low parallel momentum transfer  $q$ , the loss spectrum shows a distinctive feature peak which varies weakly with  $q$ . The behavior of its intensity as a function of primary energy and scattering angle indicates that it is a surface plasmon. At larger momenta, an additional peak, attributed to the Dirac plasmon, becomes clearly defined in the loss spectrum. The momentum-resolved loss spectra provide evidence of the mutual interaction between the surface plasmon and the Dirac plasmon of  $Bi_2Se_3$ . In particular, in Ref. [47] distinguishes the contribution given by bulk massive plasmon and Dirac surface plasmon.

## Chapter 2

# Hamiltonian models for topological insulator $Bi_2Se_3$

All the conditions for a topological insulator discussed in the previous chapter are addressed in a theoretical model in the first section of this chapter. In particular, the study will be directed to the compound  $Bi_2Se_3$ , whose electronic structure is studied. Relevant states for which we discuss the wave functions and the associated bands are  $p_z$ . Once constructed the effective Hamiltonian, a Dirac equation will be derived and the bands and the states for both surface and bulk will be discussed. In second section, a simplified model for  $k_x = k_y = 0$  ( $\Gamma$  point) will be considered, thus finding in a trivial way the states of the surface and the analytical form of the associated energy associated. Through the perturbation theory, one has the possibility to extrapolate states and bands for a neighborhood of the point  $\Gamma(0, 0)$  of the Brillouin zone. This allows to build up bands for any directions of the Dirac cone. A more general case for  $k_x \neq k_y \neq 0$  will be addressed in the third section, in which we consider the complete Hamiltonian of the problem, confirming surface states, as well as finding also those of bulk. Finally in the fourth section we will study the strong confinement effects in the case of a slab along the  $z$  direction.

## 2.1 Electronic Model for $Bi_2Se_3$

Three-dimensional topological insulator  $Bi_2Se_3$  has robust and simple surface states constituting a single Dirac cone at the  $\Gamma$  point. It has a rhombohedral crystal structure with five atoms in one unit cell. In detail, it has a layered structure with a triangle lattice within one layer (of constant lattice of about  $a = 5\text{\AA}$ ). It has a trigonal axis (threefold rotation symmetry), defined as the z-axis, a binary axis (twofold rotation symmetry), defined as the x-axis, and a bisectrix axis (in the reflection plane), defined as the y-axis. The material consists of five-atom layers arranged along the z-direction, known as quintuple layers (QL) (high around  $1nm$ ). Each quintuple layer consists of five atoms with two equivalent  $Se$  atoms (denoted as  $Se1$  and  $Se1'$ ), two equivalent  $Bi$  atoms (denoted as  $Bi1$  and  $Bi1'$ ), and a third  $Se$  atom (denoted as  $Se2$ , see Fig.(2.1)). To get a better understanding of the inversion of the band structure and the parity exchange, as in Figure 2.1(a), consider the states near the Fermi surface mainly come from  $p$  orbitals of  $Bi$  ( $6s^2 6p^3$ ) and  $Se$  ( $4s^2 4p^4$ ). For the analysis of the problem only the  $p_z$  orbitals become relevant [52, 53]. The band gap between these two orbitals is controlled by the spin-orbit coupling. In fact, increasing this coupling, inversion of bands occurs.

The electrons near the Fermi surfaces mainly come from the  $p$  orbitals of  $Bi$  and  $Se$  atoms. According to the point group symmetry of the crystal lattice,  $p_z$  orbital splits from  $p_{x;y}$  orbitals. Near the Fermi surface the energy levels turn out to be the  $p_z$  orbital,  $|P1_z^+, \uparrow\rangle$ ,  $|P2_z^+, \uparrow\rangle$ ,  $|P1_z^+, \downarrow\rangle$  and  $|P2_z^+, \downarrow\rangle$ , where  $\pm$  stand for the parity of the corresponding states while the symbols  $\downarrow\uparrow$  represent the electron spin. To describe the states around the point  $\Gamma$ , a basis of  $p_z$  to construct the low energy effective Hamiltonian can be used. The effective Hamiltonian based on the Dirac equation [54] :

$$H = \epsilon_0 \mathbb{I}_4 + M \mathbb{I}_2 \otimes \tau_z - iC_1 \sigma_z \otimes \tau_x \partial_z + \\ -iC_2 [\sigma_x \otimes \tau_x (\partial_x + iA_x) + \sigma_y \otimes \tau_x (\partial_y + iA_y)]. \quad (2.1)$$

The important symmetries of the system are the time reversal  $\mathcal{T}$ , the

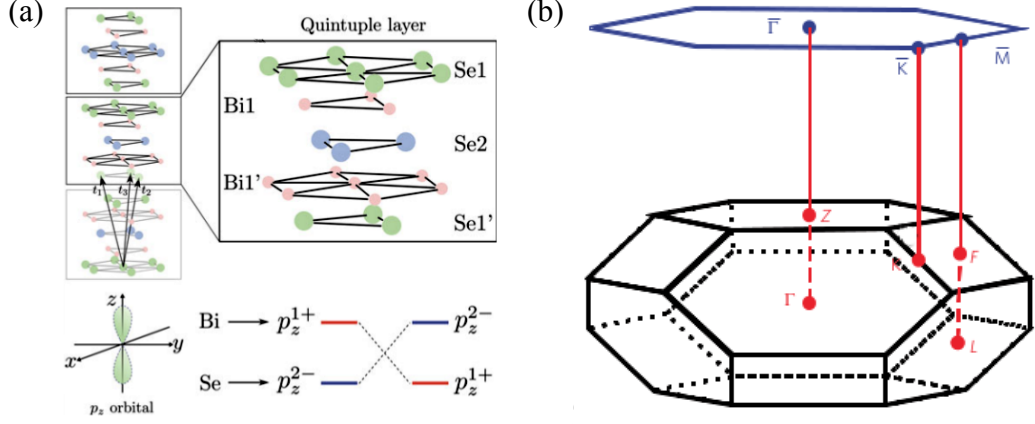


Figure 2.1: (a) Crystal structure of  $Bi_2Se_3$  with three primitive vectors denoted as  $t_{1;2;3}$ . Note the elementary cell formed by three quintuple layer. Electronic orbitals  $p_z$ , the band inversion of the  $p_z^+$  orbitals of  $Bi$  and the  $p_z^-$  orbitals of  $Se$  due to the spin-orbit coupling. (b) The four inequivalent time-reversal-invariant points in Brillouine zone are  $\Gamma$ ,  $L$ ,  $F$  and  $Z$ . The blue hexagon shows the 2D Brillouin zone of the projected  $(1, 1, 1)$  surface, in which the high-symmetry  $k$  points,  $K$  and  $M$  are labelled.

rotation symmetry  $\mathcal{C}_3$  along  $z$  direction and inversion symmetry  $\mathcal{I}$ . The representation of the cited symmetry operators is given by  $\mathcal{T} = \mathcal{K} \cdot i\sigma^y \otimes \mathbb{I}_2$ ,  $\mathcal{C}_3 = \exp(i(\pi/3)\sigma^z \otimes \mathbb{I}_2)$ , and  $\mathcal{I} = \mathbb{I}_2 \otimes \tau_z$  where  $\mathcal{K}$  is the complex conjugation operator,  $\sigma^{x,y,z}$  and  $\tau_{x,y,z}$  denote the Pauli matrices in the spin and orbital space, respectively. In equation 2.1, the operator  $M = M_0 + M_2(\partial_x^2 + \partial_y^2 + \partial_z^2)$  depends on the parameter  $M_0$  controlling the bulk gap, and the parameter  $M_2$  giving a mass correction.  $\partial_x$  and  $\partial_y$  are the partial derivatives along  $x$  and  $y$ , respectively. The symbol  $\otimes$  represents the tensor product linking spin and orbital degrees of freedom. Finally, the parameters  $C_1$  and  $C_2$  control the inter-orbital and inter-spin couplings, while  $A_x$  and  $A_y$  are the  $x$  and  $y$  component, respectively, of the vector potential  $\mathbf{A}$  corresponding to an homogeneous magnetic field  $\mathbf{B}$  parallel to the axis of the cylinder. In this section to simplify the accounts we consider the particle-hole symmetry placing the term  $\epsilon_0 = 0$ .

For the three dimensional bulk with zero magnetic field, one gets the following  $H_{3D}$  matrix at the momentum  $\mathbf{k} = (k_x, k_y, k_z)$ :

$$H_{3D}(\mathbf{k}) = \begin{bmatrix} M & C_1 k_z & 0 & C_2 k_- \\ C_1 k_z & -M & C_2 k_- & 0 \\ 0 & C_2 k_+ & M & -C_1 k_z \\ C_2 k_+ & 0 & -C_1 k_z & -M \end{bmatrix}, \quad (2.2)$$

with  $k_+ = k_x + ik_y$  and  $k_- = k_x - ik_y$ . The topological nature of the material is determined by the relative sign between  $M_0$  and  $M_2$ . If the ratio between the two parameters is positive, then the insulating state is  $\mathbb{Z}_2$  with topological index  $\nu_0 = 0$  i.e. the material is a trivial insulator. Otherwise, one gets  $\nu_0 = 1$  and the material is a strong topological insulator. The strong topological insulator has surface states protected by strong and weak disorder unlike the weak topological insulator that in presence of disorder pushes the metal surface state into the bulk, opening a gap in the Dirac cone [55].

## 2.2 Effective model for surface states at

$$\mathbf{k}_x = \mathbf{k}_y = \mathbf{0}$$

Consider the problem on an plane  $xy$  at  $z = 0$ . In the Hamiltonian 2.1 we consider translational invariance along  $x$  and  $y$  direction, so the wave vectors  $k_x$  and  $k_y$  are good quantum numbers, while we confine along  $z$  direction. Thus the Hamiltonian in 2.1 depends still on derivative in  $z$  and remembering that is a matrix  $4 \times 4$ , we find the states for a specific case  $k_x = k_y = 0$ . The Schrodinger equation becomes

$$H(z) |\psi\rangle = E |\psi\rangle, \quad (2.3)$$

where  $H(z) = (M_0 + M_2 \partial_z^2) \mathbb{I}_2 \otimes \tau_z - iC_1 \sigma_z \otimes \tau_x \partial_z$ . It is possible to observe in the matrix 2.3 that the first and second and the third and fourth rows are

decoupled, therefore we can take two trial wave functions:

$$|\psi_1\rangle = \begin{pmatrix} a_1 \\ b_1 \\ 0 \\ 0 \end{pmatrix} e^{\lambda_1 z} \quad |\psi_2\rangle = \begin{pmatrix} 0 \\ 0 \\ a_2 \\ b_2 \end{pmatrix} e^{\lambda_2 z}. \quad (2.4)$$

The functions in eq.(2.4) are factorizable in the  $z$  variable, therefore:

$$\begin{pmatrix} M_0 + M_2\lambda_1^2 & iC_1\lambda_1 \\ iC_1\lambda_1 & -M - M_2\lambda_1^2 \end{pmatrix} \begin{pmatrix} a_1 \\ b_1 \end{pmatrix} = E \begin{pmatrix} a_1 \\ b_1 \end{pmatrix}, \quad (2.5)$$

and

$$\begin{pmatrix} M_0 + M_2\lambda_2^2 & -iC_1\lambda_2 \\ -iC_1\lambda_2 & -M_0 - M_2\lambda_2^2 \end{pmatrix} \begin{pmatrix} a_2 \\ b_2 \end{pmatrix} = E \begin{pmatrix} a_2 \\ b_2 \end{pmatrix}, \quad (2.6)$$

We focus on the solution of the eq.(2.5). To have a nontrivial solution, the characteristic equation is:

$$\det \begin{pmatrix} M_0 + M_2\lambda^2 - E & iC_1\lambda \\ iC_1\lambda & -M_0 - M_2\lambda^2 - E \end{pmatrix} = 0. \quad (2.7)$$

From this equation, there are two solutions of the type:

$$\begin{aligned} \lambda_1 &= \frac{1}{2} \sqrt{\frac{C_1^2}{M_2^2}} + \sqrt{\frac{1}{4} \frac{C_1^2}{M_2^2} - \frac{M_0}{M_2}} \\ \lambda_2 &= \frac{1}{2} \sqrt{\frac{C_1^2}{M_2^2}} - \sqrt{\frac{1}{4} \frac{C_1^2}{M_2^2} - \frac{M_0}{M_2}} \end{aligned} \quad (2.8)$$

The  $\lambda_{1,2}$  are complex quantities such that  $\lambda_1^* = \lambda_2$ . The energy eigenvalue has been taken equal to  $E = -M_0/M_2$  in the case of  $k_x = k_y = 0$ . Here we assume this result that will be better understood when we will study the general case. The equation for the eigenstates requires that

$$\frac{a_1}{b_1} = \frac{iC_1\lambda_2}{M_2\lambda_2^2 + M_0}. \quad (2.9)$$

There is the adoption of the Dirichlet boundary conditions (semi-infinite), which require that the wave function for the surface states must vanish at  $z = 0$  and for  $z \rightarrow -\infty$ . The solutions will be linear combinations of states in the eq.(2.4):

$$|\Psi_1\rangle = \begin{pmatrix} a_1 \\ b_1 \\ 0 \\ 0 \end{pmatrix} (e^{\lambda_1 z} - e^{\lambda_2 z}), \quad (2.10)$$

together with eq.(2.6) which leads to  $a_2 = -a_1$  and  $b_2 = b_1$ , one still finds

$$|\Psi_2\rangle = \begin{pmatrix} 0 \\ 0 \\ -a_1 \\ b_1 \end{pmatrix} (e^{\lambda_1 z} - e^{\lambda_2 z}). \quad (2.11)$$

The eq.(2.10) and eq.(2.11) are a simplified version, having taken  $k_x = k_y = 0$ . In order to find the solution for  $k_x$  and  $k_y \neq 0$ , we may use the perturbation method by utilizing the two solutions of the same eq.(2.10) and eq.(2.11) as the basis to determine the effective Hamiltonian for small momentum. On the new basis, the effective Hamiltonian is projected out:

$$H_{eff} = \begin{pmatrix} \langle \Psi_1 | H | \Psi_1 \rangle & \langle \Psi_1 | H | \Psi_2 \rangle \\ \langle \Psi_2 | H | \Psi_1 \rangle & \langle \Psi_2 | H | \Psi_2 \rangle \end{pmatrix}. \quad (2.12)$$

The eq.(2.12) allows to derive a general Hamiltonian where  $H$  is the same in 2.1 and from this it is possible, once diagonalized, to derive a state of the surface in the case  $k_x \neq k_y \neq 0$ :

$$H_{eff} = C_{eff}(\vec{p} \times \vec{\sigma})_z, \quad (2.13)$$

where  $C_{eff} = -iC_2(a_1^*b_1 - a_1b_1^*)$ . Note that the effective Hamiltonian is only valid for a small  $k$ . From eq.(2.9) one gets:

$$|a_1|^2 = \frac{-iC_1\lambda_1}{M_2(\lambda_1^2 + \frac{M_0}{M_2})} \frac{-iC_1\lambda_2}{M_2(\lambda_2^2 + \frac{M_0}{M_2})} |b_1|^2. \quad (2.14)$$

Developing eq.(2.14) and taking into account the expressions in eq.(2.8), one finds the relationship between the two square modules given by  $|a_1|^2/|b_1|^2 = 1$ . One can estimate the value of  $|b_1|^2 = |a_1|^2 = 1/2$ . If the expression in eq.(2.13) gathers  $|b_1|^2$ , the part independent of the momentum is obtained:

$$C_{eff} = -\frac{i}{2} \left( \frac{a_1^*}{b_1^*} - \frac{a_1}{b_1} \right) C_2. \quad (2.15)$$

Finally, from eq.(2.15) combined with the eq.(2.9), one gets

$$C_{eff} = \text{sgn}(M_2)C_2. \quad (2.16)$$

So one gets the off-diagonal terms of the Hamiltonian, which are of the type  $\vec{q} \cdot \vec{\sigma}$ , with  $\vec{q} = (-k_y, k_x)$ , which turns out to be  $\vec{q} \perp \vec{k}$ . Of course,  $\vec{\sigma}$  is parallel to the vector  $\vec{q}$ , hence it is perpendicular to the vector  $\vec{k}$ . Therefore the lock-in relation between the momentum and spin is obtained [54]. It is possible to find in the direction of the spin, thanks to a diagonalization of eq.(2.13), a basis of the spin eigenstates which prove to be also perpendicular to the direction of the moment. In fact we can find the eigenvalues and eigenvectors of the effective Hamiltonian in 2.13 for particular values of  $k_x$  and  $k_y$ , finding that they are those of spin. For example, if we consider  $k_x = 0$  and  $k_y \neq 0$  then the diagonalization of 2.13 provides eigenstates of spin  $\sigma_x$  with the two possible eigenvalues associated. Therefore, this confirms that the eigenstate has the same spin direction, so that it is also perpendicular to  $\vec{k}$ . In polar coordinates, the vector  $\vec{q}$  is given by  $|k_{||}|(-\sin\phi, \cos\phi)$ , where  $\phi = \text{arccot}(k_y/k_x)$  is the angle that  $\vec{q}$  forms with the main axis,  $|k_{||}| = \sqrt{k_x^2 + k_y^2}$ , and the matrix obtained from  $\vec{q} \cdot \vec{\sigma}$  is:

$$\begin{pmatrix} 0 & -ie^{-i\phi} \\ ie^{i\phi} & 0 \end{pmatrix} \quad (2.17)$$

We proceed to diagonalize the eq.(2.17) that provides eigenvalues  $E = \pm|k_{||}|$  and eigenstates equal to:

$$\Psi_{\pm} = \begin{pmatrix} \pm e^{-i\phi} \\ i \end{pmatrix}. \quad (2.18)$$

We found, in this first approximation with a perturbation theory, that surface states are equal to the present form in eq.(2.16) and associates a energy linearly dependent to  $|k_{\parallel}|$ . The fact that it is a bi-spinor suffers from the fact that we started from an initial problem with two separable components, using only after the complete Hamiltonian evaluated, however, on two bi-spinors. The Berry phase, which is acquired by a state upon being transported around a loop in the momentum space, can be evaluated exactly:

$$\gamma = \oint d\phi \langle \Psi_{\pm} | i \frac{\partial}{\partial \phi} | \Psi_{\pm} \rangle = \pi. \quad (2.19)$$

The Berry phase plays an essential role in transport properties of the surface states, such as weak anti-localization.

In conclusion, the features found above confirm the experimental results, for a topological insulator with a single Dirac cone, an approximate theory leads to a linear dispersion near the point  $\Gamma$  of the energy bands and surface states of the form of eq.(2.18) protected by the topology of bulk.

## 2.3 Effective model for surface states at

$$\mathbf{k}_x \neq \mathbf{k}_y \neq 0$$

Now a description of the more general case is pursued. We consider the complete Hamiltonian in 2.1 that do not decouples the components as in 2.5 and 2.6. The procedure is similar to that of the case  $k_{\parallel} = 0$ , only a little more complicated from the analytical point of view. Indeed, thanks to a trivial trial state, one can solve the secular equation as before, but this time finding four roots. This then leads to eight independent solutions, two by two degenerate, which, by imposing the boundary conditions, lead to surface states. Most important is that, with this description, one come to an analytical form of the bands of energy for the surface states. The model provides a description always around the point  $\Gamma$  [56].

Therefore, the Hamiltonian matrix considered is that of eq.(2.1), in a more

general case, in particular we don't want to consider the hole-particle symmetry, so we redefine the Hamiltonian as follows:

$$H(\vec{k}) = \epsilon_0(\vec{k})I_{4 \times 4} + \begin{pmatrix} \mathcal{M}(\vec{k}) & -iC_1\partial_z & 0 & C_2k_- \\ -iC_1\partial_z & -\mathcal{M}(\vec{k}) & C_2k_- & 0 \\ 0 & C_2k_+ & \mathcal{M}(\vec{k}) & iC_1\partial_z \\ C_2k_+ & 0 & iC_1\partial_z & -\mathcal{M}(\vec{k}) \end{pmatrix}, \quad (2.20)$$

where  $k_{\pm} = k_x \pm ik_y$ ,  $\epsilon_0 = C - D_1\partial_z^2 + D_2k^2$ ,  $\mathcal{M}(\vec{k}) = M_0 + B_1\partial_z^2 - B_2k^2$ , and  $k^2 = k_x^2 + k_y^2$ . It is easy to find the connection between the coefficients in the eq.(2.20) and those present in the description above (eq.(2.1)).

From eq.(2.20) one can find both bulk and surface states, in the second case  $k_z$  it is not a good quantum number and therefore we take a four-component trial solution

$$\psi = \psi_{\lambda}e^{\lambda z} \quad (2.21)$$

into the Schrödinger equation ( $E$  is the eigenvalue of energy):

$$H(-i\partial_z, k)\psi = E\psi, \quad (2.22)$$

where  $k = k_{\parallel}$ . The secular equation leads to four solutions of  $\lambda(E)$ , denoted as  $\pm\lambda_{1,2}$ . Defining

$$\begin{aligned} F &= C_1^2 + D_+(E - L_1) + D_-(E - L_2), \\ R &= F^2 - 4D_+D_-[(E - L_1)(E - L_2) - a_2k_+k_-], \\ D_{\pm} &= D_1 \pm B_1, \\ L_1 &= C + M_0 + (D_2 - B_2)k, \\ L_2 &= C - M_0 + (D_2 + B_2)k \end{aligned}, \quad (2.23)$$

then the roots will be:

$$\lambda_{1,2} = \pm \sqrt{-\frac{F}{2D_+D_-} \pm \frac{\sqrt{R}}{2D_+D_-}}. \quad (2.24)$$

The eq.(2.24) is very similar to eq.(2.8). The expression concerning the general case is analytically more complicated. From the eigenvalue problem, four equations are obtained from eq.(2.21) leading, for each  $\lambda$ , to two

eigenfunctions. The solutions  $\psi_\lambda$ , factorizable for the part dependent on  $z$ , are

$$\psi_{\alpha\beta 1} = \begin{pmatrix} D_+\lambda_\alpha^2 - L_2 + E \\ -iC_1(\beta\lambda_\alpha) \\ 0 \\ C_2k_+ \end{pmatrix}, \quad (2.25)$$

$$\psi_{\alpha\beta 1} = \begin{pmatrix} C_2k_- \\ 0 \\ iC_1(\beta\lambda_\alpha) \\ D_-\lambda_\alpha^2 - L_1 + E \end{pmatrix}, \quad (2.26)$$

where  $\alpha = 1, 2$  and  $\beta = \pm$ . The general solution should be a linear combination of these eight functions:

$$\psi = \sum_{\alpha=1,2} \sum_{\beta=\pm} \sum_{\gamma=1,2} C_{\alpha\beta\gamma} \Psi_{\alpha\beta\gamma} e^{\beta\lambda_\alpha z}. \quad (2.27)$$

The coefficients  $C_{\alpha\beta\gamma}$  are determined by the choice of boundary condition that, as for the previous section, will be of the semi-infinite. You still want to study the case in which:

$$\psi(0) = 0 \quad \psi(+\infty) = 0. \quad (2.28)$$

The eq.(2.28) (for the case  $+\infty$ ) requires that in the eq.(2.27) the coefficient  $\beta$  is locked to be negative and that the real part of  $\lambda_\alpha$  be positive. For this reason, the number of equations passes from eight to four. Applying the boundary conditions, the system in the eq.(2.27) evaluated at the point  $z = 0$  provides no-trivial solutions and determining the coefficients  $C_{\alpha\beta\gamma}$ , one gets:

$$(\lambda_1 + \lambda_2)^2 = \frac{C_1^2}{D_+D_-}. \quad (2.29)$$

Substituting in eq.(2.29) the relations present in eq.(2.24), one gets

$$\begin{aligned} 2B_1^2E^2 - 4[(B_1D_2 - B_2D_1)k^2 + B_1C + D_1M_0]B_1E + \\ + [(B_1D_2 - D_1B_2)k^2 + D_1M_0 + B_1C]^2 + 2(D_1^2 - B_1^2)C_2^2k^2 = 0. \end{aligned} \quad (2.30)$$

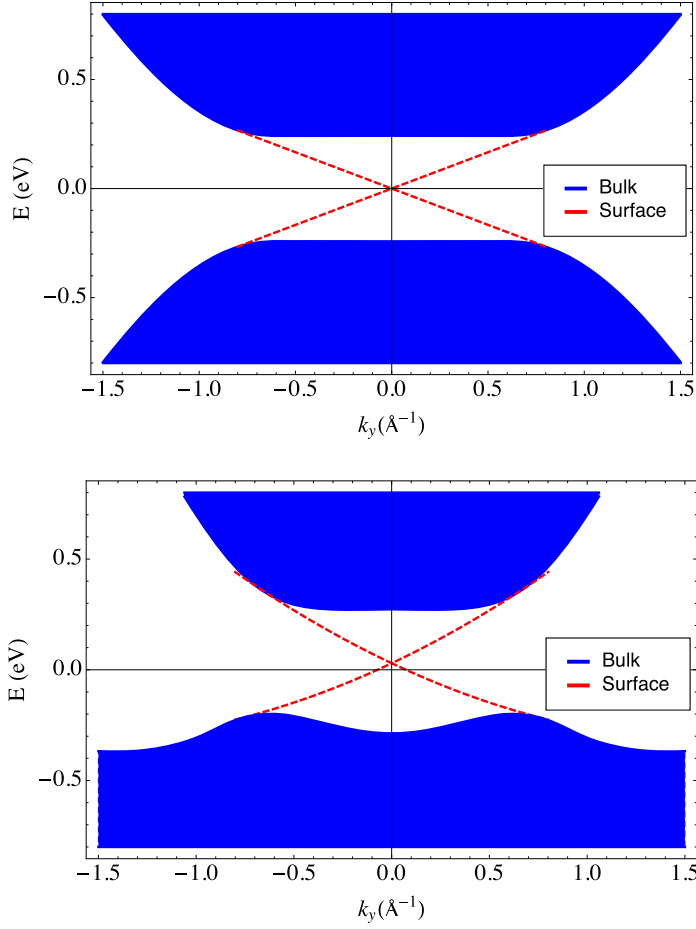


Figure 2.2: The Energy spectrum  $E(k_x = 0, k_y)$  in eV ( $k_y$  (in unit of  $\text{\AA}^{-1}$ ). The projected bulk energies are indicated by the blue areas, the surface energies due to the confinement along  $z$  direction by red dashed lines. Top panel: energies with the choice of parameters with hole-particle symmetry ( $C = D_1 = D_2 = 0$ ,  $M_0 = -0.28 \text{ eV}$ ,  $B_1 = B_2 = 40.00 \text{ eV}\text{\AA}^2$  and  $C_1 = C_2 = 3.33 \text{ eV}\text{\AA}$ ). Bottom panel: energies with the fit parameters taken from the *ab initio* calculations in [57].

Solving the eq.(2.29), finally one gets an analytical form of energy bands for surface state:

$$E_{\pm} = C + \frac{D_1 M_0}{B_1} \pm C_2 \sqrt{1 - \frac{D_1^2}{B_1^2} k + (D_2 - \frac{B_2 D_1}{B_1}) k^2}. \quad (2.31)$$

It is possible to obtain in this way also the dispersion of bulk bands. In this regard, then, one solves the secular equation eq.(2.20) for bulk states, where  $k_z$  returns to be a good quantum number; in place of  $\lambda_\alpha$ , there will be  $k_z$ . This time, similarly to the case of bulk bands, a bi-quadratic equation is obtained:

$$[E^2 - (\mathcal{M}^2(k) + C_1^2 k_z^2 + C_2^2 k^2)]^2 = 0. \quad (2.32)$$

Thus, taking into account the diagonal term, the bulk of the energy expression becomes:

$$E_{bulk} = \epsilon_0 \pm \sqrt{\mathcal{M}^2(k) + C_1^2 k_z^2 + C_2^2 k^2}. \quad (2.33)$$

From eq.(2.31) and eq.(2.33), one is able to plot along a particular direction in 3D B.z. and understand how the bands are made for surface and bulk states, as shown in Figure 2.1, for particular values of the parameters of the Hamiltonian. Note the linear dispersion around the point  $\Gamma$  represents the cone section of Dirac, very similar to experiments seen in the previous chapter. In the Figure 2.2 the two choices of parameters give results similar. To simplify from this point on, we shall consider the set of simplified parameters of the top panel of Figure 2.2. So our choice of Hamiltonian parameters will be:  $C = D_1 = D_2 = 0$ ,  $M_0 = -0.28 \text{ eV}$ ,  $B_1 = B_2 = 40.00 \text{ eV \AA}^2$  and  $C_1 = C_2 = 3.33 \text{ eV \AA}$ .

## 2.4 Confinement effects: Slab

All the results discussed in the previous sections have been obtained in the thermodynamic limit, in particular along z direction. But what happens if we get out of this condition?

Limiting the number of planes along the z direction, it is expected that, at some point, the surface states created at the two interfaces with the vacuum begin to interfere with each other. In the slab configuration, when the two interfaces with the vacuum are sufficiently far from each other, the structure of the Dirac cone is preserved. Close to the  $\Gamma$  point, due to the spin-momentum

locking at the surface, a rotation of the spin occurs when one considers different momenta in the Brillouin zone. The spin-momentum locking can be described by a Rashba model similar to that used for the description of spin-orbit couplings in two dimensional electron gases [58, 59]. However, if the thickness of the material is very reduced in the direction orthogonal to the interface, the electronic states of the two surfaces tend to hybridize through the thin bulk, hampering the formation of the Dirac cone [52]. As a result, at the  $\Gamma$  point, there is the opening of a gap whose size is typically smaller than that of the bulk gap. For convenience and to further simplify the math, we consider the same Hamiltonian present in 2.1, with the order of the inverted basis, namely  $|P1_z^+, \uparrow\rangle, |P1_z^+, \downarrow\rangle, |P2_z^+, \uparrow\rangle$ , and  $|P2_z^+, \downarrow\rangle$ . Furthermore, we neglect quadratic terms as a further simplification, given that we are interested in understanding the trend of the opening of the gap at the point  $\Gamma$  of the B.z., where the energy dispersion are linear. Thus the Hamiltonian takes the form:

$$H = -M_0(z)\tau_z \otimes \mathbb{I} - iC_1\tau_y \otimes \mathbb{I}\partial_z + C_2\tau_x \otimes (\sigma_x k_y - \sigma_y k_x), \quad (2.34)$$

in which we break the translational invariance along  $z$  direction and consider hole-particle symmetry. It is observed that the 2.34 is a linear Dirac equation for which is not possible to impose the boundary conditions present in the 2.28. For this reason, we have made the choice to take a parameter  $M_0(z)$  which depends on  $z$  variables. Thus, if we consider a slab confined along the  $z$  direction of initial and final plans respectively to  $z = -d$  and  $z = 0$ , we set

$$\begin{cases} M_0 & -d < z < 0 \\ -M'_0 & z < -d \wedge z > 0. \end{cases} \quad (2.35)$$

where  $M_0$  is defined within the material and  $M'_0$  outside. To simulate the boundary condition of infinite barrier, we consider the case in which  $M'_0 \rightarrow \infty$ . At this point, by solving the secular equation as in 2.22, we build

inside the slab the four eigenfunctions at  $\vec{k}_{\parallel} = 0$ :

$$\begin{aligned}
\psi_1(z) &= e^{\lambda z} \left( 1, 0, -\frac{E_0 + M_0}{\sqrt{M_0^2 - E_0^2}}, 0 \right), \\
\psi_2(z) &= e^{\lambda z} \left( 0, 1, 0, -\frac{E_0 + M_0}{\sqrt{M_0^2 - E_0^2}} \right), \\
\psi_3(z) &= e^{-\lambda(z+d)} \left( 1, 0, \frac{E_0 + M_0}{\sqrt{M_0^2 - E_0^2}}, 0 \right), \\
\psi_4(z) &= e^{-\lambda(z+d)} \left( 0, 1, 0, \frac{E_0 + M_0}{\sqrt{M_0^2 - E_0^2}} \right),
\end{aligned} \tag{2.36}$$

where  $\lambda = \frac{\sqrt{M_0^2 - E_0^2}}{C_1}$  and  $E_0$  is the energy for  $\vec{k} = 0$ , also since we have considered the particle-hole symmetry. We care about the normalization once you find the total wave function of the slab in  $[-d, 0]$ . For the other two cases outside the slab similarly to the equation 2.36, we obtain respectively for  $[0, +\infty]$ :

$$\begin{aligned}
\psi_5(z) &= e^{-\lambda' z} \left( 1, 0, \frac{E_0 + M'_0}{\sqrt{M'_0{}^2 - E_0^2}}, 0 \right), \\
\psi_6(z) &= e^{-\lambda'(z+d)} \left( 0, 1, 0, \frac{E_0 + M'_0}{\sqrt{M'_0{}^2 - E_0^2}} \right),
\end{aligned} \tag{2.37}$$

with  $\lambda' = \frac{\sqrt{M'_0{}^2 - E_0^2}}{C_1}$ . Finally, for the case of  $[-\infty, -d]$  we have:

$$\begin{aligned}
\psi_7(z) &= e^{\lambda' z} \left( 1, 0, -\frac{E_0 + M'_0}{\sqrt{M'_0{}^2 - E_0^2}}, 0 \right), \\
\psi_8(z) &= e^{\lambda'(z+d)} \left( 0, 1, 0, -\frac{E_0 + M'_0}{\sqrt{M'_0{}^2 - E_0^2}} \right).
\end{aligned} \tag{2.38}$$

Now we solve the problem within and outside the slab, consider three functions, respectively, within the slab to  $-d < z < 0$  :

$$\phi_{int}(z) = c_1\psi_1(z) + c_2\psi_2(z) + c_3\psi_3(z) + c_4\psi_4(z), \tag{2.39}$$

for  $z < -d$ :

$$\phi_{1,ext}(z) = c_5\psi_5(z) + c_6\psi_6(z), \tag{2.40}$$

and finally for  $z > 0$ :

$$\phi_{2,ext}(z) = c_7\psi_7(z) + c_8\psi_8(z). \quad (2.41)$$

To find the coefficients in the relationships 2.39, 2.40 and 2.41, we have to impose the condition of continuity at the points  $z = -d$  and  $z = 0$ :

$$\begin{cases} \phi_{int}(-d) = \phi_{2,ext}(-d) \\ \phi_{int}(0) = \phi_{1,ext}(0) \end{cases} \quad (2.42)$$

The linear system has as unknowns the  $c_i$  coefficients and it is homogeneous. To obtain non-trivial solutions must impose the determinant of the coefficients equal to zero. The coefficient matrix is 8x8 which can be written in two 4x4 identical blocks. Before doing any work since we are interested in solving the problem of single slab, we do limit of  $M'_0 \rightarrow +\infty$  which leads to write the 4x4 blocks as follows:

$$R_{m' \rightarrow +\infty} = \begin{bmatrix} 1 & b & -1 & 0 \\ a & -ab & 1 & 0 \\ b & 1 & 0 & -1 \\ ab & -a & 0 & -1 \end{bmatrix} \quad (2.43)$$

where we remember  $a = -\frac{E_0 + M_0}{\sqrt{M_0^2 - E_0^2}}$  and  $b = e^{-d\frac{\sqrt{M_0^2 - E_0^2}}{c_1}}$ . From the condition  $\det|R(\infty)| = 0$ , we find two relations:

$$a = \frac{-1 + b}{1 + b} \quad a = \frac{1 + b}{-1 + b}. \quad (2.44)$$

From the expression 2.44 is possible to derive the trend of the semi-gap  $E_0$ , where each one of the two equations provides a positive and negative  $E_0$ . For large distances  $d$ , it is possible to consider the energy  $E_0$  (the smallest positive energy at the point  $\Gamma$ ) such that  $E_0 \ll M_0$ , so we expand in series:

$$a = -\frac{E_0 + M_0}{\sqrt{M_0^2 - E_0^2}} \sim -\frac{1 + \frac{E_0}{M_0}}{1 - \left(\frac{E_0}{2M_0}\right)^2} \sim -\left(1 + \frac{E_0}{M_0}\right) \left(1 + \frac{E_0^2}{2M_0^2} + \dots\right), \quad (2.45)$$

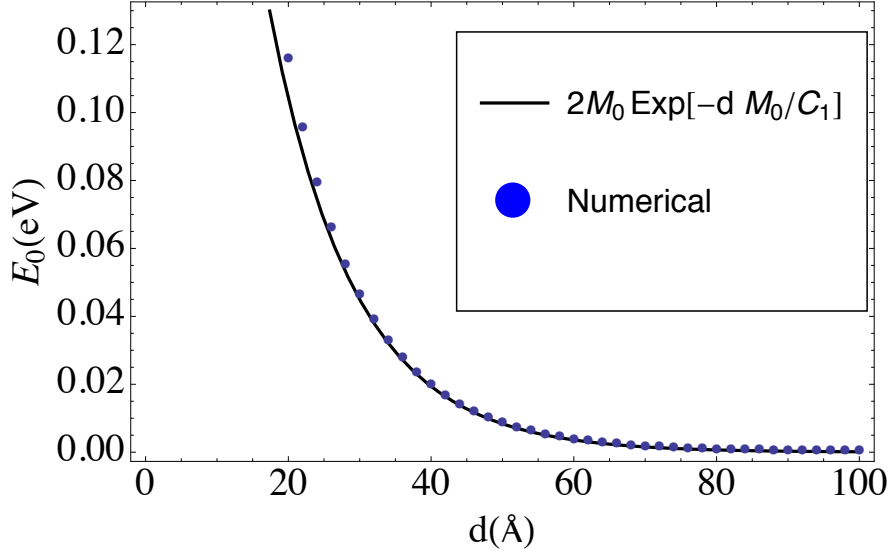


Figure 2.3: Trend of the semi-gap as a function of the thickness  $d$  of the slab. The points (blue) are the numerical solution of the expression in 2.44 while the solid line (black) is the solution found in 2.49. The choice of the parameters considered is given by  $M_0 = 0.28eV\text{\AA}$ ,  $C_1 = 3.33eV\text{\AA}$ .

and

$$b = e^{-d\frac{\sqrt{M_0^2 - E_0^2}}{C_1}} \sim e^{-\frac{d}{C_1}M_0\left[1 - \frac{1}{2}\left(\frac{E_0}{M_0}\right)^2\right]} \sim e^{-\frac{d}{C_1}M_0} \left[1 + \frac{dM_0}{2C_1} \left(\frac{E_0}{M_0}\right)^2 + \dots\right]. \quad (2.46)$$

So also this expression in 2.44 becomes:

$$\frac{1+b}{1-b} = \frac{1+b}{-1+b} \sim -(1+b)^2 \sim -(1+2b). \quad (2.47)$$

In this way, combining the equations 2.47 and 2.44, we get:

$$-\left[1 + \frac{E_0}{M_0} + \frac{1}{2} \left(\frac{E_0}{M_0}\right)^2 + \dots\right] = \left[1 + 2e^{\frac{d}{C_1}M_0} \left(1 + \frac{d}{2C_1} \frac{E_0^2}{M_0}\right)\right], \quad (2.48)$$

which solution leads to

$$E_0 = 2M_0 e^{-\frac{d}{C_1}M_0}. \quad (2.49)$$

The result of the opening of the gap in  $\Gamma$  point responsible for the loss of the Dirac cone is shown in Figure 2.3. Note that the cone is restored to a

thickness of about  $d = 80\text{\AA}$ , not far from the experimental results presented in Figure 1.7.

## Chapter 3

# Electronic states of topological insulator nano-wires

In this chapter we want to study the electronic properties of a TI nano-wires. In particular, we analyze the role that plays the Berry phase on the band structure of the surface states for different values of an external magnetic field and to vary the length and shape of the cross-section. In the case of cylindrical nano-wires, we resort also to an approximated analytical solution valid in the continuum limit. Actually, a simple approximated analytic calculation, exact only close to the asymptotic limit of infinite radius, has been proposed in the case of a full cylinder [68]. In this thesis, we improve the approximations used in the previous paper, reporting an analytical solution which is valid for large but finite radii of the cylindrical nano-wire. The effects of the Berry phase continue to be robust, but, for finite radii, the closure of the gap takes place for magnetic fields larger than those corresponding to half quantum flux. In fact, we find that the additional magnetic field decreases with increasing the nano-wire radius vanishing only in the limite of infinite radius. Concerning the numerical diagonalization, we use a grid with a variable mesh for the cross-section in order to accurately simulate a circle of fixed radius. For radii larger than  $100\text{\AA}$ , the numeric approach perfectly reproduces the analytical results. With decreasing the radius, the numerical

solutions show some deviations from the analytical results.

We numerically analyze the electronic states of a nano-wire with square and rectangular cross-sections considering not only different confining directions, but also different aspect ratios between the side lengths of the rectangle. In particular, in the case of a square cross-section, the electron density of the surface states exhibits peaks at the corners due to the boundary conditions and not to additional corner potentials as discussed in the literature [69]. In all the geometries, only for infinite area cross-sections, the closure of the gap in the presence of the magnetic field occurs for half quantum flux. With decreasing the cross-section area, the gap closes for magnetic fields larger than those corresponding to half quantum flux showing a dependence on the size and geometry of the nano-wire. Moreover, quite unexpectedly, for all the geometries, we find the presence of a minimum and maximum of the energy gap at the  $\Gamma$  point with varying the cross-section characteristic length in the range from 50 to 100Å. As a consequence, close to the minimum, the magnetic field for the gap closing gets significantly reduced. Wires with cross section lengths smaller than 100Å are at present difficult to realize experimentally [70], therefore, the analysis for those cross section lengths represents a theoretical prediction to be confirmed by experiments. In the case of a rectangular cross section with aspect ratio equal to 1/6, the minimum coincides nearly with zero energy. This implies that the gap can be closed at a finite length without any magnetic field. With decreasing the aspect ratio, close to the minimum of the gap, the system behaves decoupling the two sides with the shortest length along the perimeter, restoring in a certain sense the case of a single confinement in the direction orthogonal to these sides.

In the first section, an introduction to the experimental study and general electronic features for a TI nano-wire is presented.

In the second section, the analytical and numerical solutions for the electronic states of the cylindrical nano-wire are discussed.

In the third section, square/rectangular nano-wires are investigated.

### 3.1 Introduction

Starting from a theoretical model of low energy around the  $\Gamma$  point of the B.z., we obtained in the previous chapter the surface states and energies of the compound  $Bi_2Se_3$ . In particular, we have analyzed the confinement effects when we constrain the material along one direction in the case of a slab. When the thickness of the slab is such that the states of the surface interfere with each other, immediately opens a gap in the bulk of the gap. A different situation takes place when the TI is confined into two directions as in the case of a nano-wire. In a naive way, one can think that the surface states always communicate with each other favoring quantum interference effects. As a consequence, the opening of a small gap at the  $\Gamma$  point occurs even for large nano-wire cross-sections. In the nano-wire, the opening of the gap is ascribed to the role played by the Berry phase, the geometrical phase which characterizes the system relating the states on the cross-section perimeter with consequent real space spin-texture. Actually, the surface states not only are conductive, but they also show a particular spin rotation along the perimeter of the wire cross-section (as in Figure 3.1(a)).

Some of the mentioned properties have recently been reported in the experimental section of the first chapter of this thesis. In presence of a magnetic field Aharonov-Bohm oscillations have been detected showing that the transport is confined to the surface [60]. Furthermore, in presence of a weak magnetic field applied parallel to the axis of the nano-wire, as already discussed in the first chapter, experimental studies report peaks of the conductance at magnetic fields corresponding to fluxes close to half quantum flux ( $\hbar/2e$ ) [25]. The presence of this peak is explained by the fact that the effects of the Berry phase on the electronic spectrum are eliminated by the interference effects due to the magnetic field that is able to restore the Dirac cone as in Figure 3.1(b,c). It is worth noticing that, in some cases, the experimental value for the magnetic field able to close the Berry phase gap can also be 20% larger than that corresponding to half quantum flux [61].

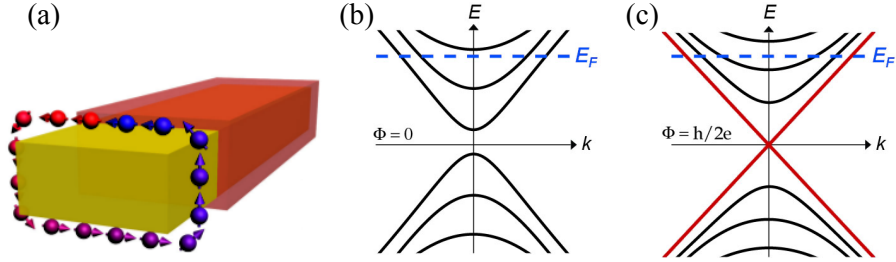


Figure 3.1: (a) A schematic diagram of the  $Bi_2Se_3$  core (yellow) / Se shell (orange) nano-wire and the topological surface electrons acquiring additional phase (represented by color change from red to blue) from the spin texture. In a TI nano-wire, electron spin is constrained in the tangent plane picking up a  $\pi$  Berry phase by a  $2\pi$  rotation of electrons along the perimeter, which (b) opens a gap in absence of magnetic flux ( $\Phi = 0$ ). (c) If we apply a magnetic field parallel to the axes of the wire the gap closes at half quantum flux ( $\Phi = \pm\hbar/2e$ ).

In a recent paper, three dimensional topological insulator nano-wires have been theoretically investigated considering only large square cross-sections in the absence of magnetic field [62]. Stimulated by these results, in this chapter, we study how the effects of the Berry phase in a  $Bi_2Se_3$  nano-wire open a gap at the Dirac cone for different geometries of the cross-section [63]. We point out that the starting point of our analysis is not given by a surface model [54, 64, 65], but by a three dimensional continuum bulk model considering not only circular [66, 67], but also square/rectangular cross sections for the nano-wires. Through an exact numerical diagonalization of the discretized model, we study the electronic states of the nano-wire with cylindrical, square and rectangular cross-sections since exact analytical solutions for the entire nano-wires are not available. We find that the gap energy and the related behavior in the presence of magnetic field are qualitatively similar for different cross-sections but they quantitatively depend on the size and the geometry of the nano-wire.

## 3.2 Cylindrical nano-wire: analytical and numerical solution

In the case of a wire with a circular cross-section and with translation invariance along  $z$  axis, one can exploit the symmetries of the geometry to obtain an approximate analytical solution. A solution of the problem, that is exact in the asymptotic limit of infinite radius, has been proposed in [68]. In fact, this solution is based on an adiabatic separation between the radial direction (“fast variable”) and the angular variable (“slow variable”). In this section, we improve that analytical approach introducing a better description of the radial component of the wave function. Moreover, we will test the analytical approximated solution by using exact diagonalization of a discretized model. Taking advantage of the cylindrical symmetry in the Hamiltonian present in 2.1, we can write  $\nabla = \partial_\rho + \partial_\phi/\rho + ik_z$  and  $\nabla^2 = \partial_\rho^2 + \partial_\rho/\rho + \partial_\phi^2/\rho^2 + k_z^2$ . Thus following the approach proposed in [68], it can be shown that the Hamiltonian 2.1 can be separated in a contribution that depends only on the derivative in  $\rho$ , namely  $H_\perp(\partial_\rho, \rho, \phi)$ , and in a part that depends only on  $\partial_\phi$ , namely  $H_\parallel(\partial_\phi, \rho, \phi, k)$ . In this way by type adiabatic approach, the approximate surface eigenfunctions can be found in the form:

$$\psi_m(k_z; \rho, \phi) = \left[ \frac{1}{\sqrt{2}} \mathbf{u}_1(\phi) + c^\pm(m, k_z) \mathbf{u}_2(\phi) \right] R(\rho) e^{im\phi}, \quad (3.1)$$

where polar coordinates  $(\rho, \phi)$  are used. In Eq. (3.1), we have introduced the two orthogonal four component vectors

$$\mathbf{u}_1(\phi) = \begin{bmatrix} 1 \\ i \\ e^{i\phi} \\ ie^{i\phi} \end{bmatrix}, \quad \mathbf{u}_2(\phi) = \begin{bmatrix} 1 \\ -i \\ -e^{i\phi} \\ ie^{i\phi} \end{bmatrix}, \quad (3.2)$$

where  $R(\rho)$  is the radial function which is solution of the following differential equation:

$$M_0 R(\rho) - M_2 \left( \frac{R'(\rho)}{r} + R''(\rho) \right) = -C_2 R'(\rho). \quad (3.3)$$

The relations in 3.2 and 3.3 coming out of resolution of the equation  $H_{\perp}(\partial_{\rho}, \rho, \phi)\mathbf{u}(\phi)R(\rho)e^{im\phi} = 0$ , where we made a expansion for  $E = 0$ . The expansion is justified because we want consider the particle-hole symmetry and we are interested to surface states around  $\Gamma$  point ( $k_x = k_y = 0$ ). If one defines  $a = M_2M_0/C_2^2$  and  $z = C_2\rho/M_2$ , the solution of (3.3) with boundary condition  $R(R_0) = 0$  ( $R_0$  is the cylinder radius) can be found in terms of combinations of hypergeometric functions and Laguerre polynomials [71–73]:

$$R(z) = e^{\frac{1}{2}(1-\sqrt{1+4a})z} \frac{H_y(a, R_0)L_a(a, z) - H_y(a, z)L_a(a, R_0)}{H_y(a, R_0)}, \quad (3.4)$$

where

$$H_y(a, z) = \text{HypergeometricU} \left[ -\frac{1 - \sqrt{1 + 4a}}{2\sqrt{1 + 4a}}, 1, \sqrt{1 + 4az} \right]$$

and

$$L_a(a, z) = \text{LaguerreL} \left[ \frac{1 - \sqrt{1 + 4a}}{2\sqrt{1 + 4a}}, \sqrt{1 + 4az} \right].$$

We note that the validity of this solution is extended to lower values of  $\rho$  compared to what done in [68] (valid for infinity radius) since in this work the term  $\partial_r/\rho$  of the Laplacian is taken into account. We find the coefficient  $c^{\pm}(m, k_z)$  in equation (3.1) and the eigenvalues by an effective two-dimensional Hamiltonian  $H_{2D}$ , obtained by calculating the matrix elements of  $H_{||}$  in terms of  $\mathbf{u}^{\pm}$ , namely  $\int d\rho\rho R^2(\rho) (\mathbf{u}^{\pm})^* H_{||} (\mathbf{u}^{\pm})$ . Thus we get:

$$c^{\pm}(m, k_z) = \pm \frac{1}{|E_{m,k_z}|} \left[ \left( \frac{M_2}{R_0^2} \left\langle \frac{R_0^2}{\rho^2} \right\rangle - \frac{C_2}{R_0} \left\langle \frac{R_0}{\rho} \right\rangle \right) \times \left( m + \frac{1}{2} - \frac{\Phi \langle \rho/R_0 \rangle}{\Phi_0 \langle R_0/\rho \rangle} \right) + iC_1k_z \right], \quad (3.5)$$

where the sign  $\pm$  corresponds to positive and negative eigenvalues given by:

$$E_{m,k_z} = \pm \left[ \left( \frac{M_2}{R_0^2} \left\langle \frac{R_0^2}{\rho^2} \right\rangle - \frac{C_2}{R_0} \left\langle \frac{R_0}{\rho} \right\rangle \right)^2 \times \left( m + \frac{1}{2} - \frac{\Phi \langle \rho/R_0 \rangle}{\Phi_0 \langle R_0/\rho \rangle} \right)^2 + C_1^2k_z^2 \right]^{1/2}. \quad (3.6)$$

In Eq.(3.5,3.6), the symbol  $\langle \cdot \rangle$  indicates the average value over the radial function  $R(\rho)$ ,  $\Phi$  is the flux threaded by the cross-section, and  $\Phi_0 = h/(2e)$

is the magnetic quantum flux. For simplify, we can call the ratio of magnetic fluxes  $r = \Phi/\Phi_0$ .

Notice that in Eq. (3.6) the parameter  $m$  labels the cylinder sub-bands whose spectrum can be also within the bulk gap. Moreover, in the absence of the flux  $\Phi$ , thanks to the factor  $1/2$  close to the parameter  $m$ , all the sub-bands are doubly degenerate in  $m$ . In fact, as reported in Eq.(3.6) for  $k_z = 0$ ,  $m = 0, -1$  (the lower sub-band) and  $r = 0$  (absence of the magnetic field), a gap is opened:

$$\Delta = \left| \left( \frac{M_2}{R_0^2} \left\langle \frac{R_0^2}{\rho^2} \right\rangle - \frac{C_2}{R_0} \left\langle \frac{R_0}{\rho} \right\rangle \right) \right|. \quad (3.7)$$

In the limit of a large radius  $R_0$ , the radial function  $R(\rho)$  for the surface states is essentially localized for values of  $\rho$  close to  $R_0$ . Thus, it is possible to consider the average values found in Eq.(3.6) and Eq.(3.7) equal to one, namely  $\langle \rho/R_0 \rangle = 1$ . Basically we can consider the radial function  $R(\rho)$  like a delta function that pike along the perimeter of the cross-section. In this case the gap in 3.7 becomes  $\Delta = C_2/R_0$ . Of course also the expression in Eq.(3.6), for large radii, becomes:

$$E_{m,k_z} = \pm \sqrt{\left( \frac{C_2}{R_0} \right)^2 \left( m + \frac{1}{2} - r \right)^2 + C_1^2 k_z^2} \quad (3.8)$$

where we have neglected the quadratic term  $M_2/R_0^2$ . The extra term  $1/2$  responsible for the nano-wire gap even for  $m = 0$  is a direct consequence of the Berry phase. As shown in Figure 3.2(b), for  $r = 0$ , above and below the semi-gap, the spectrum shows different sub-bands depending on the quantum number  $m$ . Furthermore for both positive and negative energies, the sub-bands are two-fold degenerate in  $m$ . For example, for  $r = 0$ , the couple  $m = 0, m = -1$  corresponds to the same energy. In the presence of a longitudinal magnetic field, the gap  $\Delta$  gets reduced and the two-fold degeneracy in  $m$  removed. Actually, interference terms due to magnetic field weaken the effects of the Berry phase. In particular, in the case of  $r = 0.5$  (half quantum flux), a total cancellation of the Berry phase effects takes place because of

the magnetic field even for a finite radius nano-wire. For  $r = 0.5$ , as reported both in Eq.(3.6) as in Eq.(3.8), the  $m = 0$  sub-band shows no more gap.

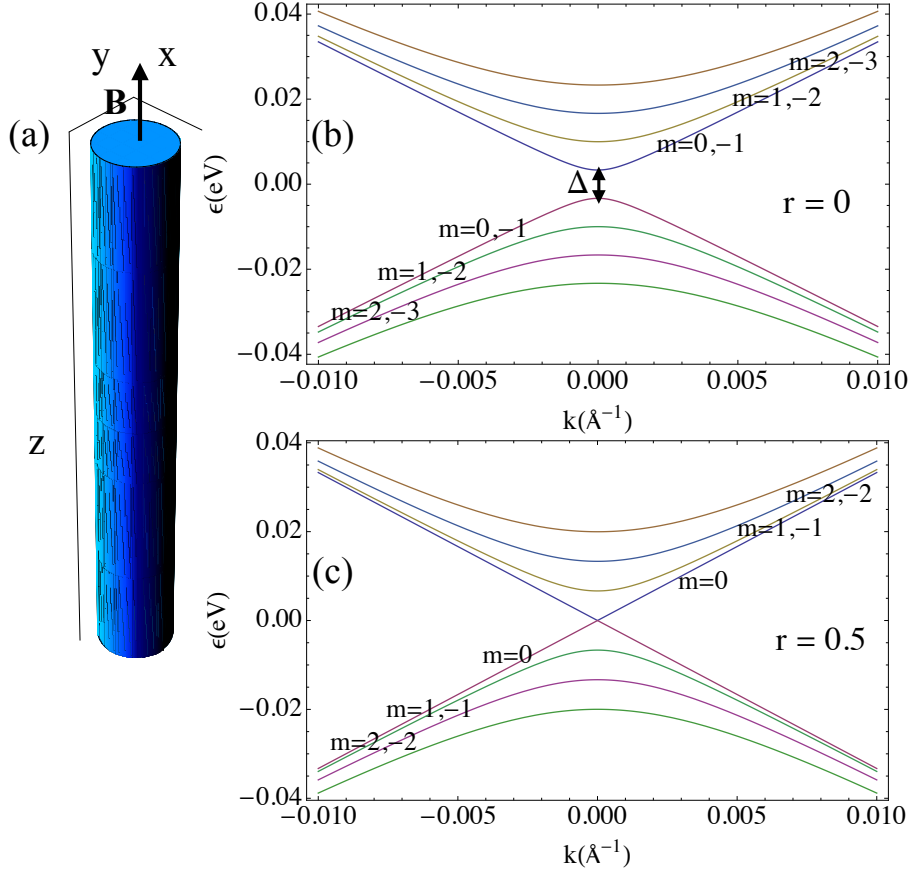


Figure 3.2: a) Sketch of the cylindrical wire with translational invariance along  $z$  direction in the presence of a magnetic field  $\mathbf{B}$  parallel to the  $z$  axis. b) The energy dispersion (in units of eV) as a function of momentum  $k$  (in units of  $\text{\AA}^{-1}$  along  $z$  direction) with the formation of a gap  $\Delta$  and the presence of sub-bands for  $r = 0$ . c) The energy dispersion (in units of eV) as a function of momentum  $k$  (in units of  $\text{\AA}^{-1}$  along  $z$  direction) with the closure of the gap for  $r = 0.5$  (half quantum flux). The surface state spectrum is obtained for a cylindrical wire with a radius  $R_0 = 100\text{\AA}$ .

As shown in Figure 3.2(c), in the case of  $r = 0.5$ , a two-fold degeneracy is again restored even if it has a different character. For example, in contrast

with the case of  $r = 0$ , we have that  $m = 1$  and  $m = -1$  are degenerate for  $r = 0.5$ .

We saw in the first chapter experiments on the transport on nano-wires. In particular, in Figure 1.9, several features of the magneto-conductance are presented for different values of the chemical potential. Through the measures of magneto-conductance for different chemical potentials, the conductive character of the material was studied as a function of the magnetic flux.

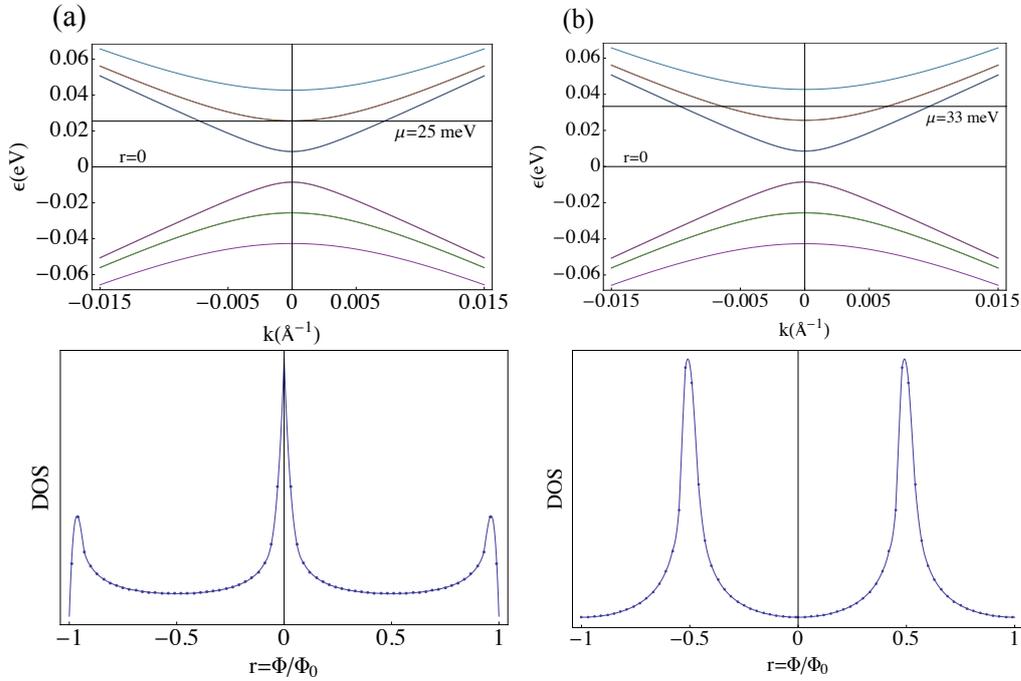


Figure 3.3: DOS calculated for two values of the chemical potential: a)  $\mu = 25 \text{ meV}$  and b)  $\mu = 33 \text{ meV}$  as a function of the magnetic flux for a cylindrical wire with a perimeter of the cross-section of about  $360 \text{ nm}$ . DOS peaks as a function of the magnetic field, are present at half quantum flux, as a sign of the closing of the gap at the  $\Gamma$  point of the B.z.

Depending on the value of the chemical potential, conductance peaks are observed at half quantum flux indicating the closure of the gap of the nano-

wire electronic states. With the surface states and energies that we have got above for a cylindrical wire, we can calculate the density of states (DOS). In the same way we can make this type of analysis through the study of DOS. A DOS calculation is very different from that of the conductance, but it can give an idea of how the sub-bands cross the Fermi level for different magnetic field values. In the work [25], fixing the chemical potential and varying the magnetic flux, the sub-bands change position in energy. In this way there is a variation of the electronic charge density (hence the DOS). Similarly to the behaviors shown in Figure 1.9, here we find the DOS to vary the magnetic field at fixed energy equal to the chemical potential. As reported in Figure 3.3, we find a trend qualitatively very similar to the experimental data for the conductance. In fact, we consider two chemical potential values, respectively  $\mu = 25 \text{ meV}$  and  $\mu = 33 \text{ meV}$  which lead to two different trends in the DOS as a function of the magnetic flux. In particular, sometimes there are peaks for integer multiples of quantum flux, and sometimes for half flux as a sign that the closure of the gap is occurred. To calculate these quantities, as indicated in Figure 3.3, we have chosen a perimeter comparable to that shown experimentally in [25], i.e.  $L = 360 \text{ nm}$ . In this way, we can reconstruct qualitatively the trends the conductance peaks by tuning the chemical potential. These features found in DOS are a clear sign of the one-dimensional nature of the system.

We found in 3.4 and 3.6 the general relations for surface states and energies, valid for each radius value. When the cylinder radius gets reduced, the solutions are no longer strictly confined on the surface and the electrons experience a finite probability to stay into the bulk. We, then, focus our study on how the gap changes as a function of the cylinder radius  $R_0$ . In Figure 3.4 we compare the gap computed with Eq.3.6, that calculated in Eq.3.8, and that obtained numerically by using exact diagonalization of the 2.1, as shown in Appendix B.

The three approaches coincide at large values of  $R_0$  confirming the asymp-

otic validity of the approximated analytical solution, but they exhibit significant differences at small  $R_0$ . However, even if quantitatively different in this regime, both our analytical solution in Eq.3.6 and the numerical one show a minimum-maximum structure for radii  $R_0$  ranging from  $40\text{\AA}$  to  $60\text{\AA}$ . We remark that this behavior is not present in previous analyses proposed in the literature [68] where only the limiting case of very large  $R_0$  has been investigated.

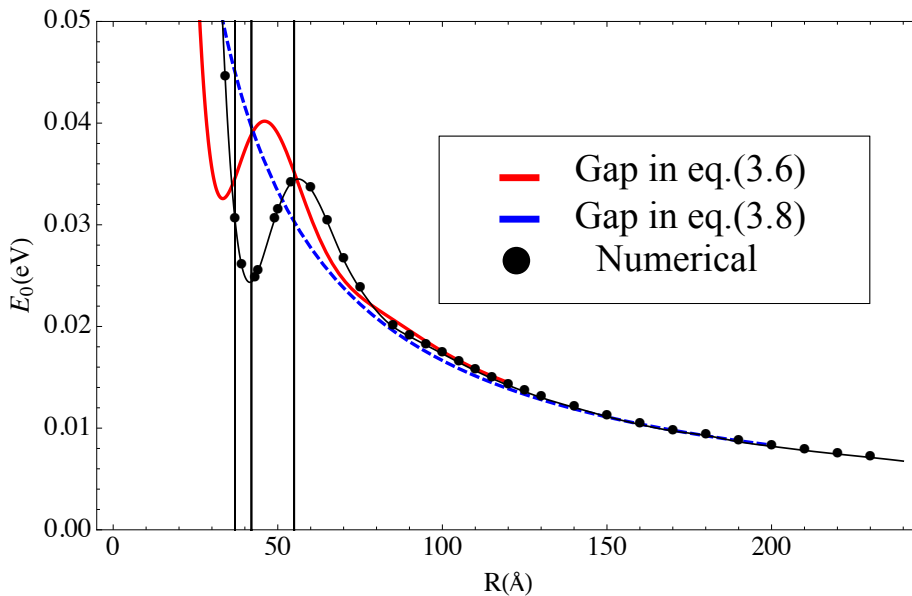


Figure 3.4: Gap energy (in units of eV) at  $k_z = 0$  and at  $r = 0$  as a function of the cylinder radius  $R_0$  (in units of  $\text{\AA}$ ) for three types of approaches: Eq.(3.6) of the approximate analytical solution valid for little radius (red line), energy derived from the solution for large radius in 3.8, and energy obtained from the numerically exact solution (black line with circles) from the Hamiltonian in 2.1.

This non monotonic behavior of the gap energy is somehow unexpected and is one of the results of this work. As mentioned above, a consequence of the Berry phase associated to the electronic state peaked at the cylinder surface and can be traced back to the term  $1/2$  present in Eq.3.6. However,

the gap value is controlled in Eq.(3.6) by the factor  $\left(\frac{M_2}{R_0^2}\langle\frac{R_0^2}{\rho^2}\rangle - \frac{C_2}{R_0}\langle\frac{R_0}{\rho}\rangle\right)^2$  that strongly depends on the radial wave-function through the average values of  $R_0/\rho$  and  $R_0^2/\rho^2$ . When  $R_0$  is reduced and the radial wave-function is not any longer strictly peaked at the cylinder surface, this factor provides an extra contribution to the gap. Naively one would have expected a simple monotonic increase of the gap since  $\langle R_0/\rho \rangle$  and  $\langle R_0^2/\rho^2 \rangle$  should increase when  $R_0$  decreases. Our calculation, instead, shows a non monotonic behavior that is confirmed by both the approximate analytical solution and the “numerically exact” solution. This behavior depends on how the “surface state” fills up the cylinder upon reducing the radius  $R_0$ . In order to clarify this point, in the upper panel of Fig.3.5, we plot the first sub-band wave-function probability density, obtained numerically, for the radii corresponding to the lowest analyzed value ( $37\text{\AA}$ , red line) and for the  $R_0$  values corresponding to the minimum ( $42\text{\AA}$ , blue line) and maximum ( $55\text{\AA}$ , orange line)(radii corresponding to vertical dotted lines in the bottom panel of Fig.3.4). We can see how, for the the radius corresponding to the maximum, the wave function extends to lower values of  $r$  compared to the case  $R = 42\text{\AA}$ , thereby entering the bulk more than the wave-function corresponding the minimum. One of the main features of the TI is related to the spin texture. We start from the analytic solution to understand the complex spin behavior of these nano-wires. For simplicity, we consider the case with  $k_z = 0$ . In the absence of magnetic field, as reported in Eq.(3.6), the two states for  $m = 0$  and  $m = -1$  correspond to the same energy and they can be written as

$$\begin{aligned}\psi_0^\pm(\rho, \phi) &= \left(\frac{1}{\sqrt{2}}\mathbf{u}_1(\phi) + c^\pm(0)\mathbf{u}_2(\phi)\right)R(\rho), \\ \psi_{-1}^\pm(\rho, \phi) &= \left(\frac{1}{\sqrt{2}}\mathbf{u}_1(\phi) + c^\pm(-1)\mathbf{u}_2(\phi)\right)e^{-i\phi}R(\rho),\end{aligned}\quad (3.9)$$

where  $c^\pm(m)$  is given in Eq. (3.5). Then, in the two dimensional subspace at fixed energy, we consider the matrix elements of the three spin components  $S_x = \sigma_x \otimes \tau_z$ ,  $S_y = \sigma_y \otimes \tau_z$ , and  $S_z = \sigma_z \otimes \mathbb{I}$  (written on the basis of the Hamiltonian in Eq.(2.1)). Considering only the lower positive sub-band, one

gets a  $2 \times 2$  matrix depending on  $(r, \phi)$  for each spin component:

$$\begin{pmatrix} \langle \psi_0^+(\rho, \phi) | S_i | \psi_0^+(\rho, \phi) \rangle & \langle \psi_0^+(\rho, \phi) | S_i | \psi_{-1}^+(\rho, \phi) \rangle \\ \langle \psi_{-1}^+(\rho, \phi) | S_i | \psi_0^+(\rho, \phi) \rangle & \langle \psi_{-1}^+(\rho, \phi) | S_i | \psi_{-1}^+(\rho, \phi) \rangle \end{pmatrix}, \quad (3.10)$$

with  $i = x, y, z$ .

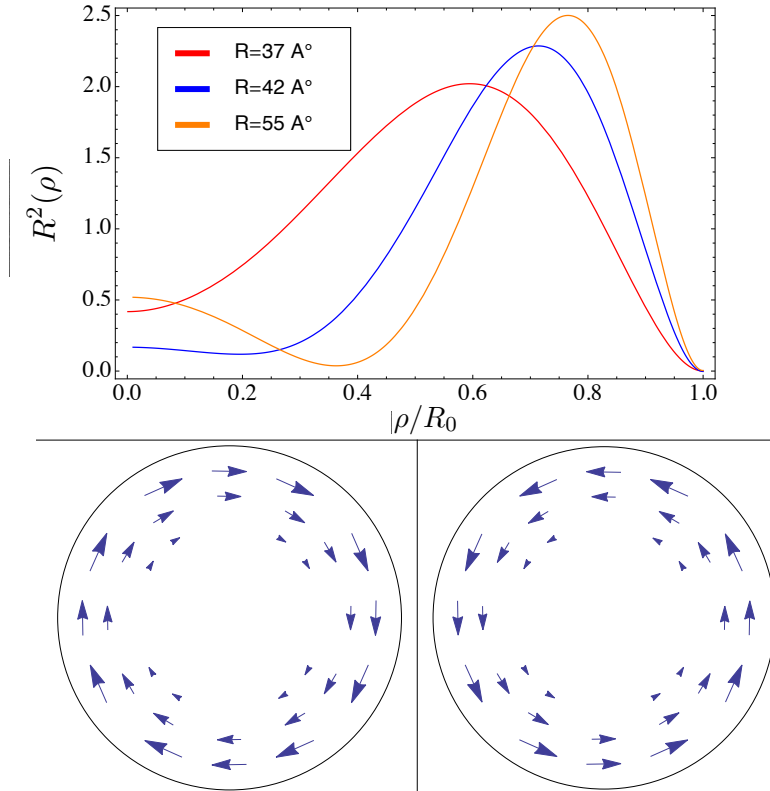


Figure 3.5: Top panel: Radial probability density of the first sub-band state at  $k_z = 0$  as a function of the radial coordinate for different cylinder radii identified by the dotted vertical lines in Fig.3.4. Bottom panel: spin-textures of the first sub-band state at  $k_z = 0$  obtained numerically for a cylinder of radius  $R = 65 \text{ \AA}$ . The modulus of the spin values is proportional to the length of the arrows.

For the two in-plane spin components ( $i = x, y$ ), only off-diagonal matrix elements are different from zero, while, for the component along  $z$ , all the matrix elements vanish. At this point, in order to find the expectation

values of spin components, we diagonalize the matrix (3.10) for each spin component at fixed  $(\rho, \phi)$  and we plot the eigenvalues. The eigenvalues for  $k_z = 0$  of the  $x$  component are:  $\lambda_x = \pm R(\rho) \cos(\phi)$ ; the two eigenvalues of the  $y$  component are:  $\lambda_y = \pm R(\rho) \sin(\phi)$ ; the eigenvalues of  $z$  component are clearly zero. Therefore, the spin eigenvalues are modulated by the radial part of the wave-function. For each spin component, the choice of the eigenvalue with varying  $(\rho, \phi)$  is made by ensuring that the phase of the corresponding spin eigenvector is continuous. Therefore, one gets two main spin textures: clockwise, corresponding to spin eigenvalues proportional to the vector  $R(\rho) (\cos(\phi), \sin(\phi), 0)$ ; counterclockwise, corresponding to spin eigenvalues proportional to the vector  $-R(\rho) (\cos(\phi), \sin(\phi), 0)$ . The procedure described above can be easily extended at finite values of  $k_z$ .

As discussed in Appendix B, at fixed energy and  $k_z$ , the method of the diagonalization of spin components can be also used starting from the eigenvectors obtained numerically. We report in the bottom panel of Fig.3.5 what we have obtained in the case of the numerical eigenvectors at  $k_z = 0$ . Indeed, the spin rotates around the surface both clockwise and counterclockwise. The agreement with the spin textures calculated analytically is good. In particular, the modulus of the spin values (proportional to the length of the arrow) directly follows the behavior radial probability density (some examples are in the top panel of Fig.3.5).

The application of a magnetic field along the translational invariant  $z$  axis of the wire introduces a magnetic flux  $\Phi$  which can change the gap value as can be seen from Eq.(3.6). There are many studies [25,64,74] about the effects of a magnetic field in TI nano-wires showing the formation of a one dimensional band for electrons on the cylinder surface. For very large cross sections, the specific values for which the gap closes correspond to semi integer quantum fluxes ( $\Phi_0/2, 3\Phi_0/2, \dots$ ) and they are distinguished from integer values found in ordinary Aharonov-Bohm effects. The analytical result provided by Eq. (3.6) and confirmed by the numerical calculations

shows that the gap closure depends on the size of the wire (see Fig.3.6). In fact, according to Eq.3.6, the gap closes at  $r = \frac{1}{2} \frac{\langle R_0/\rho \rangle}{\langle \rho/R_0 \rangle}$ , a value strongly depending on the radial wave-function and, therefore, on the radius  $R_0$  of the cylinder. The flux value closing the gap recovers  $\Phi_0/2$  only in the asymptotic regime ( $R_0 \mapsto \infty$ ). Indeed, only for large radii, the ratio  $\langle R_0/\rho \rangle / \langle \rho/R_0 \rangle \mapsto \frac{1}{2}$ .

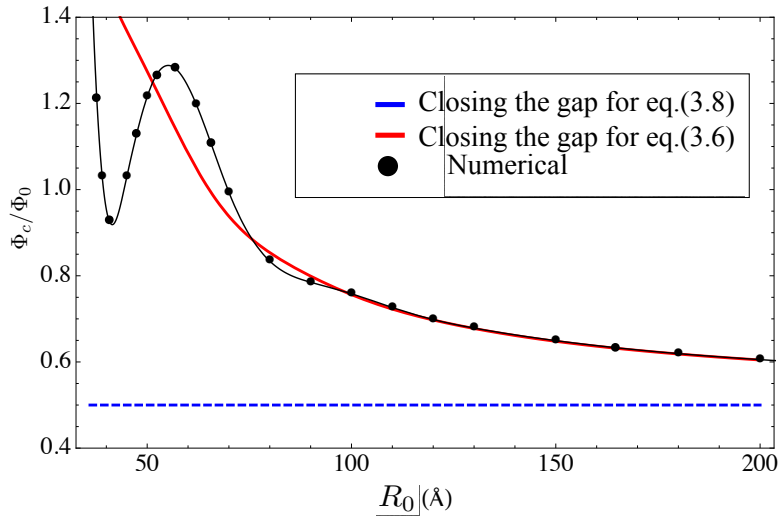


Figure 3.6: Magnetic flux  $\Phi_c$  (in units of quantum flux  $\Phi_0$ ) corresponding to the gap closure as a function of the cylinder radius  $R_0$  (in units of  $\text{Å}$ ). Curves derive from three approaches: analytical solution of Eq.3.8 (dash blue), analytical solution (red) in 3.6 and numerical method (black with solid circles).

The extrapolation of the fit of our analytical curve to infinity confirms this result. On the other hand, for small radii, the gap does not close at half quantum flux. This is, then, in contrast with what stated in the literature for the strictly two-dimensional case [65, 75] and what comes out including the magnetic field contribution in the approach of [68] (dashed line in Fig. 3.6). We point out that, for large radii, all the analytical and numerical approaches are completely consistent. However, as shown in Fig. 3.6, for small radii, the numerical data depend on the radius again in a non monotonic way differing from those derived from the proposed analytical solutions. More precisely,

the numerical results show the presence of a maximum and minimum in the magnetic flux corresponding to the gap closure. The presence of these stationary points is found for values of the radii equal to those found for the non monotonic behavior of energy gap when the magnetic field is not applied. The fully numerical approach looks very accurate since the gap closing magnetic flux is expected to be sensitive to the behavior of the gap in the absence of the magnetic field. We remark that the analytical solution proposed in this chapter does not predict the existence of the minimum and maximum for the magnetic flux.

### 3.3 Rectangular nano-wire

In this section, we discuss the case of a wire with a rectangular cross-section. The problem will be addressed only numerically, since, unlike the cylinder, an approximate analytical solution is not available for a generic cross-section and orientation (see Appendix B). To get the discrete model, we always start from Eq.(2.1), which is discretized with a fixed lattice parameter for any direction of the axes. All our results are obtained with a lattice constant  $a = 10\text{\AA}$ . However, we remark that, also for the smaller lattice parameter  $a = 5\text{\AA}$ , we find qualitatively similar results. Through a simple tight binding procedure, we analyze the surface states with their spin polarizations along the perimeter of the wire, for different confinements along the axes of the crystal lattice. This type of tight binding procedure does not consider the complex structure of the material since the triangular lattice is approximated by an effective square lattice [76]. A recent paper has proposed a more precise description of the surface states for thin wires focusing, however, on chemically distinct wire surfaces [77]. Moreover, as the cylinders, the rectangular wires are characterized by an oscillatory behavior of the gap for lengths between 50 and 100  $\text{\AA}$  due to the increased role of the bulk contribution in comparison with the surface contribution. Actually, being the surface contribution less important, we expect that the surface atomic details become less relevant at

those length scales. As for the cylinder, we analyze the surface states as a function of the wire size.

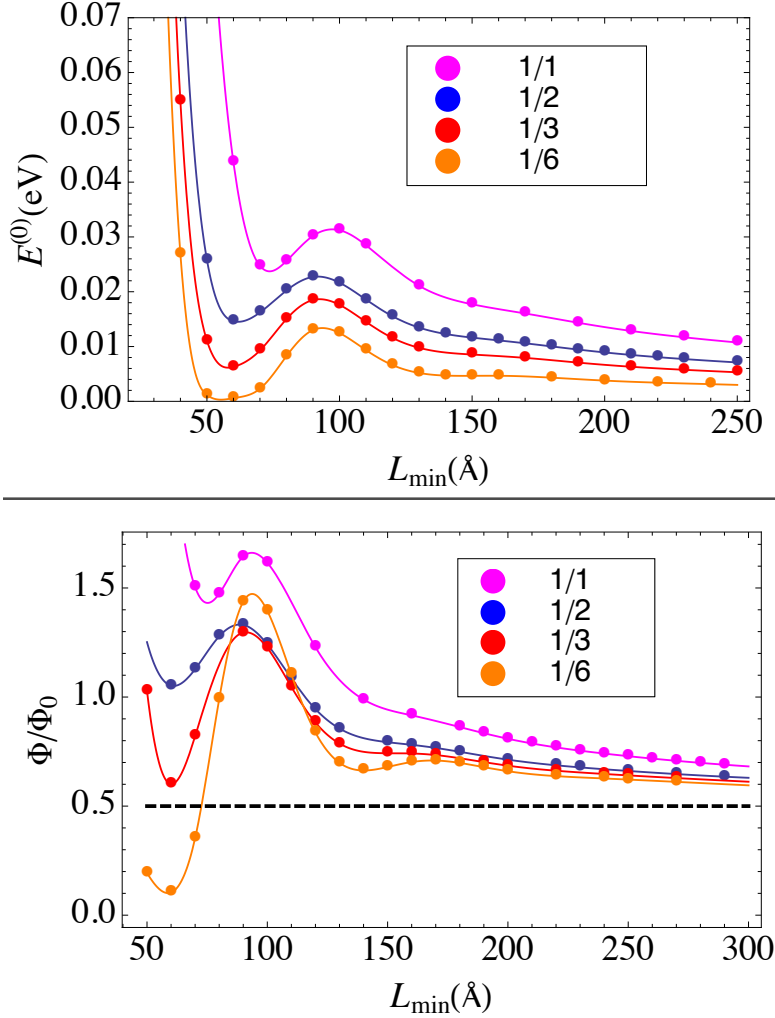


Figure 3.7: Upper panel: gap energy (in units of eV) as a function of the length of smaller side  $L_{min}$  (in units of Å) in the case of rectangular cross-sections with different aspect ratios. Lower panel: magnetic flux (in units of quantum flux  $\Phi_0$ ) corresponding to gap closing as a function of  $L_{min}$  (in units of Å) in the case of rectangular cross-sections with different aspect ratios.

In particular, we study the case of a wire with square section in the case of out of plane translational invariance (along z-axis as for the cylinder), but

we also analyze the case of translational invariance in the  $y$  axis direction (due to the hamiltonian symmetries, the case invariant in the  $x$  direction is indistinguishable). Also in this case the choice of parameters of the model is equal to that of the cylinder, therefore we consider  $C_1 = C_2 = 3.33eV\text{\AA}$  in Eq. (2.1). In this way, the spectrum for the two types of confinement remains the same. Therefore, for the wire with translational invariance in  $z$  or  $y$  direction, the same energy dispersion is obtained and, consequently, also the same values of the magnetic flux for the gap closing.

To analyze the size effects on the rectangular geometry, we investigate cross-sections with aspect ratio equal to  $1/1$ ,  $1/2$ ,  $1/3$ , and, finally,  $1/6$ . In the upper panel of Fig. 3.7, we plot the energy gap as a function of the length of the smaller side  $L_{min}$ . As in the case of cylindrical geometry, the energy gap tends to zero in the limit of infinite length. A numerical fit of our results provides the following asymptotic behavior:  $E \sim c_1/L + c_2/L^2$  (where  $c_1$  and  $c_2$  are parameters of the fit and depend from the investigated aspect ratio), in strong analogy with what we have found for the cylindrical nano-wire where we got  $E \sim \frac{M^2}{2R_0^2} - \frac{C_1}{2R_0}$ . Furthermore, also for this geometry, we find a non monotonic behavior with a maximum and a minimum for lengths between  $50$  and  $100\text{\AA}$ . In particular, the minimum in the energy gap gets smaller with reducing the aspect ratio. The case relative to the aspect ratio  $1/6$ , that is the lowest we studied, is really interesting. In fact we see that, for  $L_{min}$  around  $60\text{\AA}$ , the gap closes almost completely without the introduction of the magnetic field. As for the cylinder, we ascribe the presence of the minimum to geometrical effects, then, we find that specific wave-function density probability due to purely geometrical effects is able to compensate topological effects due to the Berry phase.

Another important aspect that emerges from this analysis is related to the properties of the surface electron states. The "numerically exact" calculations show that, in the nano-wire, the surface wave-function density probability exhibits a significant increase at the corners. Actually, in the upper right panel of Fig. 3.8, in the case of the maximum of the gap ( $L_{min} = 90\text{\AA}$ ,

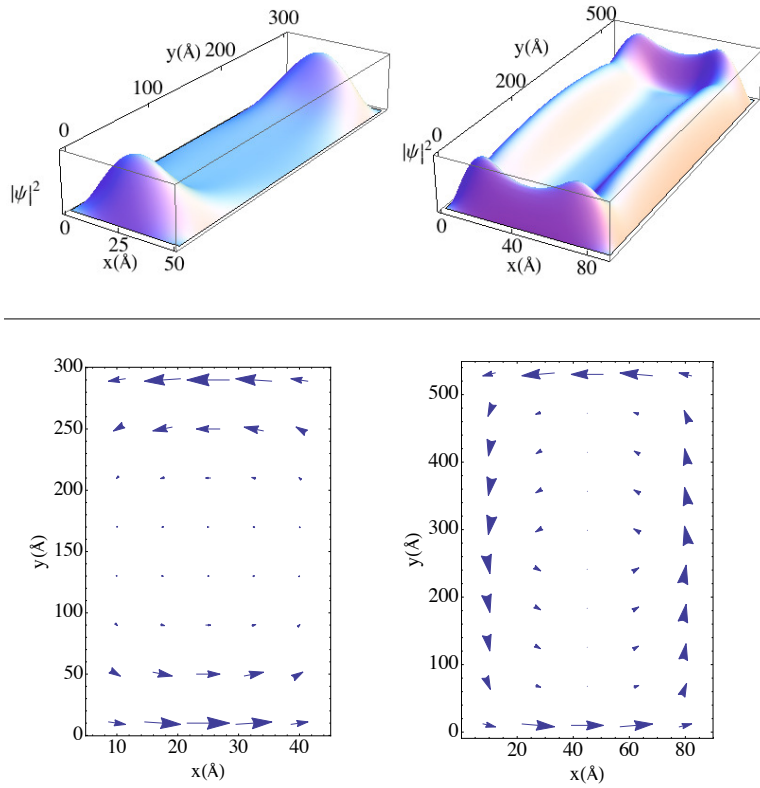


Figure 3.8: Upper panel: spatial probability density of the first subband state at  $k_z = 0$  for a rectangular wire with aspect ratio equal to  $1/6$ . Left plot for  $L_{min} = 60\text{\AA}$ , right plot for  $L_{min} = 90\text{\AA}$ . Lower panel: spin orientation corresponding to the first subband state at  $k_z = 0$  for a rectangular wire with aspect ratio equal to  $1/6$ . Left plot for  $L_{min} = 60\text{\AA}$ , right plot for  $L_{min} = 90\text{\AA}$ . For simplicity, in the two plots, only one of the two possible spin orientations is shown.

for aspect ratio  $1/6$ ), the spatial probability density of the first sub-band state is higher at the corners. Actually, it shows some analogies with the state corresponding to the maximum of the gap in the cylindrical nano-wire (see Fig. 3.4). In fact, as in the cylinder, it is not strongly confined on the perimeter. However, it shows also an enhanced corner density which represents the fingerprint of the rectangular cross-sections. It is worthy noticing that the formation of corner states is a consequence of the matching between

the wave-function along  $x$  and  $y$  sides. On the other hand, in the upper left panel of Fig. 3.8, the spatial probability density of the first sub-band in the case of the minimum of the gap ( $L_{min} = 60\text{\AA}$ , for aspect ratio 1/6) is completely different. A sort of side state takes place. It is clear that, at the minimum of the gap, one gets a complete decoupling of the two sides with smaller length along the perimeter. In this way the system reproduces the case of TI with a single confinement in the direction orthogonal to shorter sides. Therefore, one expects that the Dirac cone is recovered (zero gap in the upper panel of Fig. 3.7). We notice that rectangular wires with small aspect ratios bear some resemblance to thin films, which can be fabricated with a thickness of a few quintuple layers [78]. Actually, a non monotonic behavior of the gap has been also predicted in thin films with a thickness of the order  $30 - 40\text{\AA}$  [52]. This length is of the same order of that where in thin wires the oscillatory behavior of the gap is found. We point out that, however, on that length scale, the features of the first sub-band state for rectangular wires are different from those of thin films.

The case of confinement in the  $xz$  plane and invariance along the  $y$  direction is more complicated. If we consider a square cross-section of small size, all the three eigenvalues  $\lambda_x$ ,  $\lambda_y$  and  $\lambda_z$  of the spin components are not zero and comparable. In this way, the eigenvalues of the spin are such that, along the  $x$  direction of the cross-section of the wire, there is  $\lambda_x$  on one side and  $-\lambda_x$  on the other. Instead, the value of  $\lambda_y$  and  $\lambda_z$  is different from zero on all four sides of the square cross-section. If we increase the size of the square, however, we observe that the two components  $\lambda_y$  and  $\lambda_z$  decrease slowly, remaining only the component  $\lambda_x$  unchanged. In the asymptotic limit, for the case of translational invariance along  $y$  direction, the spin still turns around the perimeter, but in such a way that it vanishes along the two sides in the  $z$  direction. This occurs more easily in a geometry with a strong asymmetry along the sides, for example when one decreases the aspect ratios. The behavior of the spin for this confinement can be ascribed to the fact that, already with a single in-plane confinement, for example a confinement of the three-

dimensional material only along the  $x$  direction, the corresponding surface states along  $yz$  plane are not described by a Rashba hamiltonian responsible for a simple spin-momentum locking [76]. In particular, it is along the  $z$  direction that the spin behavior is more complicated. Indeed, in the case of nano-wire with a double confinement, it is on the  $z$  side that the spin has a different behavior in comparison with that of the cylinder and rectangular wire with translational axes along  $z$  direction (confinement in  $xy$  plane).

# Chapter 4

## Plasmon in topological insulator: cylindrical nano-wire

In the previous chapter we saw how in a TI nano-wire, the Berry phase opens a small gap at the  $\Gamma$  point, hampering the formation of the Dirac cone and promoting the formation of different energy sub-bands corresponding to surface states. The gap gets closed for a nano-wire with an infinite cross-section or with a finite cross-section upon the application of magnetic field which reduces the effects of the Berry phase. Also from the point of view of electronic excitations to the surface of these materials interesting features due to Berry phase are observed. In particular the collective plasmon excitations in TI, as discussed in the first chapter, have attracted a huge interest for their potential applications in quantum computing [79,80], terahertz detectors [81] and spintronic devices [82]. Only recently plasmons were observed in TI showing high frequency-tunability in the mid-infrared and terahertz spectral regions [83,85].

The random phase approximation for the dielectric function has been used for gapped Dirac systems in different dimensions [86,88], but, as far as we know, not for the cylindrical nano-wire geometry. In this chapter we extend those studies to the case a cylinder [89] exploiting the analytical electron wave functions that have been calculated in the previous chapter, for a TI

cylindrical nano-wire with a finite radius in the continuum limit. As part of this thesis, we analyze the system response considering the Coulomb interaction between electrons treating the interaction at the level of RPA. We provide an analytical solution of the inverse dielectric function, and, then, of the dynamic factor structure, relevant to study the response of the system to electronic scattering processes. The knowledge of these quantities in the limit of high surface density and infinite radius (two-dimensional surface) is used as a benchmark for the theoretical calculations.

The analysis starts from the case of zero surface density, i.e. when the chemical potential is inside the small gap opened in the spectrum of the surface states by the effects of the Berry phase. In this case it is possible to observe a plasmon dispersion of inter-band nature that exhibits a minimum threshold value of the momentum along the cylinder axis. Very interesting results are obtained when an applied longitudinal magnetic field closes the gap at half quantum flux and removes the degeneracy of the states by splitting the nano-wire sub-bands. As effect of this field, in the dynamic structure factor, we observe a well-defined magneto-plasmon peak with a long life-time and an another excitation peak, resulting from the splitting of the same sub-band, at higher frequency and with lower spectral weight. When the chemical potential crosses the first sub-bands, it is possible to observe the existence of both inter- and intra-band excitations with very different frequencies. With increasing the electron density, the most important electronic excitations become those of intra-band nature. Moreover, the increase of density or of the cylinder radius induces a cross-over to the two-dimensional regime where the effects of the magnetic field are no more relevant.

The chapter is divided as follows: in the first section, starting from the electronic model for a  $Bi_2Se_3$  cylindrical nano-wire, we obtain the analytical form of the susceptibility and the dynamic structure factor. In the second section, inter-band plasmons are analyzed for zero surface density. Finally,

in the third section, the case of a finite surface density is discussed. Details of the calculations are included in Appendix C and D.

## 4.1 Susceptibility and dynamic structure factor

The eigenvalues and eigenvectors found in 3.1 and 3.6 in the previous chapter for a cylindrical nano-wire represent the starting point for the calculation of the free electron charge susceptibility (or polarization function). Then, within the RPA theory for the electron-electron Coulomb interaction the dielectric function is obtained. In this section, we focus on the main results since more details of the calculations are provided in Appendices C and D. We can now say that since we consider radii definitely higher than  $100\text{\AA}$ , for the expression of the energy we consider that in 3.8 with  $C_1 = C_2$ . Using surface single-particle energies and states labelled by  $\alpha$ , one can calculate the free electron susceptibility  $\chi(\vec{r}, \vec{r}'; \omega)$  (or polarization function) at zero temperature:

$$\chi(\vec{r}, \vec{r}'; \omega) = \sum_{\alpha, \alpha'} \frac{f(\epsilon_{\alpha'}) - f(\epsilon_{\alpha})}{\epsilon_{\alpha'} - \epsilon_{\alpha} + \hbar(\omega + i0^+)} \psi_{\alpha'}^*(\vec{r}) \psi_{\alpha}(\vec{r}) \psi_{\alpha}^*(\vec{r}') \psi_{\alpha'}(\vec{r}'), \quad (4.1)$$

where  $f(\epsilon_{\alpha})$  is the Fermi function at zero temperature calculated at the energy  $\epsilon_{\alpha}$ , which is related to the chemical potential  $\mu$ . Since, in the case of the TI nano-wire, we use the eigenvalues (3.8) and the corresponding eigenfunctions (3.1) in cylindrical coordinates. Hence, in eq.(4.1),  $\alpha = (k, m, s = \pm)$ ,  $\alpha' = (k+q, m+l, s' = \mp)$ , where  $q$  is the transferred momentum along  $z$  axis,  $l$  is the relative number linking the sub-band  $m$  to the sub-band  $m' = m+l$ . Indeed,  $m$  and  $m' = m+l$  are the variables conjugate to  $\phi$  and  $\phi'$ , respectively. The parameter  $s$  is the sign of the eigenvalue. The susceptibility for the cylinder becomes

$$\chi(\vec{r}, \vec{r}'; \omega) = \chi(\rho, \rho', z - z', \phi - \phi'; \omega) = R^2(\rho) R^2(\rho') \chi_0(z - z', \phi - \phi'; \omega), \quad (4.2)$$

where  $\chi_0(z - z', \phi - \phi'; \omega)$  reflects the translation invariance along  $z$  axis and the rotation invariance around  $z$  axis due to the cylindrical geometry (details about  $\chi_0(z - z', \phi - \phi'; \omega)$  are provided in Appendix (C)). Clearly, the susceptibility is different from zero for values of the positions  $\vec{r}$  and  $\vec{r}'$  inside the cylinder. We point out that, along the radial direction, the susceptibility depends on the product of the squares of the radial functions calculated in  $\rho$  and  $\rho'$ , respectively. This separation of the radial dependences will be of paramount importance for the calculation of the inverse of the dielectric function. Finally, we calculate the dielectric function due to the surface charges of the TI cylindrical wire within the RPA theory for the electron-electron Coulomb interaction. Even if we confine electrons within the cylinder, the generated electromagnetic fields affects all the space and, therefore, the dielectric function is defined also outside the cylinder. Within the RPA approximation, the dielectric constant  $\epsilon(\vec{r}, \vec{r}'; \omega)$  is defined in the following way:

$$\epsilon(\vec{r}, \vec{r}'; \omega) = \delta(\vec{r} - \vec{r}') - \int d\vec{r}_1 V(\vec{r} - \vec{r}_1) \chi(\vec{r}_1, \vec{r}'; \omega), \quad (4.3)$$

where  $V(\vec{r} - \vec{r}_1) = e^2/|\vec{r} - \vec{r}_1|$  is the Coulomb potential in real space and the integration is over the volume enclosed by the cylinder. We emphasize again that  $\vec{r}$  can assume values both inside and outside the cylinder unlike  $\vec{r}_1$  and  $\vec{r}'$ . In the next section, we will see that, in order to describe the response of the system to external probes, we need to calculate the inverse of the dielectric function  $\epsilon^{-1}(\vec{r}, \vec{r}'; \omega)$ . As discussed in Appendix (D), in order to make the inversion of the dielectric function in Eq.(4.3), we solve analytically an integral equation with a separable variable kernel. Now we provide an analytic form of the dynamic structure factor for a TI cylindrical wire. This quantity is relevant for example in electron-energy-loss experiments (EELS), where an electron impinges on the sample and loses energy by exciting plasmons. This energy loss is given by the imaginary part of the integral of the potential created by the electron, and the induced charge [90]. When the potential due to an electron is taken proportional to a plane wave, one can calculate the response function  $L(\vec{q}; \omega)$  making a double Fourier transform of

the inverse dielectric function:

$$L(\vec{q}; \omega) = -Im \left[ \frac{1}{V} \int \int d\vec{r} d\vec{r}' \epsilon^{-1}(\vec{r}, \vec{r}'; \omega) e^{-i\vec{q}\cdot\vec{r}} e^{i\vec{q}\cdot\vec{r}'} \right], \quad (4.4)$$

where  $V$  is the volume enclosed by the cylinder and the two integrals are over all the space. It can be shown that the response function  $L(\vec{q}; \omega)$  in Eq.(4.4) is proportional to the dynamic structure factor [91], whose peaks characterize the electronic excitations, such as plasmons, induced by scattering processes. Since the system has translational invariance in the  $z$  direction and rotational invariance around  $z$  axis, as discussed in Appendix (D), one can use partial Fourier transforms in  $q$  and  $l$  for the Coulomb potential  $V(\vec{r} - \vec{r}_1)$  and the polarization function  $\chi(\vec{r}_1, \vec{r}')$  obtaining the following result:

$$L(q, |\mathbf{q}_{||}|; \omega) = -\frac{2}{R_0^2} Im \left[ \sum_l \frac{\chi_0(q, l; \omega)}{1 - \chi_0(q, l; \omega) \tilde{V}_{q,l}} \right. \\ \left. \times \int_0^{R_0} d\rho' \rho' J_l(|\mathbf{q}_{||}|\rho') R(\rho')^2 \int_0^\infty d\rho \rho J_l(|\mathbf{q}_{||}|\rho) S_{q,l}(\rho) \right]. \quad (4.5)$$

where  $|\mathbf{q}_{||}|$  is the modulus of the momentum transverse to the axis  $z$  of the cylinder (parallel to the  $x - y$  plane), and  $J_l$  are the Bessel functions of the first kind. In Eq.(4.5),  $\tilde{V}_{q,l}$  takes into account the Coulomb repulsion:

$$\tilde{V}_{q,l} = 4\pi \int d\rho \rho R^2(\rho) S_{q,l}(\rho), \quad (4.6)$$

since  $S_{q,l}(\rho)$  is defined as

$$S_{q,l}(\rho) = e^2 \int d\rho' \rho' R^2(\rho') I_l(|q|\rho_<) K_l(|q|\rho_>), \quad (4.7)$$

with  $I_l$  and  $K_l$  the modified Bessel functions of the first and second kind, respectively. In Appendix (C) we report the expansion of the Coulomb potential in cylindrical coordinates clarifying that  $\rho_<$  and  $\rho_>$  appearing in Eq.(4.7) represent the smaller and larger of  $\rho$  and  $\rho'$ , respectively. The zeros of the denominator in equation (4.5) provide the plasmon dispersions. Indeed, one has the equation

$$1 - \chi_0(q, l; \omega) \tilde{V}_{q,l} = 0 \quad (4.8)$$

typical of the RPA approach. In this paper, we focus on the contributions for  $|\mathbf{q}_{\parallel}| \rightarrow 0$ , therefore we consider probes propagating parallel to the axis of the cylinder. This means that we only have to analyze the term  $L(q, 0; \omega)$  corresponding to  $l = 0$ :

$$L(q, 0; \omega) = -\frac{2}{R_0^2} \text{Im} \left[ \frac{\chi_0(q, 0; \omega)}{1 - \chi_0(q, 0; \omega) \tilde{V}_{q,0}} \int_0^\infty d\rho \rho S_{q,0}(\rho) \right]. \quad (4.9)$$

In the limit of large radius  $R_0$  and small  $q$ , it is possible to show how the potential  $R_0 \tilde{V}_{q,0}$  converges to the two-dimensional Coulomb potential  $V_q^{2D} = 2\pi e^2/q$ . As reported in Appendix C, in the limit of infinite radius, the dynamic polarization  $\chi_0(q, 0; \omega)$  also converges to that of the two-dimensional case [88].

For a system with particle-hole symmetry,  $\chi_0(q, l; \omega) = \chi_0(q, l; -\omega)^*$ . Therefore, the results will be given only for chemical potential  $\mu > 0$ ,  $\omega > 0$  and  $q > 0$ . Furthermore, since we will consider only the  $l = 0$  contribution, in the following, we name  $\tilde{V}_{q,0} = \tilde{V}_q$  and  $\chi_0(q, 0; \omega) = \chi_0(q; \omega)$ . As shown in Appendix C and following what done in literature, we can divide the polarization function for massive Dirac electrons into three contributions:

$$\chi(q; \omega) = -\chi_\infty^-(q; \omega) + \chi_\mu^-(q; \omega) + \chi_\mu^+(q; \omega), \quad (4.10)$$

where the subscripts are related to the position of the chemical potential:  $-\chi_\infty^-(q; \omega)$  is the contribution for  $\mu < \Delta$ ,  $\chi_\mu^-(q; \omega) + \chi_\mu^+(q; \omega)$  is the additional contribution for  $\mu > \Delta$ . In Eq.(4.10), the superscript + indicates intra-band transitions, while the superscript - inter-band transitions. Therefore, one can define

$$\begin{aligned} \chi_T^\pm(q; \omega) &= \frac{1}{4C_2\pi^2} \sum_m \int_{-T}^T dk \left[ 1 \pm \frac{k(k+q) + \tilde{\Delta}_m^2(R_0)}{\tilde{\epsilon}_{k,m} \tilde{\epsilon}_{k+q,m}} \right] \\ &\times \left[ \frac{\tilde{\epsilon}_{k,m} \mp \tilde{\epsilon}_{k+q,m}}{(\tilde{\omega} + i\tilde{\eta})^2 - (\tilde{\epsilon}_{k,m} \mp \tilde{\epsilon}_{k+q,m})^2} \right], \end{aligned} \quad (4.11)$$

with  $\tilde{\Delta}_m(R_0) = \tilde{\Delta}(R_0)(1 + 2m - 2r)$ ,  $\tilde{\omega} = \hbar\omega/C_2$ ,  $\tilde{\epsilon}_{k,m} = \epsilon_{k,m}/C_2$ ,  $\tilde{\mu} = \mu/C_2$ , and  $\tilde{\eta} = \eta/C_2$ , with  $\eta$  very small positive energy. The integration limit  $T$  is equal to infinity for  $\mu$  in gap, while  $T = \sqrt{\tilde{\mu}^2 - (1 + 2m - 2r)^2 \tilde{\Delta}^2}$  otherwise.

The sum over  $m$  for the case  $\mu < \Delta$  has to be made over all sub-bands, then  $m$  goes from minus infinity to infinity. On the other hand, for  $\mu > \Delta$ , the sum is limited by the condition of existence of  $T$ , that is  $\tilde{\mu}^2 - \tilde{\Delta}^2(1+2m-2r)^2 > 0$ , with  $m$  integer.

## 4.2 Zero surface density

In a previous section, we have pointed out that the effect of the Berry phase is to open a small gap in the energy spectrum. In this section, we provide a description of the inter-band surface plasmons, when the chemical potential  $\mu$  is in the Berry gap and neither holes nor electrons are present at the TI surface.

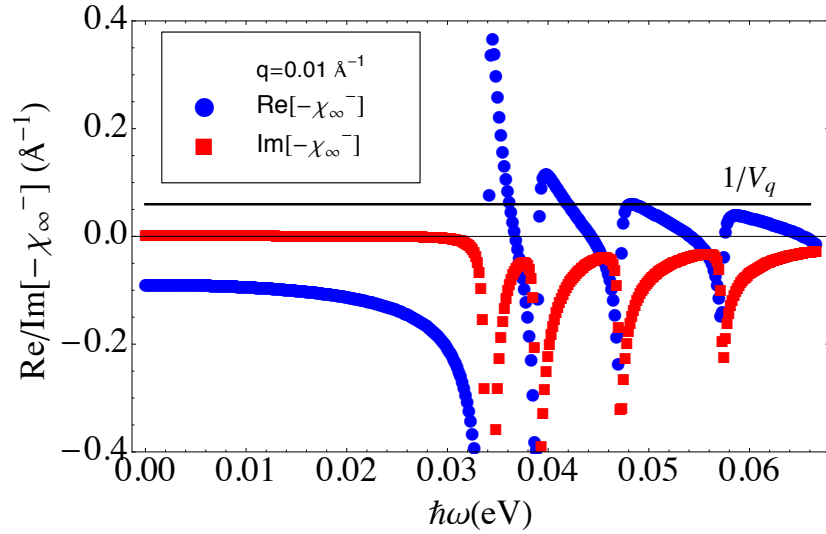


Figure 4.1: Real (blue circles) and imaginary (red squares) part of the susceptibility (in units of  $\text{\AA}^{-1}$ , obtained numerically with  $\eta = 1.5 \times 10^{-4} \text{ eV}$ ) as a function of the energy (in units of eV) for  $q = 0.01 \text{ \AA}^{-1}$  at  $R_0 = 500 \text{ \AA}$  and  $r = 0$ . Large variations of the real part are related to those of the imaginary part in correspondence with the same value of  $\hbar\omega = C_2 \sqrt{q^2 + 4\tilde{\Delta}^2(1+2m-2r)^2}$  at  $r = 0$ . The intersections that  $1/\tilde{V}_q$  (black line) has with  $\text{Re}(-\chi_\infty^-)$  give the plasmon frequencies.

This means that the chemical potential is in the middle of the gap:  $\mu = 0$  (due to the particle-hole symmetry). As shown in Figure (3.2), the basic particle-hole excitations are due to transitions from states with negative energies ( $s = -$ ) to those with positive energies ( $s = +$ ). In this section, considering the chemical potential in gap ( $\mu = 0 < \Delta$ ), we need only to analyze the contribution  $-\chi_{\infty}^-$  of the equation (4.10). Moreover, the  $l = 0$  contribution to the susceptibility come only from inter-band transitions associated to the same sub-band number  $m$  but opposite  $s$  (see for clarity also Fig.(3.2)). We determine the plasmon dispersion from Eq.(4.8) considering  $l = 0$ :

$$1 - \text{Re} [\chi_0(q; \omega + i\eta)] \tilde{V}_q = 0. \quad (4.12)$$

We solve numerically equation (4.12) taking  $\eta$  (see Eq. (4.11)) very small but finite. As shown in an example in Figure (4.1), the equation has more solutions corresponding to different frequencies, all with a finite imaginary part. Furthermore, for each value of  $R_0$ , these inter-band plasmons show a minimum frequency related to the finite gap  $\Delta(R_0)$ . In fact, the real part  $\text{Re}(-\chi_{\infty}^-)$  is completely negative for  $\hbar\omega < C_2\sqrt{q^2 + 4\tilde{\Delta}^2(R_0)}$ , instead it assumes also positive values for larger values of frequency. Since the solutions of the equation (4.12) exist only for values of  $\text{Re}(-\chi_{\infty}^-) > 0$ , plasmon dispersion exists only above the curve  $\hbar\omega = C_2\sqrt{q^2 + 4\tilde{\Delta}^2(R_0)}$ . In Fig. (4.2a) we report these curves for different cylinder radii. Associated with minimum frequency  $\omega$ , there is also a minimum momentum  $q_t$  for which equation (4.12) admits a solution. This is clearly shown in Figure (4.2a). With decreasing the radius  $R_0$ , the gap  $\Delta(R_0)$  gets enhanced, therefore this minimum  $q_t$  becomes bigger. It is worthwhile noting that, due to the existence of a minimum threshold  $q_t$ , it is not possible to derive an analytical expression of the dispersion in the limit of small  $q$ , as in the case of intra-band plasmons. In Fig. (4.2a) we report our numerical analysis for the plasmon dispersions at different cylinder radii. It is important to analyze the behavior of the potential  $\tilde{V}_q$  in the limit

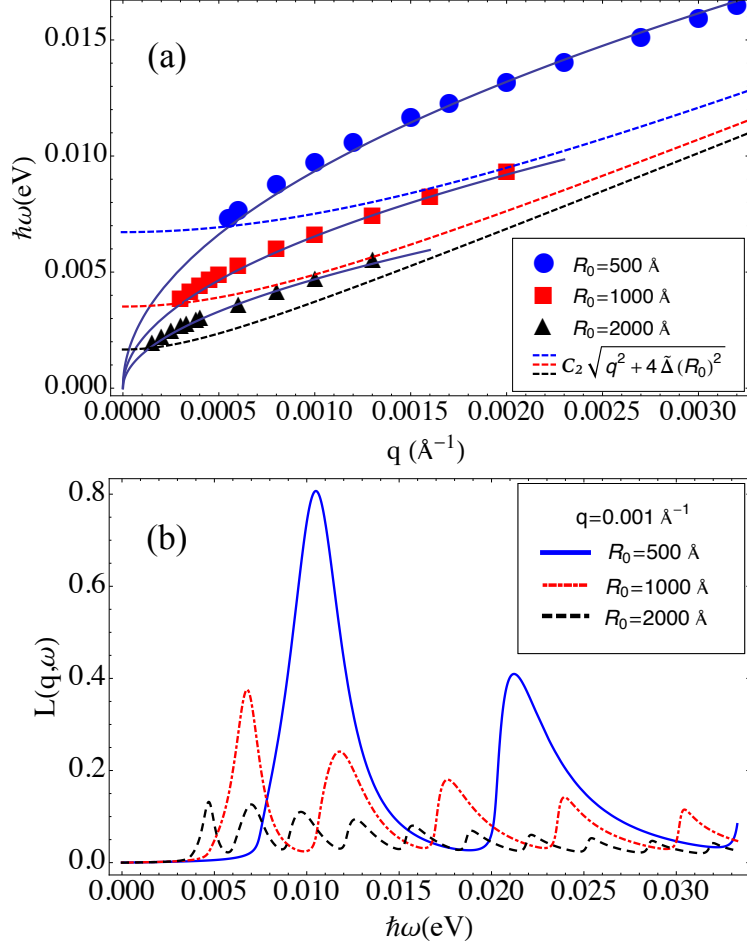


Figure 4.2: a) Inter-band plasmon dispersion (in units of eV) as a function of the momentum  $q$  (in units of  $\text{\AA}^{-1}$ ) for different values of the cylinder radius. Plasmon excitations are present only for energies larger than  $C_2\sqrt{q^2 + 4\tilde{\Delta}^2(R_0)}$ . The fits (continuous lines) of the dispersions indicate that, above the minimum  $q$ , the dispersion is square root like:  $\hbar\omega = \alpha\sqrt{q}$ . For  $R_0 = 500\text{\AA}$ ,  $\alpha \sim 0.3eV\text{\AA}^{1/2}$ ; for  $R_0 = 1000\text{\AA}$ ,  $\alpha \sim 0.2eV\text{\AA}^{1/2}$ ; for  $R_0 = 2000\text{\AA}$ ,  $\alpha \sim 0.155eV\text{\AA}^{1/2}$ . b) the dynamic structure factor  $L(q; \omega)$  as a function of the energy (in units of eV) at  $q = 0.001 \text{\AA}^{-1}$  for different values of the cylinder radius.

of small  $q$ , since two different regimes are present:

$$\tilde{V}_q \sim \begin{cases} e^2 K_0(qR_0) \mapsto -e^2 \log(qR_0), & q \ll 1/R_0, \\ e^2/(qR_0) = V_q^{2D}/R_0, & q > 1/R_0. \end{cases} \quad (4.13)$$

Indeed, for  $q \ll 1/R_0$ ,  $\tilde{V}_q$  shows a one-dimensional type behavior, while, for  $q > 1/R_0$  it is more two-dimensional [86]. Inter-band plasmons are stable only for  $q > q_t$ , which is comparable with  $1/R_0$  in the absence of the magnetic field. Therefore, as shown in Figure (4.2a), the plasmon dispersion is similar to the two-dimensional case ( $\omega \sim \sqrt{q}$ ). Moreover, we observe that, for larger values of  $q$ , the dispersion tends towards  $C_2q$ . For the radii considered in this paper, the linear regime is reached at most at  $q > 0.01\text{\AA}^{-1}$ . This value of  $q$  is in any case smaller than  $0.1\text{\AA}^{-1}$ , which represents the order of magnitude of the wave-vector at the border of the Brillouin zone in materials like  $Bi_2Se_3$ . Therefore, the analysis pursued in this paper considers values of the wave-vector  $q$  where RPA is known to give a reliable description of the electronic excitations. The dynamic structure factor calculated in equation (4.9) provides the spectral weights associated with the plasmon frequencies. As shown in Figure (4.2b), this allows to estimate the damping of the plasmon and its lifetime. In the case of inter-band plasmon studied in this section, we stress that, for long wavelength, only the first peak corresponds to a solution of equation (4.12). The peaks at higher frequencies are associated to minima of the right side member of eq.(4.12), and correspond to higher values of the sub-band number  $m$ . Actually, we notice that only the first peak has a Lorentzian shape while the others become progressively more asymmetric with increasing the frequency. As shown in Figure (4.2b), for the radius  $R_0 = 500\text{\AA}$ , the first plasmon peak almost saturates the spectral weight, while, for the radius  $R_0 = 2000\text{\AA}$ , it has a spectral weight comparable with high frequency peaks. In any case, the increase of the radius  $R_0$  induces a decrease of the spectral weight as we see in Figure (4.2b) and a shift of the plasmon frequency toward lower values. If one further increases the value of  $R_0$ , the spectral weight of the inter-band plasmon frequency falls to zero. Indeed, as discussed in Appendix C, for  $R_0 \rightarrow \infty$ , one reaches, as expected, the two-dimensional limit where inter-band plasmons are no more present. A similar decrease of the plasmon spectral weight is observed when wave-vector  $q$  increases.

The application of a magnetic field along the axis of the cylindrical wire introduces a magnetic flux  $\Phi$  which changes the gap value through the term  $r = \Phi/\Phi_0$ . This way, it is possible to study the effects of the Berry phase on Dirac inter-band plasmon frequencies in nano-wires up to the closing of the gap. As shown in Figure (3.1), the additional effect of the magnetic field is to remove the degeneracy of energy states and it has an interesting effect on the dynamic structure factor. In fact, the presence of the magnetic field separates a peak into two: one at a frequency lower and the other at a frequency larger than the peak at  $r = 0$ , as shown in Figure (4.3a). We notice that the sum of the spectral weights of two new plasmon peaks is similar to that of the main peak for zero magnetic field. The redistribution of this weight is not homogeneous, indeed almost all the contribution is given by the low frequency peak, as we show in the inset of Figure (4.3a). Not only the integral of this peak is more important but also the peak itself is better defined being narrower and higher. Indeed, the closure of the Berry gap caused by the magnetic field gives rise to a magneto-plasmon with a very long life-time, therefore more likely to be observed experimentally. Our analysis suggests that, in the presence of a magnetic field, the magneto-plasmon peak should be observed at lower frequency. Furthermore, for a magnetic field near half quantum flux, as shown in Figure (4.3b) for  $r = 0.4$ , when the gap is practically closed, the minimum threshold  $q_t$  becomes very close to zero. As discussed in equation (4.13), the potential for values of  $q \ll 1/R_0$  has a one-dimensional behavior, and, therefore, also the magneto-plasmon for wavelength  $q_t < q \ll 1/R_0$  acquires a dispersion typical of one-dimensional systems:  $\omega \propto q\sqrt{K_0(qR_0)}$ , as shown in Figure (1.4b). Unlike the case without magnetic field, a threshold minimum  $q_t$  tending to zero with the closing of the gap allows us to explore the region which has a one-dimensional character. Finally, with the closing of the gap at  $r = 0.5$ , we restore the degeneracy in the sub-bands but the resulting excitations are at frequencies lower than those for zero magnetic field.

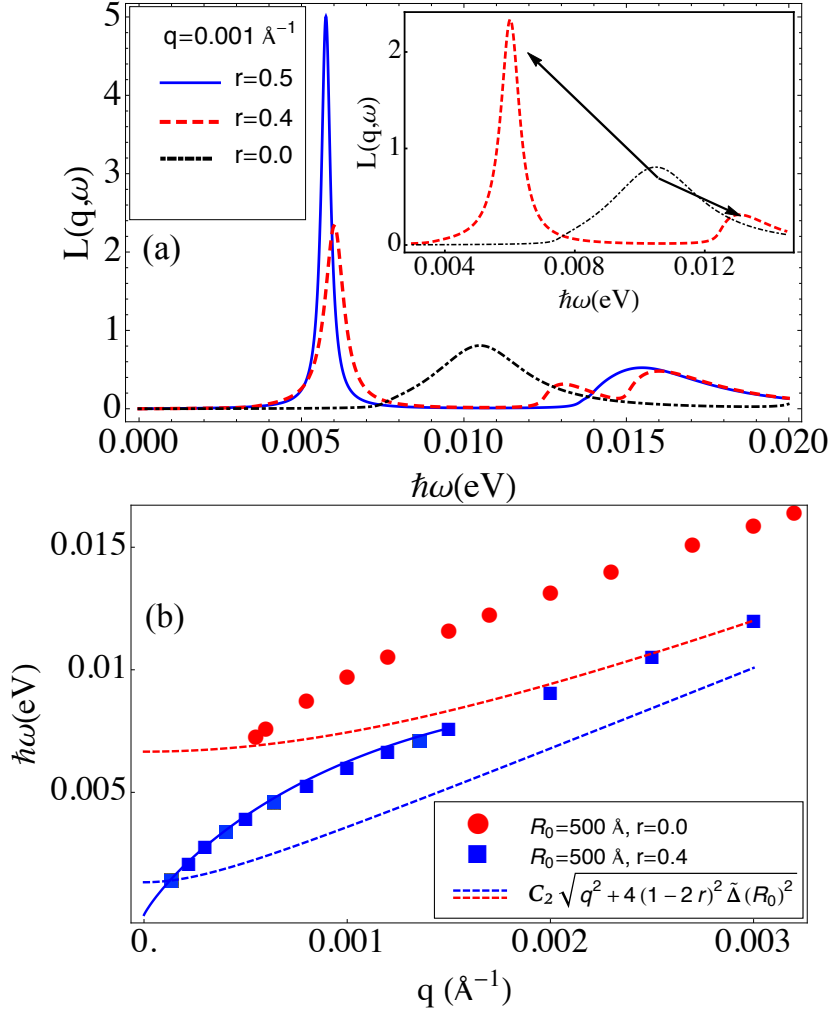


Figure 4.3: a) The dynamic structure factor as a function of the energy (in units of eV) at  $R_0 = 500 \text{ \AA}$  and  $q = 0.001 \text{ \AA}^{-1}$  for some values of the ratio of the magnetic fluxes. Note the separation of the plasmon peak into two peaks (shown in the inset by the arrows). b) Plasmon dispersion (in units of eV) as a function of the momentum  $q$  (in units of  $\text{\AA}^{-1}$ ) at  $R_0 = 500 \text{ \AA}$  for two values of  $r$ :  $r = 0$  (red circles),  $r = 0.4$  (blue squares). Plasmon excitations are present only for energies larger than  $C_2 \sqrt{q^2 + 4(1 - 2r)^2 \tilde{\Delta}^2(R_0)^2}$ . The fit (continuous line) of the  $r = 0.4$  curve provides a dispersion typical of a one-dimensional system:  $\hbar\omega = \alpha q \sqrt{K_0(qR_0)}$ , with  $\alpha = 6.5 \text{ eV \AA}^{-1}$ .

Indeed, the resulting peak of the dynamic structure factor has a similar spectral weight but it is much higher and narrower. We will see in the next section that the nature of this magneto-plasmon at zero gap is different from that of inter-band type since it is similar to an intra-band plasmon.

### 4.3 Finite surface density

In this section we analyze the case of finite surface electron density:  $\mu > \Delta$ . In order to find the dispersion and spectral weight associated with the plasmon excitations, we have to consider all three contributions of equation (4.10). We start analyzing the case of low electron density to understand how the crossover between inter- and intra-band plasmon takes place.

We define the electron density for the case of a cylindrical wire as follows:

$$n = \frac{1}{2\pi^2 R_0} \sum_{m=-M+1}^{M-1} \sqrt{\tilde{\mu}^2 - (1 + 2m - 2r)^2 \tilde{\Delta}^2}, \quad (4.14)$$

where  $M$  is the number of the sub-bands intersected by chemical potential. We choose to study the case in which the potential intersects a single sub-band equivalent to  $m = 0$ . For this condition we have an electron density equal to  $n = 10^{10} \text{ cm}^{-2}$ . This way, the equation (4.12) always admits solution for each value of momentum  $q$  due to the intra-band contribution given by  $\chi_\mu^+(q; \omega)$ , unlike the case of  $\mu = 0$  studied in the previous section where there was a minimum threshold  $q_t$ . For this reason, it is possible to make the  $q \rightarrow 0$  limit for the polarization function valid at each  $\omega$ :

$$\chi_0(q \rightarrow 0; \omega) = \frac{1}{2\pi^2 C_2} \sum_m \frac{k_F(m) \tilde{\mu} q^2}{\tilde{\mu} \omega^2 - k_F(m) q^2}, \quad (4.15)$$

where  $k_F(m) = \sqrt{\tilde{\mu}^2 - (1 + 2m - 2r)^2 \tilde{\Delta}^2}$  and the sum on  $m$  depends always on the number of sub-bands intersected by the chemical potential. At this point we have all the ingredients to define the intra-band plasmon analyzing the dispersion and the response function.

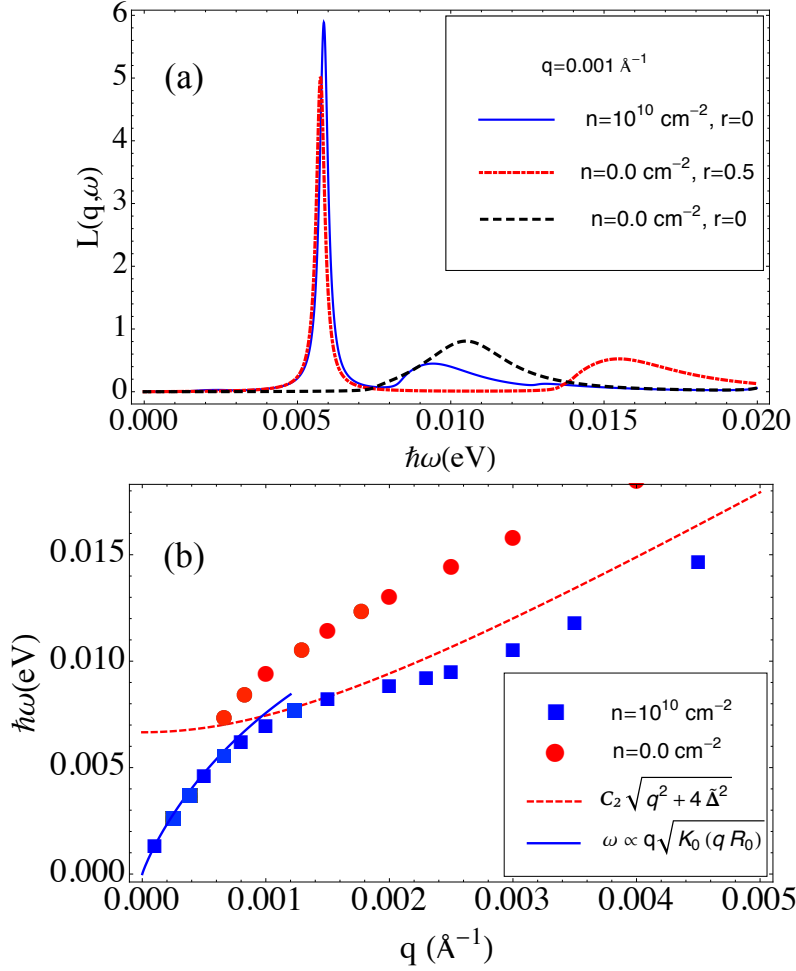


Figure 4.4: a) The dynamic structure factor as a function of the energy (in units of eV) at  $R_0 = 500 \text{ \AA}$  and  $q = 0.001 \text{ \AA}^{-1}$  for electronic density  $n = 10^{10} \text{ cm}^{-2}$  and  $r = 0$  (solid blue line),  $n = 0 \text{ cm}^{-2}$  and  $r = 0$  (dashed black line), and  $r = 0.5$  (red dotted line). b) Plasmon dispersion (in units of eV) as a function of the momentum  $q$  (in units of  $\text{\AA}^{-1}$ ) in the case of single occupied subband with  $n = 10^{10} \text{ cm}^{-2}$  (blue squares) compared with the inter-band contribution for zero electronic density (red circles). Inter-band plasmons are present only for energies larger than  $C_2 \sqrt{q^2 + 4(1 - 2r)^2 \tilde{\Delta}^2(R_0)}$ . Note how the analytical solution (continuous line) for small  $q$  matches the points obtained numerically.

We start from the case of electron density  $n = 10^{10} \text{ cm}^{-2}$  and  $R_0 = 500\text{\AA}$  corresponding to a single occupied sub-band. We note immediately that  $L(q; \omega)$  (see Figure (4.4a)) exhibits two peaks. The first one at lower energy is well defined with shape, spectral weight and position very similar to those we have found for the magneto-plasmon at  $\mu = 0$  and  $r = 0.5$ . On the contrary, the second peak at higher energy is much broader and similar to the peak associated at the inter-band plasmon observed at  $\mu = 0$  and  $r = 0$ . Actually, the effect of the gap closure in the presence of the magnetic field at  $\mu = 0$  gives a result very close to what observed for low density in the absence of the field. Therefore, for low density (only first sub-band occupied) we observe that the inter-band Dirac plasmon still survives even if its spectral weight is reduced, but a new well defined excitation (intra-band plasmon) gets in. Finally, to derive the dispersion for long wavelength, we can consider equation (4.15) and replace it in Eq.(4.12) thus obtaining the behaviors for the case of single occupied sub-band:

$$\frac{1}{2\pi^2 C_2} \frac{k_F(0) \tilde{\mu} q^2}{\tilde{\mu} \omega^2 - k_F(0) q^2} \tilde{V}_q = 1, \quad (4.16)$$

which has solution  $\omega_p = q \sqrt{C_2^2 k_F^2 \pi + 4k_F C_2 \tilde{\mu} \tilde{V}_q / \sqrt{\pi \tilde{\mu}^2}}$ . We recall that  $\tilde{V}_q$  for  $q \rightarrow 0$  has different trends depending on whether  $q \ll 1/R_0$  (one-dimensional) or  $q > 1/R_0$  (two-dimensional). For a single sub-band, we call  $k_F(m=0) = k_F$ . Therefore, we find that the  $q \rightarrow 0$  behavior for the low density dispersion is of one-dimensional type with  $\omega_p \propto q \sqrt{K_0(qR_0)}$ . In fig.(4.4b) the analytic solution of equation (4.16) is shown as the continuous line and shows a very good agreement with the numerical data.

If we apply a magnetic field parallel to the axis of the cylinder, we remove the degeneration of energy sub-bands. Keeping constant the electron density to  $n = 10^{10} \text{ cm}^{-2}$  for  $R_0 = 500\text{\AA}$ , inevitably the chemical potential changes crossing more sub-bands. This depends on the ratio  $r$  of the fluxes as seen in equation (4.14). Therefore, if we take, for example, a value of  $r = 0.4$ , the chemical potential crosses two sub-bands instead of one as before. Even

in this case, by exploiting Eq.(4.15), we can get an analytical solution of the plasmon dispersion for large wavelength.

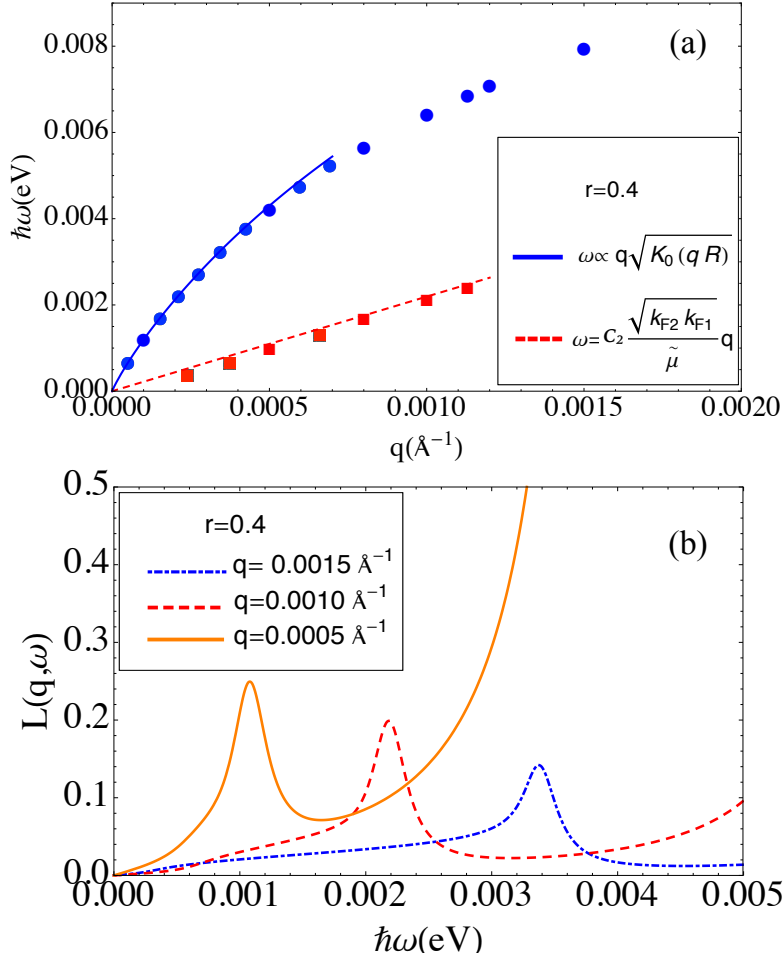


Figure 4.5: a) Plasmon dispersion (in units of eV) as a function of momentum  $q$  (in units of  $\text{\AA}^{-1}$ ) for  $n = 10^{10} \text{ cm}^{-2}$  and  $R_0 = 500 \text{ \AA}$  at  $r = 0.4$  in the case of two occupied sub-bands. We distinguish a solution for  $\omega > C_2 q$  (blue circles) and an other with a linear behavior for  $\omega < C_2 q$  (red squares) where  $k_{F1} = k_F(m = 0)$  and  $k_{F2} = k_F(m = -1)$ . Continuous lines indicate the analytical solutions. b) The dynamic structure factor as a function of the energy (in units of eV, energy range  $\hbar\omega < C_2 q$ ) for different values of wave-vector  $q$  at  $r = 0.4$  in the case of two occupied sub-bands with  $n = 10^{10} \text{ cm}^{-2}$ .

In fact, in the case of two sub-bands, in the limit of  $q \rightarrow 0$ , the relation in (4.16) becomes a bi-quadratic equation because we have a sum on  $m = 0$  and  $m = -1$  in Eq.(4.15). Hence, we get four solutions, two for positive frequencies and two with opposite frequencies, as shown in Figure (4.5a) for a specific case. A solution will be of the same type like in the single sub-band case ( $\omega \sim q\sqrt{K_0(qR_0)}$ ), the other will have a linear behavior in  $q$  for values  $\hbar\omega < C_2q$ . The analytical solution for the linear dispersion provides  $\omega = qC_2\sqrt{k_F(0)k_F(-1)}/\tilde{\mu}$ , although, as shown in Figure (4.5b), this solution have a spectral weight lower than the other for  $\hbar\omega > C_2q$ . In fact, for the density and parameters considered here, the spectral weight of the plasmon peak with linear dispersion is about ten times smaller than the other solution ( $\omega \propto q\sqrt{K_0(qR_0)}$ ) at higher frequency. For example, if we take a  $q = 0.5 \text{ m}\mathring{\text{A}}^{-1}$  the spectral weights of the two resulting plasmon peaks are  $8 \text{ meV}$  ( $\hbar\omega > C_2q$ ) and  $0.2 \text{ meV}$  ( $\hbar\omega < C_2q$ ), respectively.

A similar reasoning could be made for any number of sub-bands in the limit  $q \rightarrow 0$ . However, the analytical solutions of equation (4.12) would become more and more complicated increasing the number of sub-bands. At fixed radius  $R_0$ , increasing the number of sub-bands means considering higher densities. Also in this case an excitation for  $\hbar\omega > C_2q$  will be observed in the dynamic structure factor and the remaining will be all concentrated in the area  $\hbar\omega < C_2q$  like in the case of two sub-bands. For example, in a case of higher density, for example  $5 \times 10^{10} \text{ cm}^{-2}$  for  $R_0 = 500\mathring{\text{A}}$ , the chemical potential crosses three sub-bands. We get a plasmon excitation with a behavior of type  $\omega_p \propto q\sqrt{K_0(qR_0)}$  and the other two solutions are both linear in  $q$  at lower frequencies. More the electronic density increases, more the spectral weight of excitations present at  $\hbar\omega < C_2q$  decreases. In addition, the peak shape observed in the dynamic structure factor for these excitations is no longer a single peak as we see in Figure (4.5b) in the case of two sub-bands. Indeed, the structure becomes a continuous separated by the higher frequency narrow main peak (present for  $\hbar\omega > C_2q$ ) whose spectral weight gets enhanced with increasing the electron density. If the

electron density further increases, the spectral weight of the low frequency continuous becomes negligible in comparison with the main peak.

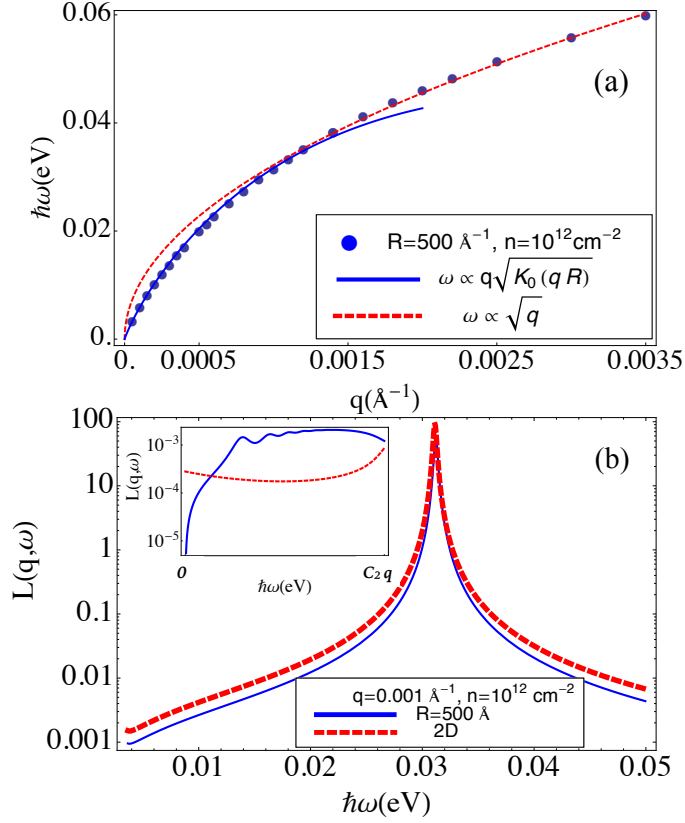


Figure 4.6: a) Plasmon dispersion (in units of eV, circles) as a function of momentum  $q$  (in units of  $\text{\AA}^{-1}$ ) for  $R_0 = 500\text{\AA}$  and  $n = 10^{12} \text{ cm}^{-2}$ . For  $q < 1/R_0$ , the dispersion is one-dimensional type:  $\hbar\omega = \alpha q\sqrt{K_0(qR_0)}$  (blue solid line) with  $\alpha = 33eV\text{\AA}$ . For  $q > 1/R_0$ , the dispersion is two-dimensional type:  $\hbar\omega = \beta\sqrt{q}$  (red dashed line) with  $\beta = 1,02eV\text{\AA}^{1/2}$ . b) Dynamic structure factor (in logarithmic scale) as a function of the energy (in units of eV) for  $q = 0.001\text{\AA}^{-1}$ ,  $n = 10^{12} \text{ cm}^{-2}$ , and  $R_0 = 500\text{\AA}$ . It is compared with the factor of the two-dimensional (2D in figure) infinite surface at the same electron density and  $q$  value. Only in the region  $0 < \hbar\omega < C_2q$ , for the cylinder case, there is a continuous structure (in the inset), which is not present for the infinite surface.

Up to now, in this section, we have presented all the results for a radius  $R_0 = 500 \text{ \AA}$ . An increase of the density requires a larger number  $M$  in equation (4.14). When one increases the electron density up to  $n = 10^{12} \text{ cm}^{-2}$  keeping the radius at  $R_0 = 500 \text{ \AA}$ , we take into account a number of sub-bands equal to  $M = 20$ . If one increases the radius, one reduces the gap and the sub-bands become more dense. In the case of a larger radius, the effects of the Berry phase are lost since the gap is practically closed and the sub-bands become a continuous. The two-dimensional limit for the electronic surface states is reached for larger and larger radii. In the case of  $R_0 = 4000 \text{ \AA}^{-1}$  and high density about  $10^{12} \text{ cm}^{-2}$ , we show in Figure (C.1) of Appendix C that the plasmon dispersion converges to that of the two-dimensional limit [88]. On the other hand, for a surface density  $n = 10^{12} \text{ cm}^{-2}$  and at a radius  $R_0 = 500 \text{ \AA}$ , we actually find significant corrections for the plasmon dispersion compared to the case of an infinite large cylinder (2D Dirac plasmons). Immediately, we observe a difference in the dispersions for large wavelength. In fact, for  $q < 1/R_0$ , as seen in Figure (4.6a), the dispersion for a radius  $R_0 = 500 \text{ \AA}$  has one-dimensional features of type  $\hbar\omega = \alpha q \sqrt{K_0(qR_0)}$ , with  $\alpha \sim 33 \text{ eV \AA}$ . For small  $q$  but such that  $q > 1/R_0$ , we have the two-dimensional behavior:  $\hbar\omega = \beta \sqrt{q}$ , with  $\beta \sim 1.02 \text{ eV \AA}^{1/2}$ . A clear dimensional crossover occurs for intra-band plasmons in these range of parameters. As discussed in Appendix C, in the case of a radius  $R = 4000 \text{ \AA}$  for the same density, one gets a two-dimensional dispersion for all momenta  $q$ :  $\hbar\omega = \beta_2 \sqrt{q}$ , with  $\beta_2 = \sqrt{(C_2 e^2 k_F^{2D})/2}$  and  $k_F^{2D}$  two-dimensional Fermi momentum. Note that, for the chosen parameters, one gets  $\beta_2 \sim 0.98 \text{ eV \AA}^{1/2}$ . Therefore, the  $\beta$  coefficient is slightly different from what is found for a Dirac 2D plasmon and depending on the radius. We notice that the spectral weights for  $R_0 = 500 \text{ \AA}$  and  $R = 4000 \text{ \AA}$  are practically identical as it is possible to observe for a particular  $q$  in Figure (4.6b). The only tiny difference is seen in the region  $0 < \hbar\omega < C_2 q$ . In fact, in the case of 2D Dirac plasmon, no structure is observed in that region except for that due to the finite  $\eta$  used for the calculation giving a little imaginary part to the spectrum. For the case of radius

$R_0 = 500\text{\AA}$  instead we see a small structure with a spectral weight that is five orders of magnitude smaller than the weight of the solution for  $\hbar\omega > C_2q$ , as shown in the inset of Figure (4.6b). Finally, for values of density larger than  $10^{12} \text{ cm}^{-2}$ , the plasmon is very stable and does not undergo significant variations even upon the application of magnetic field. Therefore, the Berry phase does not affect the features of the magneto-plasmon in the limit of a large radius or high density.

# Conclusion

The main purpose of this thesis has been the theoretical study of the confinement effects on the electronic properties of three-dimensional TIs. The focus has been on nano-wires of the prototype compound  $Bi_2Se_3$ . Starting from a bulk Hamiltonian based on a two-orbital model for the compound, we have analyzed not only single-electron but also collective electronic excitations such as Dirac magneto-plasmons. The electronic properties of the nano-wires have been obtained by analytical and numerical methods which have provided consistent results. We have found interesting features with varying the cross-section area, the electron surface density and the strength of an axial magnetic field. We have emphasized that the Berry phase plays an important role in the characterization of both spectral and electronic dielectric properties of TI nano-wires. Finally, we have made some predictions on single particle and collective electronic properties which could be experimentally confirmed.

First, we have analyzed the spectral properties of a  $Bi_2Se_3$  nano-wire with different geometries of the cross-section. The presence of the Berry phase allows the opening a gap at the Dirac cone for finite area cross-sections. On the other hand, the effects of a magnetic field applied along the translational axis of the nano-wire are able to close the energy gap. Therefore, we have pointed out the relevance of quantum interference effects on measurable quantities of the nano-wire, such as the gap and the magnetic flux responsible for the gap closure. An exact approach based on numerical diagonalizations has been implemented not only to check the accuracy of the analytical so-

lutions but also to study cylinders with small radii. With decreasing the radius, the numerical approach confirms the presence of a maximum and a minimum of the gap energy as a function of the radius in semiquantitative agreement with the analytical solution. Then, we have numerically studied the electronic states of a nano-wire with rectangular cross-sections focusing on different aspect ratios between the side lengths of the rectangle. We have pointed out that the gap size and the related behavior in the presence of a magnetic field are qualitatively similar but they quantitatively depend on the size and geometry of the nano-wire. Moreover, we have compared the theoretical prediction for the gap closing magnetic flux with the experimental data of Ref. [61]. Considering similar rectangular cross-sections, the theoretical estimate is about  $0.6\Phi_0$ , while the experimental one is roughly around  $0.75\Phi_0$ . Indeed, the experimental value can be enhanced by different effects, such as, for example, surface oxidation and roughness, which are not taken into account in the theoretical analysis. In any case, theory and experiment point towards the same direction.

All the methods have confirmed the presence of a minimum and maximum of the nano-wire energy gap at the  $\Gamma$  point in the range of characteristic cross-section lengths from 50 to  $100\text{\AA}$  and the resulting variation of the magnetic flux for the gap closing close to the minimum. One of the results discussed in the third chapter is obtained in the case of a rectangle with aspect ratio equal to  $1/6$ . Indeed, the minimum coincides nearly with zero energy implying that the gap can be closed without any magnetic field when the length of the smaller side is the order of  $60\text{\AA}$ . Therefore, a decoupling of the system takes place on the two sides with the shortest length along the perimeter, in strong analogy with the case of a single confinement in the direction orthogonal to these sides. Close to the minimum of the gap, the first sub-band state shows both a spatial probability density and a spin polarization concentrated almost along the shortest sides of the perimeter.

Interesting electronic properties of the nano-wire have been obtained in the range of cross section characteristic lengths from 50 and  $100\text{\AA}$ , where we ex-

pect that effects due to quantum confinements of the wave-function are not relevant. Actually, we have considered energy levels of the first sub-bands well within the gap of the three dimensional bulk. Only for cross section characteristic lengths smaller than  $10\text{\AA}$ , the first sub-band state has energies comparable with the bands of the three dimensional bulk. Indeed, it would be very interesting to theoretically analyze the transport properties of the wire by decreasing the cross-section area and varying the chemical potential (or equivalently the gate voltage). Moreover, the thermoelectric properties in TI would be enhanced in a nano-wire of Bismuth based materials which are known for their large Seebeck effects and thermoelectric figure of merit. These studies would naturally require the introduction of disorder potentials and electron-phonon couplings in the Hamiltonian model.

In the last chapter of the thesis, we have studied the charge response of a cylindrical wire of  $Bi_2Se_3$ . We have provided an analytical solution of the dynamic structure factor within the RPA approximation for the electron-electron Coulomb interaction. We have analyzed how the Berry phase and the interference on it due to an axial magnetic field affect the plasmon dispersion and spectral weights. One of the main results of the study is that, in the case of zero surface density ( $\mu = 0$ ), inter-band plasmons can form in TI nano-wires unlike in TI slabs. An axial magnetic field induces a change in dispersion and peak shape of the magneto-plasmon, which becomes more defined with a longer life-time. Then, in the case of a low surface electron density of about  $10^{10} \text{ cm}^{-2}$  in the absence of a magnetic field, we have stressed that the resulting plasmon excitation has both dispersion and spectral weight similar to those of a magneto-plasmon at zero surface density. In this case, it has been also possible to calculate the limit for  $q \rightarrow 0$  of the polarization function analytically solving the RPA equation and providing the dispersion of intra-band plasmons. The application of a magnetic field removes the degeneration of sub-bands giving rise to two types of excitations: a lower frequency with a linear behavior as a function of  $q$  and the other to a higher frequency with a behavior  $\omega \sim q\sqrt{K_0(q)}$ . The most important difference

between these two kinds of solution is in the spectral weight which is much larger for plasmons at higher frequency. Finally, we have checked that the limit of infinite two-dimensional surface is reached for a very large radius, for example  $R_0 = 0.4 \mu m$ , at a large surface density of  $10^{12} cm^{-2}$ . We have also analyzed corrective terms to the case of the two-dimensional limit in the plasmon dispersion. In any case, for high density, we have pointed out that the effects induced by an axial magnetic field are no more important.

Focus of this thesis has been on the case when, in the dynamic structure factor, the momentum  $q_{\parallel}$  parallel to x-y plane (orthogonal to the axis z of the cylinder) is zero. The effects of  $q_{\parallel}$  could give the possibility to have charge excitations where the angular degrees of freedom are more involved (perimeter plasmons). Moreover, it could be interesting to consider not only the presence of Dirac surface plasmons but also of surface plasmons related to bulk charge carriers which have been observed very recently in EELS experiments. Finally, it could be useful to study plasmon features at finite temperature analyzing the effects of electron-phonon couplings in the case of wires freely suspended or grown on a substrate.

In this thesis, the theoretical results not only confirm previous experimental observations, but also allow to predict some new behaviors of the electronic properties of TI nano-wires. Interesting aspects of the theoretical analysis are obtained for lengths of the cross-section of the order of a few tens of angstroms. These small nano-structures are not immediately realizable, but, in the near future, the results proposed in this thesis might promote experimental investigations. Moreover, in the case of the analysis about plasmons, interesting theoretical results are obtained for realistic radii of the order of about  $500 \text{ \AA}$  in the experimentally complicated regime of very low surface density, which corresponds to a chemical potential well within the bulk gap. Experiments are in constant progress toward the direction of varying the chemical potential in all the relevant energy ranges.

The analysis of the electronic properties of a TI wire is particularly interesting not only from a fundamental point of view, but also for applications. Indeed, a TI nano-wire has been suggested as a possible platform for the observation of Majorana fermions. A finite-length TI nano-wire, proximity-coupled to an ordinary bulk s-wave superconductor and subject to a longitudinal applied magnetic field, is indicated to realize a one-dimensional topological superconductor with unpaired Majorana fermions localized at both ends. This situation occurs under a wide range of conditions and constitutes an easily accessible physical realization of the elusive Majorana particle in a solid-state system [93].

# Appendices

# Appendix A

## Berry phase

A very important role for characterizing the topological phase is the concept of Berry phase [48]. We know that if a particle performs a closed path, the final state will differ from the initial one by a phase factor, this phase is observable and is attributable to a type of geometric phase. At this point we ask ourselves how a state changes if he fulfills a closed path, especially in adiabatic manner. To understand in a qualitative way from the geometrical point of view this phase, consider the example in Figure A.1. The berry phase is related to the tangent along the path taken along the sphere. If we start on the left path and go down in the  $yz$  plane until we hit  $z = 0$ , the arrows show that specific vector. Then we rotate around in the  $xy$  plane until we hit  $y = 0$ . Then we rotate back up in the  $xz$  plane. The path is a closed path on the sphere, but the resulting vector now points in a different direction but we never really rotated our vector! This is the concept of a Berry phase as a geometric phase factor. Features of the Berry phase:

1. it is a real quantity.
2. It depends only on the path of the particle and not the time taken to perform it or other variables.
3. If we talk about paths on a sphere, the berry phase will ascribe a phase factor to every path  $\gamma$ .

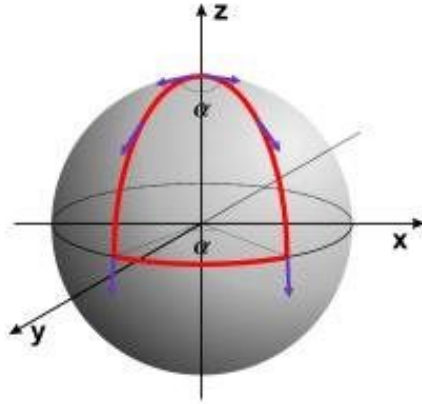


Figure A.1: Geometric representation of the Berry phase. Consider a path of a constant vector tangent to the sphere in a closed curve. Notice how the direction of the vector changes once completed the cycle, although it is not carried out any rotation to the vector.

Wanting to mathematically explain this concept, consider an adiabatic evolution. Without loss of generality, we take a system with a 1/2-spin in a time-dependent magnetic field:

$$H(t) = -\vec{B}(t) \cdot \vec{S} \quad (\text{A.1})$$

and suppose that  $\vec{B} = B\vec{n}$  is constant in time and points in some direction  $\vec{n}$ . The ground state is  $|\vec{n}\rangle$  where  $\vec{S} \cdot \vec{n} |\vec{n}\rangle = \pm \frac{1}{2} |\vec{n}\rangle$ . Then we evolve this in time, but we keep the magnetic field fixed, in this way we can write:

$$\langle \vec{n} | e^{-iHt} | \vec{n} \rangle = e^{-iE_0 t}. \quad (\text{A.2})$$

Now, we can imagine adiabatically changing  $\vec{B}$  in time. Then there's a general result that tells us that the system will stay in its ground state. Let's just slowly vary the direction  $\vec{B} = B\vec{n}(t)$ . If this is slow enough, then the ground state evolves into the ground state (adiabatic theorem). The time scale here is of order  $B$  so we change it slowly compared with  $B$  (we have neglected all  $\hbar$ ). So at any given time, our spin will follow and track

our magnetic field. So let's repeat the same calculation we made before in equation A.2 and calculate the matrix element for the spin between some initial state. Heuristically, we have:

$$\langle \vec{n}(T) | \mathcal{T} e^{-i \int_0^T H(t) dt} | \vec{n}(0) \rangle, \quad (\text{A.3})$$

where  $\mathcal{T}$  is the time-ordering that orders the product of operators according to the value of the temporal parameter. Given that the system evolves in adiabatic manner it is possible to write the equation A.3 in discrete form:

$$\begin{aligned} & \langle \vec{n}(T) | e^{-iB(T-\Delta t)S(T-\Delta t)\Delta t} | \vec{n}(T-\Delta t) \rangle \dots \langle \vec{n}(\Delta t) | e^{-iB(0)S(0)\Delta t} | \vec{n}(0) \rangle = \\ & = e^{-iNE_0\Delta t} \langle \vec{n}(T) | \vec{n}(T-\Delta t) \rangle \dots \langle \vec{n}(\Delta t) | \vec{n}(0) \rangle = \\ & = \exp(-iE_0T) \exp\left(i \int dt \langle n | \partial_t | n \rangle\right). \end{aligned} \quad (\text{A.4})$$

Therefore, through the variation of the magnetic field, the system has followed a path through adiabatic processes which has led us to an additional phase factor  $\exp(i \int dt \langle n | \partial_t | n \rangle) = \exp(i\theta_B)$  of the ground-state unlike the equation in A.2. We made three claims above about the Berry phase. Proving them here now:

1. The Berry phase depends only on the path. We've shown it is an integral of time. But we can do a change of variables:

$$\theta_B = \int dt i \langle n | \partial_t | n \rangle = \int_{\gamma} dk i \langle k | \partial_k | k \rangle \quad (\text{A.5})$$

It is not a random choice we have taken the space of moments  $k$  rather than those temporal or spatial, since we can apply the concept of Berry phase to the band theory.

2. The Berry phase is real. We can just calculate:

$$\begin{aligned} & i \langle n | \partial_t | n \rangle - (i \langle n | \partial_t | n \rangle)^* = \\ & = i(\langle n | \partial_t | n \rangle + \partial_t \langle n | n \rangle) = \\ & = i\partial_t \langle n | n \rangle = 0 \end{aligned} \quad (\text{A.6})$$

3. The term  $e^{i\theta_B}$  defines a phase factor for every path  $\gamma$ . Indeed, we can just define  $|\vec{n}(t)\rangle \rightarrow e^{i\phi(t)} |\vec{n}(t)\rangle$ . Then, the Berry phase term becomes:

$$\begin{aligned}\theta_B &\rightarrow \int_0^T dt i \langle \vec{n}(t) | e^{-i\phi(t)} \partial_t e^{i\phi(t)} | \vec{n}(t) \rangle = \\ &= \theta_B + \phi(0) - \phi(T)\end{aligned}\tag{A.7}$$

And of course, if we integrate that, we can see that the first term is the old Berry phase term and the new term gives us a phase difference.

If we want to keep the phase of Berry constant for each closed path, you have to make a particular choice that  $\phi(0) = \phi(T)$ . A different situation is for an open path, ie the Berry phase depends on the path, so it is not a well-defined quantity. It depends on both the path we take and the phase choice  $\phi(t)$ .

All that we have said for the Berry phase can be transported in the band theory in which we consider Bloch states  $|u(\mathbf{k})\rangle$  in the Brillouin zone. So we define as in the equation A.5 the relationship that leads to define the phase of Berry:

$$\mathbf{A} = -i \langle u(\mathbf{k}) | \nabla_{\mathbf{k}} | u(\mathbf{k}) \rangle.\tag{A.8}$$

$\mathbf{A}$  is equivalent to the electromagnetic vector potential. It is possible according to the gauge transformations to turn the potential  $\mathbf{A} \rightarrow \mathbf{A} + \nabla_{\mathbf{k}}\phi(\mathbf{k})$  where  $\phi(\mathbf{k})$  is a scalar function. Notice how in this way we recover the relation obtained in the equation A.7. For any closed loop  $C$  in  $\mathbf{k}$  space, we have seen that we may define the Berry phase,

$$\theta_B = \oint_C \mathbf{A} \cdot d\mathbf{k} = \int_S \mathcal{F} dk^2\tag{A.9}$$

where we applied the theorem of Stokes and  $\mathcal{F} = \nabla \times \mathbf{A}$  is the definition of the Berry curvature. Berry phase in a sense is something like the expectation value of  $2\pi i \nabla_{\mathbf{k}}$ , so if we think it is quite accurate to say that  $r \sim i \nabla_{\mathbf{k}}$ , we are able to connect this quantity to the polarization  $P$ . In fact, the polarization is something like the expectation value of  $er$ , but this is

not convincing because neither  $\langle r \rangle$  nor  $\langle i\nabla_{\mathbf{k}} \rangle$  are defined for extended Bloch states. The problem is solved immediately considering a basis of localization Wannier states associated with lattice sites [49]. For a sufficiently smooth gauge these functions are localized so that  $\langle r \rangle$  is well defined. Now we introduce another quantity connected to the phase of Berry, which defines the topological invariant that distinguishes a particular insulating from a trivial insulator. Consider one-dimensional Hamiltonian  $H(k, t)$  that changes with time adiabatically in a cyclic manner, with each completed cycle the Hamiltonian back to square one. The system has a polarization  $P$ , that is well defined up to an integer charge  $e$ . However, since the polarization can only change for integer amount of the charge  $e$  (IQHE), it is possible to write the polarization as  $P = ne$ . The change of  $P$  is related to the curvature of Berry (TKNN) integrated in space  $-\pi/a < k < \pi/a$  and  $0 < t < T$  such that  $H(k, t) = H(k, t + T)$ . Thus, the domain of the integration is the 2-torus,  $T^2$ . It follows that the integer  $n$  which appears in polarization  $P$  is the Chern number, defined:

$$n = \frac{1}{2\pi} \int_{T^2} \mathcal{F} dk dt. \quad (\text{A.10})$$

So we conclude that the families of 1D insulators defined by  $H(k, t)$  are classified by the Chern number, and that topological invariant characterizes the quantized charge pumped per cycle [50, 51]. Clearly these concepts can be extended to  $d$  dimensions.

# Appendix B

## Numerical approaches

In this Appendix, we provide details about the two numerical approaches used in the third chapter for the cases of rectangular and cylindrical cross-section, respectively.

The numerical approaches exactly solve the eigenvalue/eigenstate problem. They are based on a discretization of the Hamiltonian in Eq.(2.1), reducing the continuum to a discrete lattice. In the case of a wire, a single direction is translationally invariant, while the other two are confined. In this way just a single momentum component is a good quantum number, while in the other two directions one considers the representation of the Hamiltonian in the space site. For square/rectangular nano-wires, one considers square/rectangular lattices with fixed lattice parameters. To obtain the expression of the derivative of the first and second order in the Hamiltonian, we consider the following Taylor expansions for the wave functions:

$$\begin{aligned}\psi_{j\pm 1} &= \psi_j \pm \psi'_j a, \\ \psi_{j\pm 1} &= \psi_j \pm \psi'_j a + \frac{1}{2}\psi''_j a^2.\end{aligned}\tag{B.1}$$

In the case of translational invariance along z direction,  $j = n_x, n_y$  label the sites of the bidimensional lattice in the x-y plane. With this method we obtain a homogeneous grid where each site is distant from the nearest one

of a step equal to  $a$ . From Eq.(B.1) it is possible to obtain the expression of the derivatives that appear in the eigenvalue problem:

$$\begin{aligned}\psi_j' &= \frac{\psi_{j+1} - \psi_{j-1}}{2a}, \\ \psi_j'' &= \frac{\psi_{j+1} + \psi_{j-1}}{a^2} - \frac{2\psi_j}{a^2}.\end{aligned}\tag{B.2}$$

Once built the matrix elements, it is possible to obtain eigenvalues and eigenvectors with any diagonalization routine.

In the case of the cylindrical nano-wire, the procedure is more complicated since one has to discretize the continuum model with a circumference as boundary. This issue is particularly relevant since we want to study the surface states. With the procedure adopted in the case of the square/rectangular cross-section, one can select the points that fall into a circle inscribed within the square in order to obtain a circular cross-section. It is evident, however, that, being the lattice path constant, the sites will never lie perfectly along the circumference, but we could only approximate it. This approximate procedure for the cylinder will be indicated as constant mesh.

To improve the approach, we choose a mesh such that the sites present in bulk are more rarefied and those on the edge are more dense, as shown in Figure B.1. In this way, we are able to create a perfect circumference, simulating very well the surface. Using a numerical diagonalization procedure with open boundary conditions, one gets bulk and surface states making a comparison with the analytical solutions. The numerical approach perfectly reproduces the analytical results for large radii, where the analytical solutions are valid. Therefore, the numerical approach allows to make an extrapolation to the continuum limit. Since we have considered a variable mesh, we make the limit of the average lattice parameter of the lattice to zero.

To derive the matrix elements of the Hamiltonian, we exploit the Taylor expansion of the first and second derivatives present in Eq.(2.1). If we consider the  $i$ -th site, where the index  $i = x, y$ , we denote  $a_i$  its distance from the nearest neighbor on the left,  $a_{i+1}$  its distance from the nearest neighbor

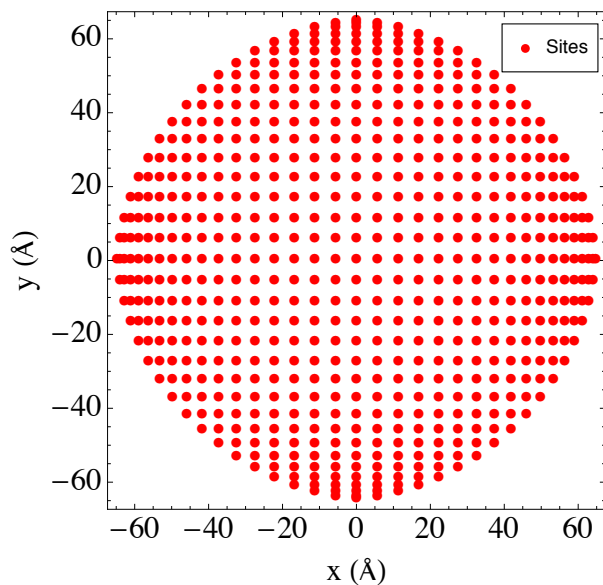


Figure B.1: Site positions (in the real space) with variable mesh in the case of radius  $R = 65\text{\AA}$ . A perfect circumference on the boundary is numerically simulated.

on the right. Based on these notations, we write the first derivative of the wave function  $\psi$  in terms of finite differences:

$$\begin{aligned}\psi_{i+1} &= \psi_i - \psi'_i a_i \\ \psi_{i-1} &= \psi_i + \psi'_i a_{i+1}.\end{aligned}\tag{B.3}$$

Doing the same with the expansion to the second order of the eq.(B.3), one gets:

$$\begin{aligned}\psi'_i &= \frac{\psi_{i-1} - \psi_{i+1}}{a_i + a_{i+1}} \\ \psi''_i &= \frac{2\psi_{i+1}}{a_i(a_{i+1} + a_i)} + \frac{2\psi_{i-1}}{a_{i+1}(a_{i+1} + a_i)} - \frac{2\psi_{i,j}}{a_i a_{i+1}}\end{aligned}\tag{B.4}$$

Therefore, we are able to write the Hamiltonian (2.1) as a matrix  $(4N_x N_y)^2$ , where  $N_x$  and  $N_y$  are the site numbers along x and y direction in the non-uniform grid. In the case where  $a_{i+1} = a_i = a$ , we get back the equations in

(B.2). This grid is constructed such that each distance scales as a function of sine and cosine. Hence, it is possible to select points that are located at a distance from the center less or equal to half side of the square which contains the circle (see Figure B.1 ). The elements which are outside the circle must be put to zero. Therefore, the matrix will contain a number of rows and columns containing zeros. Once allocated the matrix, it is possible to obtain eigenvalues and eigenvectors with any diagonalization routine.

In order to emphasize similarities and differences between different geometries, we compare square and circular cross-sections (the circumference is inscribed in the square) by using the same numerical procedure (fixed grid). In the case of the cylinder, the energy dispersions are compared for a constant and variable mesh at fixed radius, as shown in Figure B. The energies of the first sub-band are in good agreement.

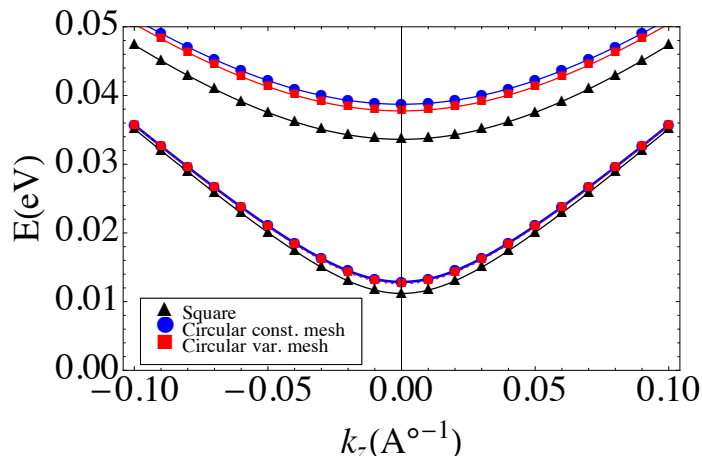


Figure B.2: Energy dispersion (in eV) of the first and second subband as a function of  $k_z$  (in  $\text{\AA}^{-1}$ ) for a square with side  $L = 240\text{\AA}$  (black line with triangles). The energies for a circular cross-section of radius  $R = 120\text{\AA}$  are also shown in the case of uniform (blue line with circles) a non-uniform (red line with squares) grid.

Once found eigenstates and eigenvalues, we can get the orientation of spin on the surface building up a matrix similar to that in equation (3.10)

of section III. This time, however, the representation is made considering a discrete lattice and not a continuum. Therefore, considering for simplicity  $k_z = 0$  and indicating with 0 and  $-1$  the two eigenvectors corresponding to the same eigenvalue, one gets the following matrix for the spin components at each lattice site:

$$\begin{pmatrix} \langle \psi_0(i) | S_j | \psi_0(i) \rangle & \langle \psi_0(i) | S_j | \psi_{-1}(i) \rangle \\ \langle \psi_{-1}(i) | S_j | \psi_0(i) \rangle & \langle \psi_{-1}(i) | S_j | \psi_{-1}(i) \rangle \end{pmatrix},$$

with  $j = x, y, z$ . Therefore, the couple  $(r, \phi)$  of the wave function  $\psi_m(r, \phi)$  in Eq.(3.10) is replaced by the index  $i$  that labels the sites as in Figure B.1. The eigenvalues of the equation (B.5) for each site  $i$  will provide the spin orientation as found in bottom panel of Figure 3.5 in section III.

# Appendix C

## Large radius limit of the polarization function and plasmon dispersion in cylindrical wire

In this appendix, we want to clarify the concept of polarization function in the cylindrical wire discussed in chapter four. In particular as evidence of our analytical result, we provide a limit for large radius ( $R_0 \rightarrow \infty$ ) that allows us to reconstruct the two-dimensional plasmon dispersion.

We consider the surface wave functions of a TI cylindrical wire obtained from previous works [63, 68]:

$$\psi_{k,m}^s(\rho, \phi, z) = \sqrt{\frac{1}{4\pi L}} e^{ikz} R(\rho) e^{im\phi} \mathbf{u}_{k,m}^s(\phi), \quad (\text{C.1})$$

where  $L$  is the length along the  $z$  axis,  $R(\rho)$  is the radial function,  $\mathbf{u}_{k,m}^s(\phi)$  is a quadri-spinor depending on the angular variable  $\phi$ . In Eq.(C.11), the radial function  $R(\rho)$  is zero for  $\rho \geq R_0$ , while, for  $0 < \rho < R_0$  for large radii, it is the following:

$$R(\rho) = N e^{-\alpha - R_0} (e^{(\alpha_+ + \alpha_-)\rho} - e^{\alpha_+ R_0 + \alpha_- \rho}), \quad (\text{C.2})$$

with  $N$  normalization constant,

$$\alpha_{\pm} = \frac{1 \pm \sqrt{1 + 4a}}{2L_0},$$

$$a = -\frac{M_2 M_0}{A^2}, \quad L_0 = \frac{M_2}{A}.$$

We re-write In Eq.(C.11), for negative eigenvalues  $\epsilon_{k,m}^-$ , the quadri-spinor

$$\mathbf{u}_{k,m}^-(\phi) = \begin{bmatrix} \frac{1}{2} + \alpha_{k,m} + i\beta_{k,m} \\ -\frac{i}{2} + i(\alpha_{k,m} + i\beta_{k,m}) \\ -\frac{e^{i\phi}}{2} + e^{i\phi}(\alpha_{k,m} + i\beta_{k,m}) \\ \frac{1}{2}ie^{i\phi} + ie^{i\phi}(\alpha_{k,m} + i\beta_{k,m}) \end{bmatrix}, \quad (\text{C.3})$$

while, for positive eigenvalues  $\epsilon_{k,m}^+$ , it is

$$\mathbf{u}_{k,m}^+(\phi) = \begin{bmatrix} \frac{1}{2} - (\alpha_{k,m} + i\beta_{k,m}) \\ -\frac{i}{2} - i(\alpha_{k,m} + i\beta_{k,m}) \\ -\frac{e^{i\phi}}{2} - e^{i\phi}(\alpha_{k,m} + i\beta_{k,m}) \\ \frac{1}{2}ie^{i\phi} - ie^{i\phi}(\alpha_{k,m} + i\beta_{k,m}) \end{bmatrix}. \quad (\text{C.4})$$

with

$$\alpha_{k,m} = \frac{(\frac{1}{2} + m - r) C_1}{2\sqrt{C_2^2 k^2 + (\frac{1}{2} + m - r)^2 C_1^2}}, \quad (\text{C.5})$$

$$\beta_{k,m} = \frac{C_2 k}{2\sqrt{C_2^2 k^2 + (\frac{1}{2} + m - r)^2 C_1^2}}.$$

We can evaluate the term  $\chi_0(z - z', \phi - \phi'; \omega)$  present in the equation (4.2) for the full susceptibility:

$$\chi_0(z - z', \phi - \phi'; \omega) = \frac{1}{(2\pi L)^2} \sum_{k,q,m,l,s,s'} e^{iq(z-z')} \times e^{il(\phi-\phi')} \frac{f(\epsilon_{k,m}^s) - f(\epsilon_{k+q,m+l}^{s'})}{\epsilon_{k,m}^s - \epsilon_{k+q,m+l}^{s'} + \hbar(\omega + i0^+)} F^{s,s'}(k, q, m, l), \quad (\text{C.6})$$

where  $q$  is the momentum along  $z$  axis,  $l$  is the angular number, and  $F^{s,s'}(k, q, m, m+l)$  is the scalar product between the eigenvectors in (C.4) and (C.5):

$$F^{s,s'}(k, q, m, m+l) = \frac{1}{2} \left[ 1 + ss' \times \frac{\tilde{\Delta}^2(R_0) (1 + 2m + 2l) (1 + 2m) + k(k+q)}{\sqrt{\tilde{\Delta}^2(R_0)(1+2m) + k^2} \sqrt{\tilde{\Delta}^2(R_0)(1+2m+2l) + (k+q)^2}} \right], \quad (\text{C.7})$$

with

$$\tilde{\Delta}(R_0) = \frac{C_1}{2C_2 R_0}.$$

Finally transforming in the equation (C.6) the discrete sum over  $k$  in a integral, we get the polarization function  $\chi_0(q, l; \omega)$  used in the main text:

$$\chi_0(q, l; \omega) = \frac{1}{(2\pi)^2} \int dk \sum_{m,s,s'} \frac{f(\epsilon_{k,m}^s) - f(\epsilon_{k+q,m+l}^{s'})}{\epsilon_{k,m}^s - \epsilon_{k+q,m+l}^{s'} + \hbar(\omega + i0^+)} \times F^{s,s'}(k, q, m, l). \quad (\text{C.8})$$

The polarization function in equation (C.8) is expressed in terms of a sum on  $m$ . We will show that, in the limit of infinite radius, the double sum in  $k$  and  $m$  will transform in a bi-dimensional integral over  $\mathbf{k}$ . Therefore, equation (C.8) becomes the susceptibility of a 2D problem in the large radius limit. To this aim, for simplicity, we take only the contributions for  $l = 0$ . The energy for our problem is defined as  $\epsilon_{k,m} = \pm C_2 \sqrt{k^2 + (m + 1/2)^2 / R_0^2}$  having considered  $C_1 = C_2$ . In the 2D case we have  $\epsilon_k = \pm \hbar v_F \sqrt{k^2 + k_{\parallel}^2}$ , where  $C_2 = \hbar v_F$ ,  $k$  is the same associated to  $z$  direction and  $\mathbf{k}_{\parallel}$  is the other momentum in the plane. If we send  $R_0 \rightarrow \infty$  also the parameter  $m \rightarrow \infty$ , and, if  $k_{\parallel} = \frac{2\pi}{L} m$ , where  $L = 2\pi R_0$ , then in this limit  $m/R_0 \rightarrow k_{\parallel}$ . The factor  $1/2$  due to Berry phase, in the limit of large radius, is no longer relevant. Automatically, even the pre-factors  $F^{s,s'}(k, q, m, m+l)$  becomes the two-dimensional ones:

$$F^{s,s'}(k, |\mathbf{k}_{\parallel}|, q) = \frac{1}{2} \left[ 1 + ss' \frac{k(k+q) + k_{\parallel}^2}{\sqrt{k^2 + k_{\parallel}^2} \sqrt{(k+q)^2 + k_{\parallel}^2}} \right]. \quad (\text{C.9})$$

Finally, the discrete sum on  $m$  becomes a continuum such that  $\sum_m \rightarrow R_0 \int dk_{||}$ . Naturally, we note that between  $\chi_0(q; \omega)$  and  $\chi_{2D}(q; \omega)$  there is a length factor of difference, therefore, we conclude that

$$\frac{1}{R_0} \chi_0(q; \omega) \xrightarrow{R_0 \rightarrow \infty} \chi_{2D}(q; \omega) \quad (\text{C.10})$$

where  $\chi_{2D}(q; \omega)$  is

$$\begin{aligned} \chi_{2D}(q, \omega) = \frac{1}{(2\pi)^2} \int d\mathbf{k} \sum_{s, s'} \frac{f(\epsilon_k^s) - f(\epsilon_{k+q}^{s'})}{\epsilon_k^s - \epsilon_{k+q}^{s'} + \hbar(\omega + i0^+)} \\ \times F^{s, s'}(k, k_{||}, q). \end{aligned} \quad (\text{C.11})$$

If we also considered contributions for  $l \neq 0$ , in addition to the momentum  $q$  another transferred momentum  $q_{||}$  of transversal type to the axis of the cylinder would appear.

We can find through the electron density function, the equation of the RPA theory given by  $1 - \tilde{V}_{q,l} \chi_0(q, l; \omega) = 0$ , which provides the condition for plasmon formation in the system. For this reason we need to expand the Coulomb potential in the cylindrical coordinates [92] as follows:

$$\begin{aligned} V(\vec{r} - \vec{r}') = \frac{2}{\pi} \sum_{m=-\infty}^{\infty} \int_0^{\infty} dk I_m(kr_{<}) K_m(kr_{>}) \\ \times e^{im(\phi - \phi')} \cos[k(z - z')] \end{aligned} \quad (\text{C.12})$$

which, by using translational invariance in the  $z$  direction, becomes

$$V(q; \mathbf{r}, \mathbf{r}') = 2 \sum_{m=-\infty}^{\infty} I_m(|q|r_{<}) K_m(|q|r_{>}) e^{im(\phi - \phi')} \quad (\text{C.13})$$

where we used

$$\begin{aligned} \int dz e^{-iq(z-z')} \cos[k(z-z')] = \\ = 2\pi \frac{1}{2} [\delta(q-k) + \delta(q+k)]. \end{aligned} \quad (\text{C.14})$$

From the definition, the induced density can be written as  $\rho(\vec{r}) = \int d\vec{r}' d\vec{r}'' \chi(\vec{r}, \vec{r}') V(\vec{r}' - \vec{r}'') \rho(\vec{r}'')$  where  $\chi(\vec{r}, \vec{r}'; \omega) = R(\rho)^2 R(\rho')^2 \chi_0(z - z', \phi - \phi'; \omega)$  is the susceptibility.

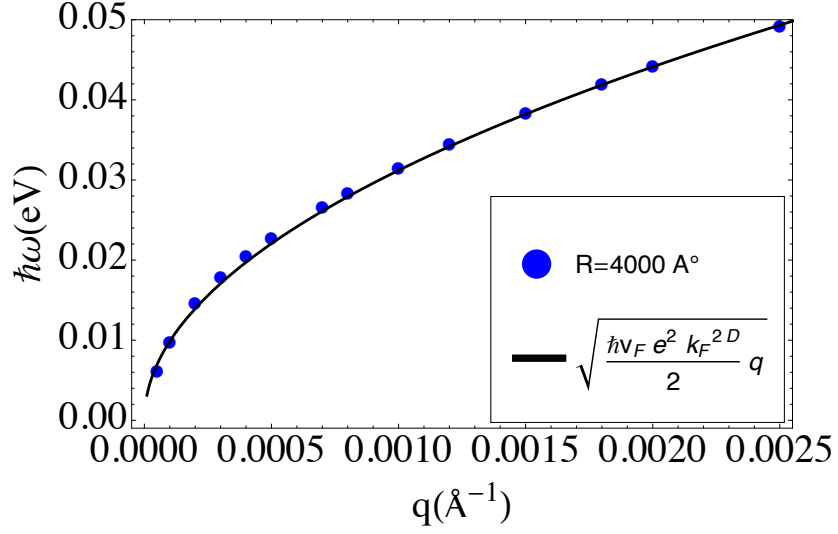


Figure C.1: The plasmon dispersion as a function of the momentum  $q$  along  $z$  for a cylindrical wire of radius  $R = 4000\text{\AA}$ . The result is compared with that of an infinite plane (translational invariance along all two directions [88]). In this limiting case, there is an analytical form for the plasmon dispersion which is reported in the figure.

Passing in Fourier transform in  $q$  and in  $l$ , and replacing the equation (C.6) and (C.13) in  $\rho(\vec{r})$ , we have that the density is given by:

$$\begin{aligned} \rho_{q,l}(r) &= 4\pi e^2 \chi_0(q, l) \int dr' r' R(r)^2 R(r')^2 \\ &\times \int dr'' r'' I_n(|q|r_<) K_n(|q|r_>) \cdot \rho_{q,l}(r''). \end{aligned} \quad (\text{C.15})$$

If we define:

$$\begin{aligned} S_{q,l}(r'') &= \int dr' r' R(r')^2 I_l(|q|r_<) K_l(|q|r_>) \\ &= K_l(|q|r'') \int_0^{r''} dr' r' R(r')^2 I_l(|q|r') \\ &+ I_l(|q|r'') \int_{r''}^{R_0} dr' r' R(r')^2 K_l(|q|r'), \end{aligned} \quad (\text{C.16})$$

and multiplying by  $S_{q,l}(r)$  to the left and right member and integrating over

$r$ , the equation in (C.15) becomes:

$$1 = \chi_0(q, l; \omega) \tilde{V}_{q,l}. \quad (\text{C.17})$$

where we called  $\tilde{V}_{q,l} = 4\pi e^2 \int dr r R(r)^2 S_{q,l}(r)$ . Recalling that  $l = 0$ , we note that, if  $R_0$  is very large, for long wavelength  $qR_0 \ll 1$ , thus we can write

$$\begin{aligned} R_0 \tilde{V}_{q,l=0} &= 4\pi e^2 R_0 \int dr r R(r)^2 S_{q,0}(r) & (\text{C.18}) \\ &\mapsto 4\pi e^2 R_0 I_0(qR_0) K_0(qR_0) \mapsto \frac{2\pi e^2}{q}, \end{aligned}$$

which is the transformed of the two-dimensional Coulomb potential. Therefore the equation in (C.17) for large  $R_0$  becomes

$$1 = \frac{1}{R_0} \chi_0(q, \omega) \frac{2\pi e^2}{q}$$

where, in this limit, from equation (C.17),  $\chi_0(q, 0)/R_0$  converges towards the two-dimensional susceptibility. As shown in the Figure (C.1), the plasmon dispersion of the infinite radius nano-wire converges to that of a 2D problem ( $\omega \propto \sqrt{q}$ ).

# Appendix D

## Calculation of the inverse dielectric function and dynamic structure factor in cylindrical wire

In this appendix we calculate the inverse of the dielectric constant and, then, the dynamic structure factor presented in the fourth chapter for a cylindrical wire. This calculation could be extended to any type of geometry, although here for simplicity it is specialized for a cylindrical case. Exploiting the symmetries of the cylinder and using equation (C.12), the dielectric constant given in equation (4.3) can be written as:

$$\begin{aligned} \epsilon(\vec{r}, \vec{r}') &= \frac{\delta(\rho - \rho')}{\rho} \delta(\phi - \phi') \delta(z - z') \\ &- \frac{2}{L} R(\rho')^2 \sum_q e^{iq(z-z')} \sum_l e^{il(\phi-\phi')} S_{q,l}(\rho) \chi_0(q, l; \omega). \end{aligned} \quad (\text{D.1})$$

The inverse dielectric function is so defined:

$$\int d\vec{r}'_1 \epsilon^{-1}(\vec{r}, \vec{r}'_1) \epsilon(\vec{r}'_1, \vec{r}') = \delta(\vec{r} - \vec{r}'). \quad (\text{D.2})$$

Using  $q$  and  $l$  and replacing the equation (D.1) in (D.2), we get :

$$\int d\rho_1 \rho_1 \epsilon_{q,l}^{-1}(\rho, \rho_1) \left( \frac{\delta(\rho_1 - \rho')}{\rho_1} + \right. \quad (D.3)$$

$$\left. -4\pi R(\rho')^2 S_{q,l}(\rho_1) \chi_0(q, l) \right) = \frac{\delta(\rho - \rho')}{\rho}.$$

We need to solve an integral equation with a separable variable kernel. If we define  $A_{q,l}(\rho) = \int d\rho_1 \rho_1 \epsilon_{q,l}^{-1}(\rho, \rho_1) S_{q,l}(\rho_1)$  and we multiply for  $S_{q,l}(\rho')$ , integrating both members over  $\rho'$ , the integral equation becomes:

$$A_{q,l}(\rho) \left[ 1 - 4\pi \chi_0(q, l) \int d\rho' \rho' R(\rho')^2 S_{q,l}(\rho') \right] = S_{q,l}(\rho). \quad (D.4)$$

We note that the equation in square parenthesis is equal to equation in (C.17) since  $\tilde{V}_{q,l} = 4\pi \int d\rho' \rho' R(\rho')^2 S_{q,l}(\rho')$ . This way, it is possible find the term  $A_{q,l}$  from the equation (D.4) that replaced in (D.3) returns

$$\epsilon_{q,l}^{-1}(\rho, \rho') = \frac{\delta(\rho - \rho')}{\rho} + \frac{S_{q,l}(\rho) \chi_0(q, l; \omega) R(\rho')^2}{1 - \chi_0(q, l; \omega)}. \quad (D.5)$$

Finally we can write a dynamic structure factor in this form:

$$L(\omega, q, q_{||}) = -Im \left[ \frac{1}{V} \int \int d\vec{r} d\vec{r}' \epsilon^{-1}(\vec{r}, \vec{r}') e^{-i\vec{q}\cdot\vec{r}} e^{i\vec{q}\cdot\vec{r}'} \right], \quad (D.6)$$

where  $V$  is the volume enclosed by the cylinder. Exploiting the cylindrical symmetries and passing in Fourier transform with  $\epsilon^{-1}(\vec{r}, \vec{r}') = \frac{1}{L} \sum_q e^{iq(z-z')} \frac{1}{2\pi} \sum_l e^{il(\phi-\phi')} \epsilon_{q,l}^{-1}(\rho, \rho')$ , we get for the only integral part over  $z$  and  $z'$  in (D.6):

$$\frac{1}{L^2} \frac{L}{2\pi} \int dq \int \int dz dz' e^{i(q-q)z} e^{i(q-q)z'} = 1. \quad (D.7)$$

Finally, we have:

$$L(\omega, q, q_{||}) = -\frac{1}{2\pi^2 R_0^2} Im \left[ \sum_l \frac{\chi_0(q, l; \omega)}{1 - \chi_0(q, l; \omega) \tilde{V}_{q,l}} \right. \quad (D.8)$$

$$\times \int d\rho' \rho' d\phi' e^{i|q_{||}|\rho' \cos \phi'} e^{-il\phi'} R(\rho')^2$$

$$\left. \times \int d\rho d\phi e^{i|q_{||}|\rho \cos \phi} e^{il\phi} S_{q,l}(\rho) \right]$$

where both the integrals in  $\phi$  and  $\phi'$  return the Bessel functions  $4\pi^2 J_l(|q_{||}|\rho)J_l(|q_{||}|\rho')$ . The integral in (D.8) is thus obtained:

$$L(q, q_{||}; \omega) = -\frac{2}{R_0^2} \text{Im} \left[ \sum_l \frac{\chi_0(q, l; \omega)}{1 - \chi_0(q, l; \omega) \tilde{V}_{q,l}} \right. \quad (\text{D.9})$$

$$\left. \times \int_0^{R_0} d\rho' \rho' J_l(|q_{||}|\rho') R(\rho')^2 \int_0^\infty d\rho \rho J_l(|q_{||}|\rho) S_{q,l}(\rho) \right].$$

We notice that the second integral in equation (D.9) depends on  $S_{q,l}$  which is linked to the Coulomb potential. Since the Coulomb interaction between electrons is effective in the whole space, inside and outside the material, the integration limits of the radial variables are extended from

# Bibliography

- [1] Thouless, D. J., M. Kohmoto, M. P. Nightingale, and M. den Nijs, Phys. Rev. Lett. **49**, 405 (1982)
- [2] Von Klitzing K, Dorda G. Pepper M. Phys Rev Lett **45**, 494 (1980)
- [3] Kane CL., Mele EJ. Phys Rev Lett **95**, 14680 (2005)
- [4] Xiao-Liang Qi and Shou-Cheng Zhang, American Institute of Physics, S-0031-9228-1001-020-3 (2009)
- [5] M. Z. Hasan and C. L. Kane Rev. Mod. Phys. **82**, 3045 (2010)
- [6] T. Fukui, Y. Hatsugai, J. Phys. Soc. Jpn. **76**, 053702 (2007)
- [7] Moore JE. Balents L. Phys Rev B **75**, 121306 (2007)
- [8] Roy R. Phys Rev B **79**, 195322 (2009)
- [9] Fu L. Kane CL Mele EJ Phys Rev Lett **98**, 106803 (2007)
- [10] Ringel Z, Kraus YE, Stern A. Phys Rev B **86**, 045102 (2012)
- [11] Liu CX, Qi XL, Zhang SC. Physica E **44**, 906 (2012)
- [12] Kohomoto M, Halperin BI, Wu YS Phys Rev B **45**,13488 (1992)
- [13] Ran Y, Zhang Y, Vishwanath A, Nat Phys **5**, 298 (2009)
- [14] Lee PA, Ramakrishnan TV. Rev Mod Phys **57**, 2871985 (1985)

- [15] Fu L. Kane CL. Phys Rev B **76**, 045302 (2007)
- [16] Liu Y, Allen E, Phys. Rev. B **52**,1566 (1995)
- [17] Roushan P, et al., Nature **460**,1106 (2009)
- [18] Hsieh D, et al., Nature **460**, 1101 (2009)
- [19] Zhang T, et al., Phys. Rev. Lett. **103**, 266803 (2009)
- [20] Hor YS, et al., Phys. Rev. B **79**, 195208 (2009)
- [21] Chen YL, et al., Science **325**, 178 (2009)
- [22] Hsieh D, et al., Phys. Rev. Lett. **103**,146401 (2009)
- [23] Y. Zhang, K. He, C.Z. Chang, C.L. Song, L.L. Wang, X. Chen, J.F. Jia, Z. Fang, X. Dai, W.Y. Shan, S.Q. Shen, Q. Niu, X.L. Qi, S.C. Zhang, X.C. Ma, Q.K. Xue, Nat. Phys. **6**, 584 (2010)
- [24] Y. Sakamoto, T. Hirahara, H. Miyazaki, S. Kimura, S. Hasegawa, Phys. Rev. B **81**, 165432 (2010)
- [25] Seung Sae Hong et al., Nano Lett **14**, 2815-2821, (2014)
- [26] J.G. Checkelsky, Y.S. Hor, M.-H. Liu, D.-X. Qu, R.J. Cava, N.P. Ong, Phys Rev Lett **103**, 246601 (2009)
- [27] J.G. Checkelsky, Y.S. Hor, R.J. Cava, N.P. Ong, Phys Rev Lett **106** 196801 (2011)
- [28] A.D. LaForge, A. Frenzel, B.C. Pursley, T. Lin, X. Liu, J. Shi, D.N. Basov, Phys Rev B **81**, 125120 (2010)
- [29] N.P. Butch, K. Kirshenbaum, P. Syers, A.B. Sushkov, G.S. Jenkins, H.D. Drew, J. Paglione, Phys Rev B **81**, 241301 (2010)
- [30] D. Kim, S. Cho, N.P. Butch, P. Syers, K. Kirshenbaum, J. Paglione, M.S. Fuhrer, arXiv:1105.1410, to be published.

- [31] B. Buttner, C. Liu, G. Tkachov, E. Novik, C. Brune, H. Buhmann, E.M. Hankiewicz, P. Recher, B. Trauzettel, S. Zhang, et al., *Nature Physics* **7**, 418 (2011)
- [32] Ying Xing, Yi Sun, Meenakshi Singh Yan-Fei Zhao, Moses H. W. Chan-Jian Wang, *Frontiers of Physics* **8**, 491 (2013)
- [33] H. B. Zhang, H. L. Yu and G. W. Yang *EPL*, **95**, 56002 (2011)
- [34] J. Wang, A.M. DaSilva, C.-Z. Chang, K. He, J.K. Jain, N. Samarth, X.-C. Ma, Q.-K. Xue, and M.H.W. Chan, *Phys Rev B* **83**, 245438 (2011)
- [35] S. Hikami, A.I. Larkin, and Y. Nagaoka, *Progress of Theoretical Physics* **63**, 707-710 (1980)
- [36] P.A. Lee, and T.V. Ramakrishnan, *Phys Rev B* **26**, 4009 (1982)
- [37] Niv Levy et al., *Phys. Rev. Lett.* **110**, 117001 (2013)
- [38] Peng, H.; et al., *Nature Materials* **9**, 225-229 (2010)
- [39] Xiu, F.; et al., *Nature Nanotechnology* **6**, 216-221 (2011).
- [40] Sacepe, B. et al.; *Nature Commun.* **2**, 575 (2011)
- [41] Kim, D. et al.; *Nat. Phys.* **8**, 458-462 (2009)
- [42] Hong, S. S. et al; *Nature Comm.*, **3**, 757 (2012)
- [43] Bardarson, J. H. et al; *Phys. Rev. Lett.*, **105**, 156803 (2010)
- [44] Efimkin D K et al; *Nanoscale Research Letters* **7**, 1-10 (2012)
- [45] Ju, L. et al., *Nature Nanotech.* **6**, 630-634 (2011)
- [46] P. Di Pietro et al, *Nature Nanotechnology* **8**, 556-560 (2013)
- [47] A. Politano et al, *PRL* **115**, 216802 (2015)
- [48] Berry MV *Proc R Soc Lond A*, **392**, 45 (1984)

- [49] King-Smith RD, Vanderbilt D. Phys Rev B **47**, 1651 (1993)
- [50] Thouless DJ Phys Rev B **27**, 6083 (1983)
- [51] Niu Q. Thouless DJ Phys Rev A **17**, 2453 (1984)
- [52] S.-Q. Shen, *Topological Insulators - Dirac Equation in Condensed Mat-  
ters* (Springer, 2012).
- [53] H. Zhang, C.-X. Liu, X.-L. Qi, X. Dai, Z. Fang, and S. C. Zhang, Nature  
Phys. **5**, 438 (2009)
- [54] C A Perroni, D Bercioux, V Marigliano Ramaglia and V Cataudella, J.  
Phys.: Condens. Matter **19**, 186227 15 (2007)
- [55] Z. Ringel, Y. E. Kraus, A. Stern, Phys. Rev. B **86**, 045102 (2012)
- [56] Wen-Yu Shan, Hai-Zhou Lu and Shun-Qing Shen, New Journal of  
Physics **12**, 043048 23 (2010)
- [57] H. Zhang, C.-X. Liu, X.-L. Qi, Xi Dai, Z. Fang and S.-C. Zhang, Nat.  
Phys. **5**, 438 (2009)
- [58] Y.A. Bychkov, E.I. Rashba, J. Phys. C **17**, 6039 (1984)
- [59] V. Marigliano Ramaglia, D. Bercioux, V. Cataudella, G. De Filippis, C.  
A. Perroni, and F. Ventriglia, Eur. Phys. J. B **36**, 365 (2003)
- [60] H. Peng, K. Lai, D. Kong, S. Meister, Y. Chen, X.-L. Qi, S.-C. Zhang,  
Z.-X. Shen, and Y. Cui, Nat. Mater. **9**, 225 (2010)
- [61] J. Dufouleur, L. Veyrat, A. Teichgrber, S. Neuhaus, C. Nowka, S. Ham-  
pel, J. Cayssol, J. Schumann, B. Eichler, O. G. Schmidt, B. Bchner, and  
R. Giraud, Phys. Rev. Lett. **110**, 186806 (2013)
- [62] L. Zhang, J. Zhuang, Y. Xing, J. Li, J. Wang, and H. Guo, Phys. Rev.  
B **89**, 245107 (2014)

- [63] P. Iorio, C.A. Perroni, and V. Cataudella, *Eur. Phys. J. B* **89**, 97 (2016)
- [64] J. H. Bardarson, P. W. Brouwer, and J. E. Moore, *Phys. Rev. Lett.* **105**, 156803 (2010)
- [65] Yi Zhang and A. Vishwanath, *Phys. Rev. Lett.* **105**, 206601 (2010)
- [66] D. Bercioux and P. Lucignano, *Rep. Prog. Phys.* **78**, 106001 (2015)
- [67] A. Kundu, A. Zazunov, A. Levy Yeyati, T. Martin, and R. Egger, *Phys. Rev. B* **83**, 125429 (2011)
- [68] K.-I. Imura, Y. Takane, and A. Tanaka, *Phys. Rev. B* **84**, 195406 (2011)
- [69] O. Deb, A. Soori, D. Sen, *J. Phys.: Condens. Matter* **26**, 315009 (2014)
- [70] D. Kong, J. C. Randel, H. Peng, J. J. Cha, S. Meister, K. Lai, Y. Chen, Z.-X. Shen, H. C. Manoharan and Y. Cui, *Nano Lett.* **10** 329 (2010)
- [71] L. J. Slater, *Confluent Hypergeometric Functions* (Cambridge University Press, 1960).
- [72] B. Dwork, *Trans. Amer. Math. Soc.* **285**, 497 (1984)
- [73] See G. Arfken, *Mathematical Methods for Physicists* (Academic Press, 3rd ed., Orlando, FL, 1985).
- [74] H. Tang, D. Liang, R. L. J. Qiu, and X. P. A. Gao, *ACS Nano* **5**, 7510 (2011)
- [75] H. Peng, K. Lai, D. Kong, S. Meister, Y. Chen, X.-L. Qi, S.-C. Zhang, Z.-X. Shen, and Y. Cui, *Nat. Mater.* **9**, 225 (2010)
- [76] O. Deb, A. Soori, D. Sen, *J. Phys.: Condens. Matter* **26**, 315009 (2014)
- [77] F. W. Chen, L. A. Jauregui, Y. Tan, M. Manfra, G. Klimeck, Y. P. Chen and T. Kubis, *Appl. Phys. Lett.* **107**, 121605 (2015)

- [78] A. Richardella, A. Kandala, J. S. Lee, and N. Samarth, *APL Mater.* **3**, 083303 (2015)
- [79] G. Chen, L. Kauffman, S.J. Lomonaco (eds.): *The Mathematics of Quantum Computation and Quantum Topology* Chapman - Hall CRC, 2007.
- [80] G.P. Collins, *Sci. Am.*, **63**, (2006)
- [81] H. Zhang, X. Zhang, C. Liu, S.-T. Lee, and J. Jie, *ACS Nano*, **10**, 5113 (2016)
- [82] D. Pesin, A. H. MacDonald, *Nat. Mater.* **11**, 409 (2012)
- [83] P. Di Pietro, M. Ortolani, O. Limaj, A. Di Gaspare, V. Giliberti, F. Giorgianni, M. Brahlek, N. Bansal, N. Koirala, S. Oh, P. Calvani, and S. Lupi, *Nat. Nanotechnol.*, **8** 556 (2013)
- [84] J.-Y. Ou, J.-K. So, G. Adamo, A. Sulaev, L. Wang, and N. I. Zheludev, *Nat. Commun.*, **5**, 5139 (2014)
- [85] T. Stauber, *J. Phys.: Condens. Matter*, **26**, 123201 (2014)
- [86] A. Thakur, R. Sachdeva, and A. Agarwal, arXiv:1604.00806v1 (2016)
- [87] P. K. Pyatkovskiy, *J. Phys.: Condens. Matter*, **21**, 025506 (2009)
- [88] B. Wunsch, T. Stauber, F. Sols, and F. Guinea, *New J. Phys.*, **8**, 318 (2006)
- [89] P. Iorio, C.A. Perroni, and V. Cataudella, PRB Submitted.
- [90] G. Onida, L. Reining, and A. Rubio, *Rev. Mod. Phys.*, **74**, 601 (2002)
- [91] F. Bechstedt, *Many-Body Approach to Electronic Excitations. Concepts and Applications* (Springer-Verlag Berlin Heidelberg 2015).
- [92] H. S. Cohland, and J. E. Tohline, *Astrophys. J.* **527**, 86 (1999)

- [93] A. M. Cook, M. M. Vazifeh, and M. Franz Phys. Rev. B **86**, 15543 (2012)